STUDY ON THE PRODUCTION AND AGGREGATION OF DEFECTS IN ZIRCONIUM NITRIDE

モハメド, マジデュール, ラーマン

Study on the production and aggregation of defects in zirconium nitride

A dissertation submitted to the department of
Applied Quantum Physics and Nuclear Engineering
in partial fulfillment of the requirements
for the degree of

DOCTOR OF ENGINEERING

By

Mohammad Majidur Rahman

Graduate School of Engineering
Kyushu University, Fukuoka, Japan
September, 2021

To dedicate my Mother

Abstract

Zirconium nitride (ZrN) is a promising matrix candidate for advanced nuclear fuels and transmutation of minor actinides. In those applications, ZrN should subsist against radiations of energetic particles at high temperatures. Recent extensive researches have shown the excellent radiation resistance of ZrN under radiation environment. However, at present, information on fundamental properties of point defects, such as the production and their kinetic behavior, is limited. For example, no values are available for the displacement threshold energy (E_d) of ZrN, although this is an indispensable physical quantity to understand the radiation damage.

This thesis investigated fundamental properties of point defects in ZrN. First, values of E_d were evaluated by using *ab-initio* molecular dynamics (AIMD) simulation. Then *in-situ* microstructure observations were performed under electron irradiation in a high voltage electron microscope. Based on the evaluated values of E_d, the nucleation-and-growth process of defect clusters in ZrN was analyzed as a function of electron energy and irradiation temperature to understand the nature of defect clusters and the migration energy of point defects. Microstructure change irradiated with swift heavy ions was also investigated to evaluate the influence of high density electronic excitation. This dissertation consists of seven chapters.

Chapter 1 describes the research purpose of this study, and step-wise organization of the chapters is also outlined.

Chapter 2 reviews theoretical and experimental investigations on radiation damage in ceramic materials, with an emphasis on nitrides.

Chapter 3 describes experimental details, such as for ZrN specimen preparation, electron and ion irradiation conditions. *In situ* TEM observation conditions and data acquisition procedure are also described.

Chapter 4 describes the evaluation of E_d in ZrN by using AIMD simulation technique. Values of E_d were dependent on types of atoms (Zr and N atom) and crystallographic directions. The weighted average values of E_d for crystallographic directions were evaluated to be 33 eV and 29 eV for Zr and N atoms, respectively. Detailed monitoring of primary knock-on atoms (PKAs) during the collision process disclosed an important role of the sequential replacement collision in the [110] direction. Different configurations of interstitials between Zr and N atoms were attributed to the difference in E_d values on types of atoms.

In Chapter 5, the nucleation-and-growth of defect clusters is investigated as functions of electron energy and temperatures. Electrons with 1250 keV induced stoichiometric dislocation loops with Burgers vector parallel to <110> directions. Migration energy of interstitial atoms for the rate controlling species was evaluated to be 0.48 ± 0.07 eV. On the other hand, electron irradiation with 400 - 800 keV was found to induce nonstoichiometric dislocation loops, presumably consist of solely N atoms. A role of selective displacement damage of N atoms at electron energy below 800 keV is discussed for the energy dependent dislocation loop formation in ZrN.

Chapter 6, deals with microstructure change of ZrN irradiated with swift heavy ions. No ion tracks were formed under irradiation of 200 MeV Xe ions, which indicates the excellent resistance of ZrN to electronic excitation damage. On the other hand, different types of defects were formed dependent on the penetration depth of incident ions: dislocation lines and small dot-contrast were observed at shallow and deep depth, respectively. Those microstructure change was attributed to the change in the electronic stopping power against the penetration depth of incident ions.

In Chapter 7, important findings obtained from simulation and experimental investigations in this study were summarized as conclusions. Possible directions of researches for further understanding of defects behavior in ZrN were also highlighted.

Acknowledgements

Parise to be Allah, His majesty for His uncountable blessings, and best prayers and peace be unto His best messenger Mohammad (Sm.), his pure descendant, and his family and his noble companions.

First and foremost, I want to express my gratitude to Prof. Kazuhiro Yasuda, my thesis supervisor, whose intelligence, diligence, enthusiasm and philosophy have had a significant impact on me, not only in my research but also in my daily life. Success of the present study is due to his wise counsel and timely advice on prioritizing the tasks at hand. He provided me with a comfortable environment at workplace and much needed freedom to carry out my research work. Being a resourceful man, he has been instrumental in connecting me with the right person at various phases of my Ph.D. Interactions with him have helped widen my perspective in multiple aspects of life. I hope to continue these interactions and get opportunities to work with him in the future as well.

I am also honored to have Prof. Syo Matsumura is one of member in our research team, and my thesis committee as well. His diverse expertise and perspectives have greatly enriched my educational and research experience. Professor Matsumura provided me with very helpful insights on the discrepancies my theoretical and experimental result in ZrN under different irradiation conditions and valuable suggestions on the importance of simulation works in scattering cross-sections of different species of that ceramic material.

I would like to thank Prof. Jean-Marc Costantini one of our research collaborators, his inevitable advice to improve writing manuscript for both experimental and theoretical observation in our research.

I would like to thank Prof. Hideo Watanabe, member of my thesis committee for his invaluable advice and comments on both my research and future research directions.

I would like to acknowledge my collaborators and friends, especially Asst. Prof. Tomokazu Yamamoto, who were actively involved in all the theoretical simulations and experimental sessions of my research. Asst. Prof. Yamamoto's intelligence and diligent work in simulations and *in situ* observation of microstructure evolution has deepened my understanding of the behavior of ZrN under adverse irradiation conditions in a more broadened way. He also provided generous support and help in preparing for the scientific conferences and writing research articles.

I would also like to express my indebt to Prof. Yasukazu Murakami and Asst. Prof. Satoru Yoshioka, members of Matsumura Lab, for their valuable suggestions and discussion during monthly update meetings of the laboratory.

I would also give special thanks to Dr. S. Takaki and Dr. M. Takano from JAEA to prepare high quality ZrN specimens in the present study.

I would also like to acknowledge the members of Matsumura Lab, who are the friendliest people I met ever. My life in Japan became very convenient and comfortable due to the help and support I got from the lab-mates. I got to learn Japanese by spending time in the laboratory and I used that knowledge in my daily life out of campus, though I didn't dare to speak Japanese in the lab meetings!

I would like to thank my friends too, especially Dr. A. Z. Zia Uddin (department of theoretical Physics, University of Dhaka), Seo pooreun, Y. Yamaguchi, Dr. Xuan Quy Tran, Dr. Matair Rahman, Dr. Dr. Amirul Islam Toha, Dr. A. K. M. Saiful Islam Bhuian, Mr Md. Kamruzzaman, Dr. Md. Moshikur Rahman, Mr. Md.Shadat Hosen, who provided me mental stanchion to overcome the hardship during the beginning of my life in Japan and till to the end as well. The friendship I developed here is an unforgettable memory. They gave me great support and encouragement for my research here. They also offered their generosity during my tough time in daily life in Japan.

My gratitude and gratefulness are due to my beloved parents, sisters, for their blessings, love, and spiritual supports in all aspect of my life. It's beyond my words to express how much indebt I am for their invaluable sacrifices since beginning to this stage.

I gratefully acknowledge the funding sources that made my doctoral work possible. I would like to thank the govt. of Japan for providing me with prestigious Monbukagakusho (MEXT) scholarship throughout my study period in Kyushu University. I would also like to take this opportunity to thank the authority of Jagannath University, Department of Physics, Dhaka, Bangladesh, for allowing me to pursue my higher studies at the state-of-the-art research facilities of Kyushu University, Japan.

Contents

List of Figures

List of Tables

Nomenclature

ADS : Accelerator Driven System

AIMD : *Ab-initio* molecular dynamics

ASE : Atomic simulation environment

ATF : accident torelant fuel

BF : Bright field

CMD : Classical molecular dynamic

CCD: Charged coupled device

DFT : Density functional theory

DF : Dark field

E_d : Threshold displacement energy

FR : Fast reactor

g.b : Diffraction burger

GGA : Generalized gradient approximation

HVEM : high voltage electron microscope

HAADF : High-angle annular dark field

IFFT : Inverse fast Fourier transform

IMF : Inert matrix fuel

I_N : Interstitial of N atom

I_{Zr} : Interstitial of Zr atom

JAEA : Japan Atomic Energy Agency

LLFPs : long life fission products

MAs : minor actinides

MD : Molecular dynamic

NFFs : Nuclear fission fuels

NPPs : Nuclear power plants

NVE : Number of particles, volume, energy

PBE : Perdew, Burke, and Ernzerhof

PBCs : Periodic boundary conditions

PKA : Primary knock on atom

SA : Sudden approximation

SAD : Selected area diffraction

SCF : Self-consistent field

SHI : Swift heavy ion

SRIM : Stopping and Range of Ions in Matter

STEM: Scanning transmission electron microscope

TEM: Transmission electron microscope

TRU : Transuranium actinide

UN : Uranium mononitride

V_N : Vacancy of N atom

V_{Zr} : Vacancy of Zr atom

WBDF : Weak beam dark field

WC : Tungsten carbide

XRD : X-ray diffraction analysis

ZrN : Zirconium nitride

σ_d : Displacement cross-section

Chapter 1

Introduction

Radiation has been used in numerous human life areas, including academia, medicine, agriculture, industry, and, most notably, for electricity production development since its innovation in the 1890s. Nowadays, society is going through great scientific and industrial signs of progress; thus, we have needed a clean, consistent economy and uninterruptable electricity source for viable development. Eventually, nuclear power plants (NPPs) have become the most desirable option for the development of modern and sustainable society. As shown in Figure 1.1, at present, about 450 commercial NPPs are in operation in 30 countries. Moreover, about 53 NPPs are under construction in 19 countries, as shown in Figure 1.2. On the other hand, 178 nuclear power plants will be permanently shut-down, as shown in Figure 1.3 in about 20 countries in the world [1].

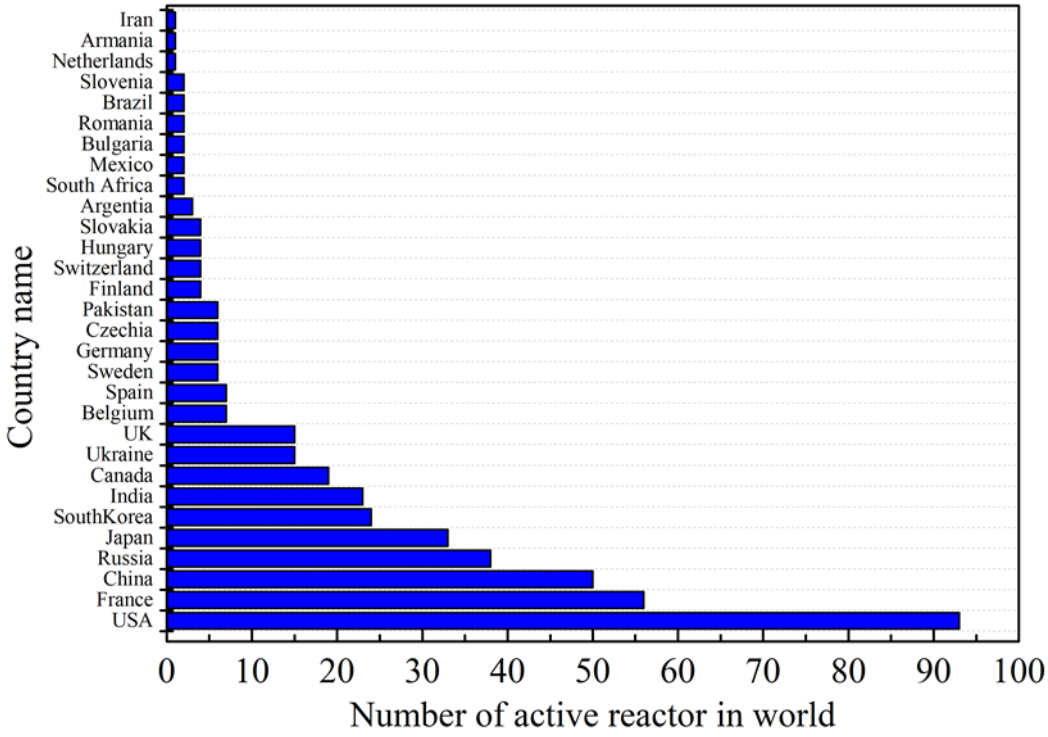

Figure 1.1 Total numbers of NPPs in operation in the world.

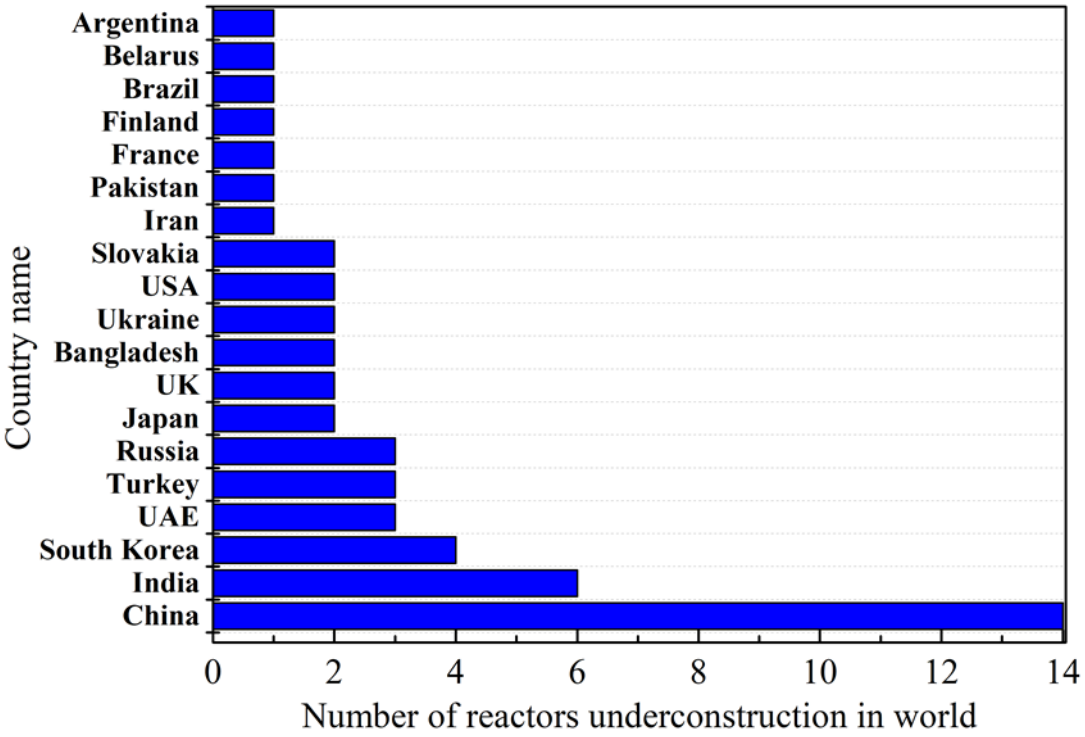

Figure 1.2 Total numbers of NPPs under construction in the world.

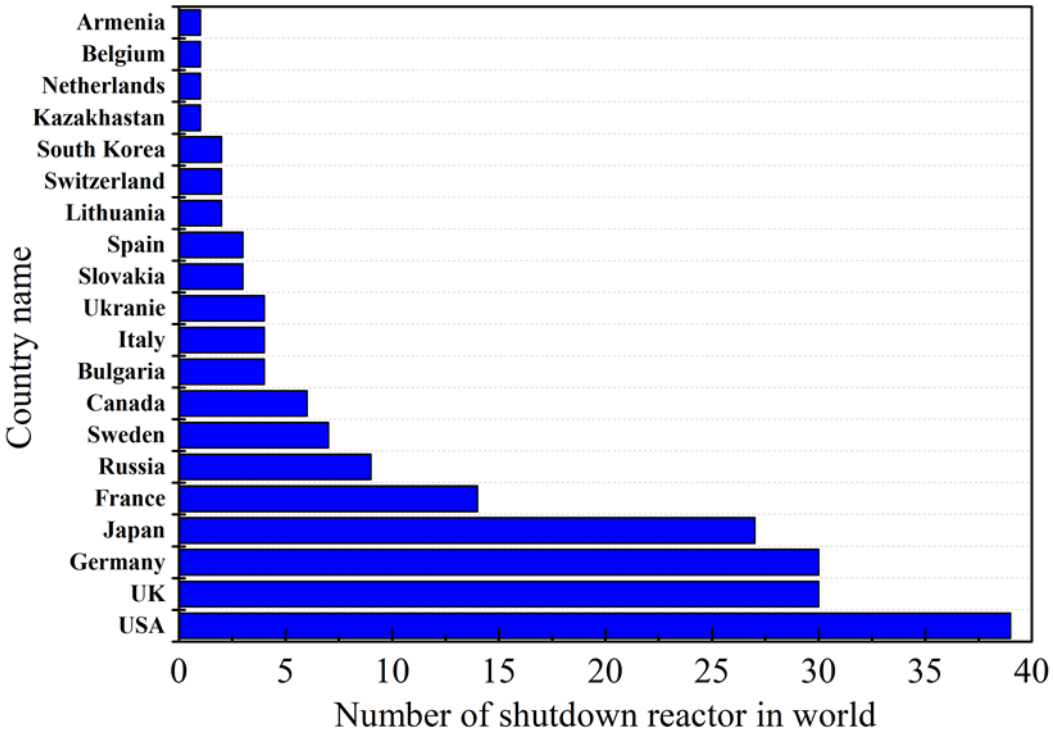

Figure 1.3 Total numbers of NPPs in Permanent shutdown in the world.

This thesis deals with fundamental radiation damage response in zirconium nitride (ZrN). ZrN is a rock-salt structure compound known as a radiation-resistant material with excellent physical and chemical properties, such as high melting point, superior hardness, low vapour pressure, and high thermal conductivity, and excellent compatibility [2–4]. This compounds attracts significant interest mainly by the following three reasons. Firstly, it is expected as an inert matrix fuel for Accelerator Driven System (ADS) reactor to burn plutonium and/or other minor actinides. Secondly, it can be used as a target material for the transmutation of minor actinides such as Np, Am, and Cm, and long life fission products (LLFPs). Due to the similar atomic radii and chemical similarities between the actinide elements and zirconium, the radiation tolerance of ZrN may be used as a predictor for the tolerance of nitride compounds including TRU to fission products [5,6]. Third reason is related to the second reason. As it is isostructural with UN, ThN, and PuN, ZrN has been used as a surrogate material for fundamental research works evaluating nuclear fuel and inert matrices' performance in a harsh radiation environment.

The disaster occurred at Fukushima Daiichi Nuclear Power Plant in 2011 was reported caused by the loss of water coolant in the reactor core. The significant oxidation of zircaly cladding materials generated hydrogen gases to lead the hydrogen explosion. The developing of new cladding/fuel materials having a high resistant to oxidation, called as accident torelant fuel (ATF), is now one of the important technical issues for the research of nuclear materials. On the other hand, in the ADS reactor, a coolant of liquid Pb or Na will be used, so that non-condensable gas will be removed easily from the inside of the reactor. As a result, there is no possibility of producing H_2 gas in the ADS reactor. The distinctive characteristic is considered to be used as diluent for inert matrix fuels (IMFs), which burn plutonium and other actinides instead of uranium, reducing actinide inventory in spent fuel in ADS reactor.

For this reason, nuclear scientists suggested a developed nitride nuclear fuel and ADS reactor. The manufacturing of new type nuclear fuel is not an easy task. At first, some parameters need developing for any nuclear fuel, such as swiftly swelling energy ingesting, the growing consumed nuclear fuel stock, and the global pressure to lessen the lifetime of radioactive waste. The concentration in commercial fast reactor technology has been improved. The technical inclination of nitride fuels suffers in the core from the lack of research, as the costs for the latter have been difficult to persuade, in light of readily available cheaper oxide fuels. Even today, the attained knowledge of nitride fuel manufacture and operation is derived from a tiny number of isolated research works. Since substitute fuel types retain desirable features, particularly with esteem to oxides, they have been frequently researched in the background. While not developed enough to be engaged in a commercial power reactor, it could be disputed that nitride fuels have been established sufficiently to deliberate their application shortly. In literature, minimal information was found about nitride type nuclear fuel task.

In NPPs, controlled fission reactions are performed to provide energy meanderingly to drive a steam turbine. The materials elaborate in the nuclear industry are exposed to austere adverse environs concerning high temperature and intense radiation fluxes of different kinds, e.g., energetic fast neutrons and gamma rays, alpha particles, electrons, and various kinds of fission fragments [7,8]. These could reduce the chemical and physical properties of those materials through elastic displacement damage and inelastic electronic excitations. Thus, the study of radiation effects in materials, including defect nucleation, growth, and recovery of point defects under severe and complex radiation environment, has become of great interest for decades.

Because of the excellent properties of ZrN, irradiation studies on ZrN have been performed extensively for a few decades with energetic particles, such as with 2.6 MeV protons

[9], hundreds of keV heavy ions [4,10,11], and swift heavy ions [12,13] and with neutrons [14]. However, according to the author's knowledge, the fundamentals of the radiation damage process and kinetics of point defects in ZrN are not fully understood at the present moment. For example, the values of threshold displacement energy (E_d) has not been evaluated yet for ZrN, and information on the migration energies of vacancies and interstitials is also limited [15]. Previous reports, therefore, assumed the values of E_d as 40 eV for both Zr and N based on the value of Zr metal [4], or 35 eV for Zr and 25 eV for N [16] based on the estimation on ZrC [17], whose crystal structure is identical (rock-salt structure) to ZrN, obtained from the values of E_d in TaC from electrical resistivity measurements [18]. It is needless to say that the threshold displacement energy (E_d) is an essential parameter for any materials used in radiation environments. For this reason, this dissertation aimed to evaluate the threshold displacement energy of ZrN using *ab-initio* MD simulation methods. Recently, most of the theoretical researchers used *ab-initio* molecular dynamics simulation method. This method has a great advantage to the classical molecular simulation (CMD) method since it does not regain the evaluation of atomic potentials.

For the fundamental understanding of kinetic behavior of point defects, high-energy electron irradiation using a high voltage electron microscope (HVEM) can be a powerful tool, which allows one dynamical observations of the nucleation-and-growth-process of defects under the production of isolated Frenkel defects [19] . It is also important to note in ceramic compounds that values of E_d can be different from each sublattice (or be different from cations and anions), and this causes the unbalance of the production rate of point defects between cations and anions. Previous investigations showed the formation of non-stoichiometric dislocation loops in fluorite-type compounds, such as ceria (CeO_2) [20,21] and yttria-stabilized cubic zirconia (Y: ZrO_2) [22], which consists of solely with oxygen ions. However, at the present moment, there is very much limited information on the production and kinetics of point

defects in ZrN, such as nature of defect clusters and the migration energy of point defects. The present study, therefore, performed *in situ* observation of radiation-induced defects in ZrN under high energy electron irradiation in an HVEM at different irradiation temperatures. The nucleation-and-growth process of defect clusters was analyzed as functions of irradiation time and temperatures to gain insights into the fundamental properties of defects, such as the nature of defect clusters and the migration energy of point defect in ZrN.

It is also important to note that ZrN exists with non-stoichiometric compositions or ZrN_{1-x}. The above chemical formula suggests that there exist structural vacancies in the nitrogen sublattice. The production and kinetics of point defects in ZrN might be influenced from the existence of structural vacancies of N atoms under irradiation. The role of nonstoichiometric to the radiation response in ZrN has not been understood yet.

From the backgrounds mentioned above, it would be important to investigate the nucleation-and-growth of radiation-induced defects, such as dislocation loops, as function of electron energy and irradiation temperatures under electron irradiation in a HVEM. Microstructure change under ion irradiation is also of importance for the safety evaluation of ZrN as nuclear fuel and transmutation targets. This study investigated the microstructure change in ZrN irradiated with swift heavy ions to gain fundamental knowledge on the microstructure evolution by fission fragments.

This dissertation aims to investigate to fundamental radiation damage response of ZrN which is an important candidate for nuclear fuel in ADS reactor, and consists of seven chapters.

Chapter 1 describes the background and addresses the objective of this dissertation. Theoretical and experimental understandings of radiation effects on ZrN, including other nuclear materials, were reviewed in Chapter 2, based on the extensive previous experimental

and computational studies. Especially, heavy ion irradiation and *ab-initio* MD simulations are described.

Chapter 3 described the experimental techniques and methods used in this research. Sequential steps of ZrN specimen preparation, electron and ion irradiation procedure, and TEM observation techniques are described.

Chapter 4 shows the evaluation of the threshold displacement energy (E_d) in ZrN using *ab-initio* molecular dynamics (MD) simulation. Values of E_d were evaluated for different crystallographic directions for both N and Zr atoms. Collision process of primary knock-on atoms (PKAs) were monitored precisely to gain insights into the production of point defects in ZrN .

Chapter 5 presents the nucleation and growth processes of radiation-induced defects under different electron energy and irradiation temperatures. We also showed in this chapter, perfect stoichiometric dislocation loops were formed under high electron irradiation energy. For lower electron irradiation energy also showed nonstoichiometric dislocation loops were confirmed by High-resolution observation.

Chapter 6 described some preliminary results on subsequent the swift heavy ion-irradiated ZrN specimens. A high density electronic excitation irradiation was not found to induce ion tracks in ZrN. Microstructure change were investigated by cross section observations, and discuss the microstructure change as a function of electronic stopping power.

Finally, in chapter 7, main findings on the radiation response in ZrN was summarized, and an outline of future research possibilities to understand the defect formation mechanism and recovery process was addressed.

Chapter 2

Theoretical and Experimental background

2.1 Introduction

Materials are made of atoms and molecules. Atoms are stacked randomly in non-crystals, while the same atomic groups are arranged consistently with a periodicity in crystalline solids, except for inevitable interruptions, such as grain boundaries and lattice defects. However, in adverse thermal, mechanical, or irradiation conditions, crystals can undergo severe structural deterioration and changes in electrical, mechanical, and chemical properties. This chapter describes and discusses the nitride fuels for Accelerator Driven Systems (ADS) reactor, necessary information on ceramic materials and the crystal structure, previous studies of radiation defects in ZrN and other ceramics, such as oxides induced by different radiations and irradiation temperature. The understandings of threshold displacement energy in ceramic materials will also be described.

2.2 Nitride fuel

There are different types of nuclear power reactor fuel: nitride fuel, oxide fuel, carbide fuel, and metal fuel. This section describes characteristic features and properties of nitride fuel. The most popular nitride fuel refers to uranium mononitride (UN), or a solution of actinide nitrides, such as (U, X) N, where X is, for example, Pu, Am, and Cm, etc. Due to the possible use of nitrides for space propulsion, the first one has been mainly investigated [23], whereas the latter is more suitable as an ADS reactor fuel. Besides, uranium free nitride fuels, usually a stable solution between nitrides of transuranium actinide (TRU) and zirconium nitride, have

been studied in ADS for their possible use. Due to the high fissile nuclide density, or the low non-metal to metal atom ratio, nitrides are an appealing fuel choice for ADS. Nitrides have unique matches with metals, despite being refractory ceramic materials. In particular, high thermal and electrical conductivity are the merit of nitride fuel. Nitride fuels can, therefore, be maintained by linear ratings of up to 100 kW/m although a moderate linear heat rating is selected for the safe of pertion. The relatively hard neutron spectrum increases TRU's fissioning likelihood in nitride fuels, while better breeding efficiency can be applied to the higher neutron yield per fission.

The actinide nitrides are mutually soluble [24]. An additional advantage is their compatibility with liquid sodium and leads [25,26], cladding material [27,28]. However, as TRU nitrides appear to separate at the necessary sintering temperatures, the manufacture of nitride fuels is a major challenge [29]. Nitride fuel having a density with over 90% theoretical density, unlike oxide fuel, cannot be obtained with traditional sintering methods, due to the low diffusion rate of metal atoms in these materials. Nitride production is obstructed by the need to grip these materials in an inert environment because they react rapidly to form oxidation with air and moisture. A further safety issue is the pyrophoric activity of actinide nitride powders. The neutron economy would be weakened by the high-energy neutron capture cross-section of ^{14}N, and the radioactive ^{14}C isotope that would be formed by neutron absorption by ^{14}N and subsequent proton emission. Nitrogen gas used for the processing of fuel must also be increased to ^{15}N. As the natural sum of ^{15}N atom is 0.4 %, the cost is greatly enhanced. It has been estimated that, in the case of ADS nitride fuels, the enrichment of ^{15}N would increase the production price by only ~ 9% [30]. It was proposed that the performance of nitride fuels should be developed in solution with ZrN, as the solution is more stable at a high temperature [31,32]. Nitride fuel is likely to demonstrate reduced gas release and fuel expansion under irradiation at ZrN resolution [27,33]. In particular, if the ZrN segment in the inert matrix fuel reaches 40

mol%, the material's thermal conductivity is significantly higher [6]. It results lower thermal gradient over the fuel radius, according to Blank et al [34], and lead to reduce the release of fission gas and the amounts of swelling. Existing industrial systems could be pragmatic for reprocessing, depending on the fuel pin plan. Aqueous recovery systems have been tested for unirradiated mono-nitrides, which dissolve in nitric acid entirely and higher than oxides [35]. This method could be applied only to He-bonded fuel pins, whereas Na bonding would dictate the need for pre-processing. A large amount of oxygen and carbon impurities reduce the dissolution rate [35,36].

2.3 Crystal structure and ceramics

As mentioned earlier, in section 2.1, crystals are solids that periodically retain a long-range order. The crystals are categorized according to reference axes, which have a direction and magnitude, into six crystal families and seven crystal systems (Table 2.1) [37,38]. The reference axes are labelled as *a, b* and *c*, and the angles between the positive axes are α, β and γ. The positive axes are *a, b,* and *c,* where angle α lies between $+a$ and $+b$, β lies between $+b$ and $+c$, and γ lies between $+a$ and $+c$, as shown in Figure 2.1. Ceramic materials also belong to various crystal systems, but are more complex than metals. Ceramic compounds usually contain at least two and sometimes three or more elements with a combination of stronger bonds known as ionic and/or covalent bonds. These bonds gives a high elastic modulus and hardness, high melting point, low thermal expansion, and excellent chemical resistance of ceramic materials [39,40]. The crystal structure of zirconium nitride (ZrN), which is delt with this dissertation, is shown in Figure 2.2. As shown in Figure 2.2, it forms the rock-salt structure: the structure and stability of zirconium nitride will be discussed below.

2.4 ZrN: structure and stability

ZrN offers a relatively high thermal conductivity and a high melting point, and a cubic lattice structure, as summarized in Table 2.2 for the physical properties. This high-temperature refractory nitride is attractive due to its extensive uses in ceramic engineering and as a nitrogen sensor in fuel cells, metallurgy, and thermal barrier coating in engines. Most importantly, ZrN has also been reported as one of the most radiation-resistant ceramics for its excellent radiation stability characteristics and incorporating actinides readily as already written in Chapter 1.

Table 2.1 Crystal families and crystal systems

Crystal family	Crystal systems	Axial relationships
Isomeric	Cubic	$a = b = c, \alpha = \beta = \gamma = 90°$
Tetragonal	Tetragonal	$a = b \neq c, \alpha = \beta = \gamma = 90°$
Orthorhombic	Orthorhombic	$a \neq b \neq c, \alpha = \beta = \gamma = 90°$
Monoclinic	Monoclinic	$a \neq b \neq c, \alpha = 90, \beta \neq 90, \gamma = 90°$
Anorthic	Triclinic	$a \neq b \neq c, \alpha \neq 90, \beta \neq 90, \gamma \neq 90°$
Hexagonal	Hexagonal	$a = b \neq c, \alpha = \beta = 90°, \gamma = 120°$
Trigonal or Rhombohedral	hexagonal axes hexagonal axes	$a = b = c, \alpha = \beta = \gamma$; *or* $a' = b' \neq c', \alpha' = \beta' = 90, \gamma' = 120°$

In rock-salt structure, each Zr atom is located at the octahedral sites formed by six N atom and vice versa for N atoms or vacancies at the N atom site. Figure 2.3 shows the phase diagram of zirconium nitride. It is noted that ZrN exists with nonstoichiometric compositions or ZrN_{1-x}, where N vacancies exist in a relatively wide composition range. It is also noted that zirconium nitride forms a cubic structure at ambient pressure up the melting point.

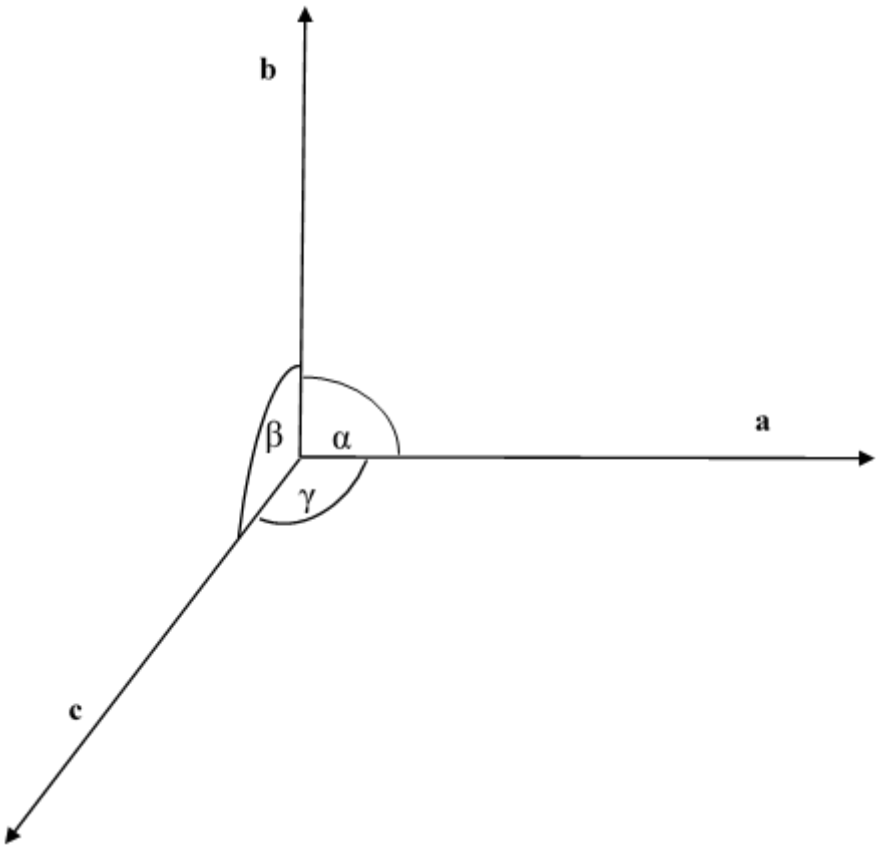

Figure 2.1 Seven crystal systems are characterized by the crystallographic axes a, b, c, and the angles between them, α, β, and γ.

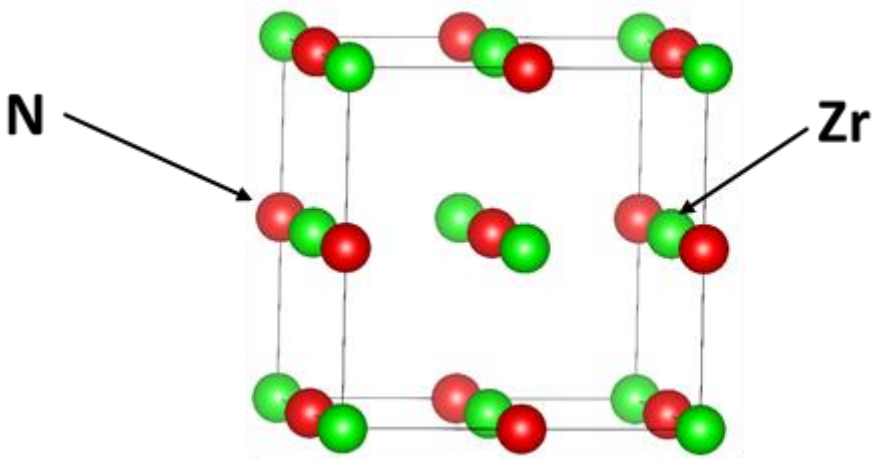

Figure 2.2 The rock-salt structure of the unit cell in ZrN.

Table 2.2 Summarized the physical properties of ZrN

Element	melting point	thermal conductivity	lattice parameter
ZrN	2980 °C	28 $Wm^{-1}K^{-1}$ (300K)	4.61 Å

2.5 ZrN: theoretical density calculation

The theoretical density of ZrN nitride ceramic can be found by calculating all atoms' mass in the unit cell [37]. The mass of an atom, m_A, is its molar mass (grams mol^{-1}) divided by the Avogadro constant, N_A, (6.02214×10^{23} mol^{-1}). m_A = molar mass/ N_A (grams). The total mass of all the atoms in the unit cell is then $(n_1m_1 + n_2m_2 + n_3m_3 + \ldots)/N_A$, where n_1 is the number of atoms of type 1 a molar mass of m_1, and so on. This can be written as a more compact form as-

$$\sum_{i=1}^{q} n_i m_i / N_i \tag{2.1}$$

where q is the unit cell of the different atoms.

The density, ρ is defined as-

$$\rho = \sum_{i=1}^{q} \left\{ \frac{n_i m_i}{N_i} \right\} / V \tag{2.2}$$

Here the theoretical density of ZrN is calculated to be 7.09 gcm^{-3}, according to equation ((2.2).

2.6 Radiation damage in materials

Zirconium nitride (ZrN) is one of the paramount research materials for inert matrix fuels (IMF) of the ADS reactor. Numerous irradiation experiments have been conducted in the past, but these researches have not been concentrated on aspects of nuclear fuel [41,42]. Some

experiments have focused on the irradiation of high energy protons [9,43]. Helium (He) desorption experiments provide the nature of the defects produced by heavy-ion [4]. Zirconium

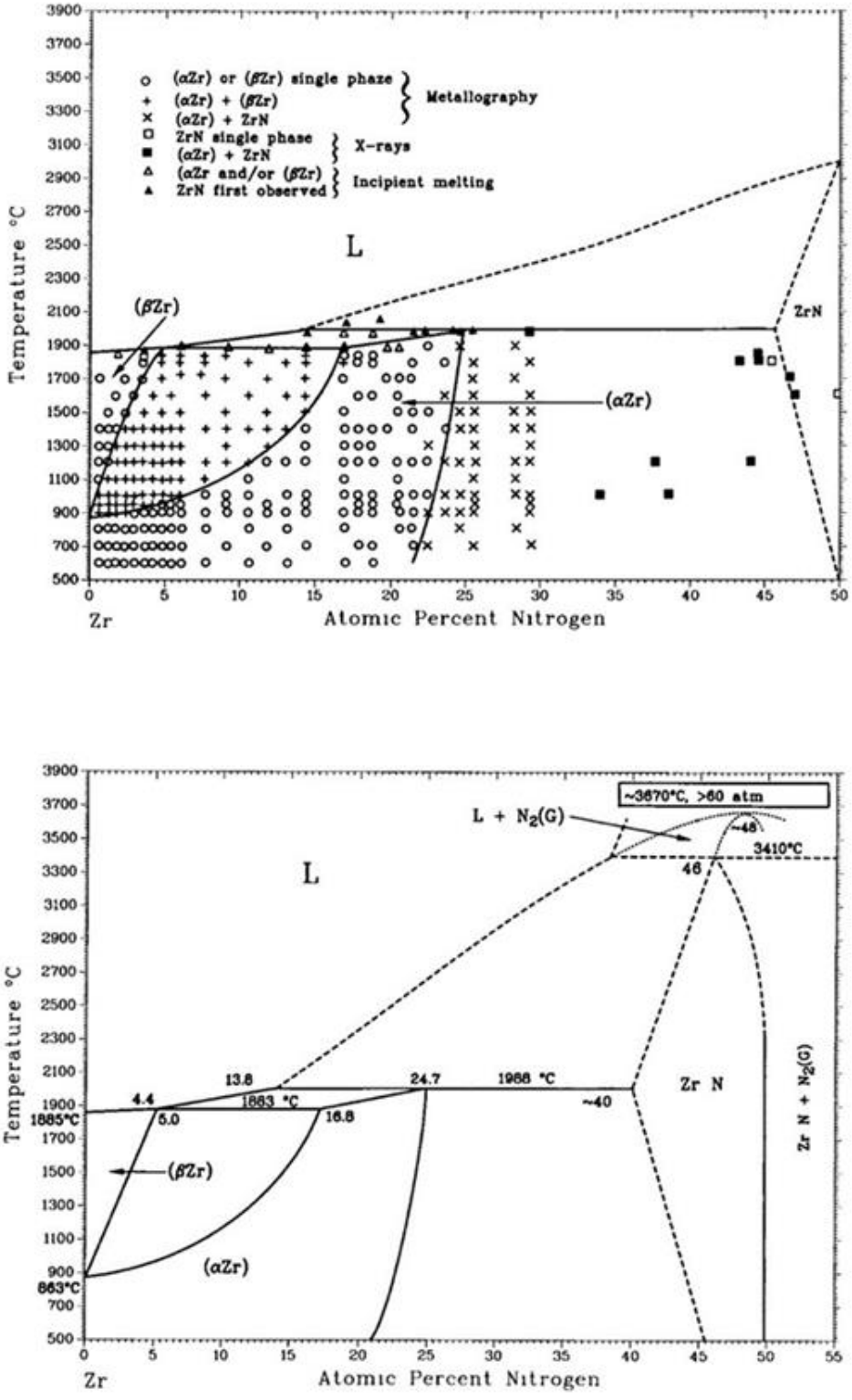

Figure 2.3 Experimental data for the Zr-N phase diagram (J. Phase Equli. Vol.15 No. 4 1994.

nitride has shown to keep cubic crystal structure under ion-irradiation at cryogenic and ambient temperatures to a very high displacement damage level of 200 dpa [4], which is a much higher than the necessary dose (25 dpa) to amorphization of magnesium aluminate spinel ($MgAl_2O_4$) [44]. Yang et al. investigated the structure change of ZrN irradiated with proton ions at relatively low doses of 0.35 and 0.75 dpa [9]. They showed that the irradiation damage appeared through the generation of dislocation loops and point defects clusters, and revealed that crystal lattice of ZrN was stable. The microstructural response of SiC, ZrC, and ZrN irradiated to proton irradiation was also investigated by Gan et al., showing that the ZrN was relatively stable than others [43].

Very recently, Ogarkov et al. and Kuzenetsov et al. [45,46] investigated the structure of ZrN irradiated with high energy Xe ions (167 MeV), they reported that no significant lattice damage was observed except for the distortion. Further, ZrN with nano sized grains was shown to possess significantly improved stability of structure against radiation damage, owing to the high density of interfaces and surfaces that provide sinks for the annihilation of radiation-induced defects [47].

2.7 Temperature dependence of radiation defects

Irradiation temperature has a very significant effect on the microstructural evolution of irradiated materials. In early experimental investigates in pure metals, measurements of electrical resistivity during isochronal annealing from liquid He temperature was used to classify five major recovery stages of point defects [48–51]. Figure 2.4 shows the defect recovery stages in copper irradiated with electrons at 4 K [52]. In general, the quantitative magnitude of the recovery of point defects at each stage depends on materials, its purity, the energies of PKAs and dose. The recovery process is categorized into five stages: the stage I

corresponds to the onset of the migration of self-interstitial atoms (SIAs) to recombine with vacancies from the same displacement event or uncorrelated defects from the primary displacement events. The stage II involves the migration of long range distance of interstitials to form small SIA clusters and SIA-impurity complexes. The stage III corresponds to the onset of the vacancy migration. The stage IV involves the formation of vacancy-impurity clusters, and the stage V corresponds to thermal dissociation of sessile vacancy clusters. Annealing Cu specimens with electron irradiation over a wide range temperatures, from 14 to 600 K, gives a different sub-stages (recovery stage) and migration energy of point defects, where properties and behaviors are different as summarized in ref. [53].

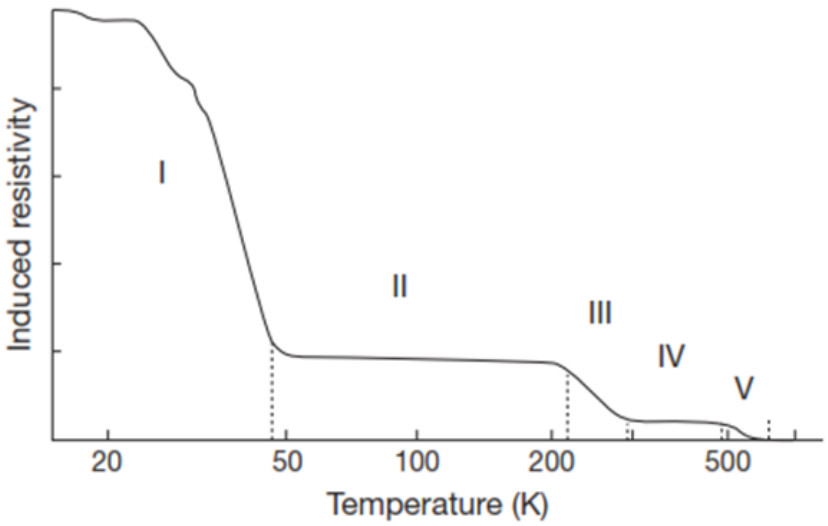

Figure 2.4 Electrical resistivity defect recovery stages for copper following electron irradiation at 4 K. Reproduced from Agullo-Lopez, F.; Catlow, C. R. A.; Townsend, P. D., Point Defects in Materials. Academic Press: San Diego, CA, 1988; p 445.

In some metals and ceramic oxides, the nucleation-and-growth processes of defects were investigated under electron irradiation in high-voltage electron microscopes. Kiritani et al. [54] investigated the nucleation-and-growth of interstitial-type dislocation loops to evaluate the migration of point defects in Al, Au, Cu, Fe, and Mo. They found that the migration rate of

vacancies regulates the growth speed of interstitial-type dislocation loops but not by that of interstitials. Further, they proved that the growth rate of loops in a thin specimen is directly proportional to the irradiation flux, and depends on the irradiation temperatures as explained by Yasunaga for CeO_2 et al. [20]. They were observed growth rate of perfect dislocation loops decreased with increasing temperatures.

For ZrN, Eggeland et al. [4] recently observed temperature dependence of radiation-induced defects irradiated with heavy-ions. They have observed cluster formation, atom de-trapping and the changes of defect microstructure at 623 K, 853 K and 1073 K. At the lower temperature of 623 K they showed the effect of 80 dpa Xe implant on the development of defect microstructure, and at 853 K vacancy-type defects were observed. The depth of penetration at 1073 K was observed 260 nm, and observed some defects are mobile. However, there has not been enough experimental investigations on the nucleation-and-growth of defect clusters in ZrN, nor those observations were explained by the nature of defect clusters and the migration energy of point defects.

2.8 Displacement cross-section (σ_d) and threshold displacement energy (E_d)

Electrons provided by transmission electron microscopes in the energy range of 400 keV to 1.25 MeV have been used to irradiate materials in the study of radiation damage. It has the dual benefit: one is the simple form of the damage production of Frenkel defects, and the other is the capability of *in situ* observation under the radiation damage circumstance [20]. In order to measure the likelihood of a fast electron displacing an atom in the material from its lattice position, the displacement cross-section between an electron and an atom in the target material must be understood. The electrons used in radiation damage study are in the relativistic velocity range, and as an infinite sequence of Legendre expansion. Mott [55–57] has articulated the

scattering between a point nucleus and an electron. Later McKinley et al. [58] simplified the theory. Legendre expansion, and the cross-section for Coulomb scattering by atomic nuclei of relativistic electrons was evaluated. The McKinley-Feshbach formula is the most commonly used, and it is expressed as follows [59]:

$$\sigma_{\text{tot}}(E, T_{\text{d}}) = \frac{\pi Z^2 e^4 (1-\beta^2)}{m^2 C^4 \beta^4} \left\{ \int_{T_d/T_m}^{1} \frac{dx}{x^2} \mathrm{M}(x, E) \right\}, \text{ if } T_{\text{d}} \leq T_{\text{m}} \leq 2T_{\text{d}} \tag{2.3}$$

$$= \frac{\pi Z^2 e^4 (1-\beta^2)}{m^2 C^4 \beta^4} \left\{ \int_{T_d/T_m}^{2T_d/T_m} \frac{M(x,E)}{x^2} dx + \int_{2T_d/T_m}^{1} \frac{T_m}{2T_d} \frac{M(x,E)}{x^2} dx \right\}, \quad \text{if } T_{\text{m}} \geq 2T_{\text{d}} \tag{2.4}$$

where E is the electron's kinetic energy, M the target atom's mass, T_m the maximum transferred energy, T_d the threshold displacement energy to displace an atom from its lattice site. (The notation of E_d is used for describing threshold displacement energy later on), $\beta^2 = E\,(E+mc^2) / (E+mc^2)^2$, Z the atomic number of the target nucleus, e the electronic charge, and $M(x, E)$ the ratio of the Mott to Rutherford cross-section, which can be calculated by using the method of Doggett and Spencer [60]. In recent days, a computer code named as SMOT/POLY code was developed that calculates the scattering cross-section, σ_d, versus electron energy for a given T_d value [61]. This code is explicitly designed for polyatomic targets where a significant contribution of the first elastic collisions and a minimal one of the secondary collisions with small collision cascades are included in the total cross-sections. It is noted that the displacement cross-sectional data for ZrN are not available in the literatures.

For the evaluation of E_d, several theoretical and experimental procedures have been used for different atomic sublattices in metals and ceramics. Electron irradiation sources were used to produce isolated Frenkel defects and measure the threshold displacement energy of sublattices. On the other hand, some experimental techniques, such as used optical

spectroscopy or EPR techniques were utilized to uniquely track the behavior of a specific type of defect, such as anion vacancies [62–64]. However, it has been stated that unless displacement damage occurs on both sublattices, the EPR or optical signals might not be visible [65]. Different theoretical methods for the evaluation of threshold displacement energies were developed: those are sudden approximation (SA) method [66], classical Mott-Littleton [67] approximation, or by the molecular dynamics (MD) method [68]. In recent years, *ab-initio* molecular dynamics methods, in which electronic structure calculations measure the forces acting on the nuclei rather than empirically equipped potentials, have proved to be a valuable instrument for gaining insight into defect configurations generated with *ab-initio* accuracy by low-energy recoil events [64,69–71]. In TEM studies, the measured threshold electron energy can be obtained by recognition of defect clusters. In ceramic materials with multi-sublattice, determination of E_d is not straightforward because of the multiple displacement and selective displacement damage.

The threshold displacement energy, E_d, can be bracketed by the following well-known equation [63,72].

$$E_d = \frac{2E_e(E_e+2m_ec^2)}{mc^2} = \frac{2147.7E_e(E_e+1.022)}{A} \quad [\text{eV}] \qquad (2.5)$$

where E_d is in eV, E_e is the incident electron energy in MeV, and A is the atomic mass of the displaced ion on the right side of equation (2.5). Aggregation of displaced point defects is dependent on the materials, and thereby the evaluation of E_d has not been fully achieved at this moment as described above.

2.9 Molecular dynamics (MD) and density functional theory (DFT)

Molecular dynamics simulation is one of the vital tools to investigate atomic behavior since the 1950s. MD have different assumptions about the materials being simulated, one of

them hard-sphere model. Recently, this model was described by Monte Carlo methods. Another key assumption is that the force between atoms can be defined as force fields. This model is known as the interatomic interaction model. Table 2.3 shows that significantly develop in MD simulations. Early on, in the 1960s, some physical models were used to investigate hard spheres connected with sticks. Nowadays, the dynamics of crystals are investigated with charged particles to represent atoms. In 1953, Metropolis et al. first investigated equations of motion by using MD methods. The Monte Carlo simulation proposed by Metroplis was developed advances computational system, which is suitable for numerically to analyze a liquid of two-dimensional spheres [73]. Expanding this simulation technique was achieved by Fermi, Pasta, and Ulam in 1955 and later.

2.9.1 Historical context of MD

The Vineyard group at Brookhaven Lab. analysis is the most relevant work, which was presented titled by" dynamic of radiation damage." The radiation damage phenomena was observed up to 400 eV PKA for copper system by Gibson et al. [74]. This was the first investigated radiation damage in a crystalline material using the classical MD approach. In their case, they used a Born-Mayer potential to correlate the repulsive force between atoms in addition to a cohesive surface force. The methodology used in that simulation is very similar to that is used today for calculating threshold displacement energies [74].

In 1964, Rahman investigated the simulation of liquid Ar by using a Lennard-Jones potential. The Lennard-Jones potential describes the interatomic interaction of noble gases, and calculated properties were in good agreement with experimental data [75]. In the early 1970s, the computational techniques were more advanced to describe several ensembles in molecular systems. However, Andersen's major work in 1980s, and later Parrinello and Rahman made

frameworks with use of ensembles [76]. The latest significant development was advanced molecular dynamics in 1985 work by Car and Parrinello, which combined DFT and MD [77]. It is important to note that advanced primary methods are established for computational physics and materials science to interrelate between two techniques.

Table 2.3 To develop a timeline in molecular dynamic simulations.

Year	Work	Author
1953	The fast computing machines to calculate equation of the state [78]	Metropolis et al
1955	Los Alamos report [73]	Fermi, Pasta, and Ulam
1956	To calculate phase transitions for a hard-sphere system [79]	Alder and Wainwright
1960	Dynamics of radiation damage [74]	The Vineyard group
1964	The motion of atoms in Liquid Argon [75]	Rahman
1971	Molecular Dynamics study of Liquid Water [80]	Rahman and Stillinger
1972	The Monte Carlo calculations for binary liquid Mixtures by using NPT ensemble [81]	McDonald
1980	Molecular Dynamics study at constant temperature And Pressure [82]	Andersen
1980	The development of pair potentials and Crystal structure by Molecular Dynamics methods [76]	Parrinello and Rahman
1981	Polymorphic transitions in single crystals by new Molecular Dynamics methods" [83]	Parrinello and Rahman
1985	Unified approach for Molecular Dynamics and Density functional Theory [77]	Car and Parrinello

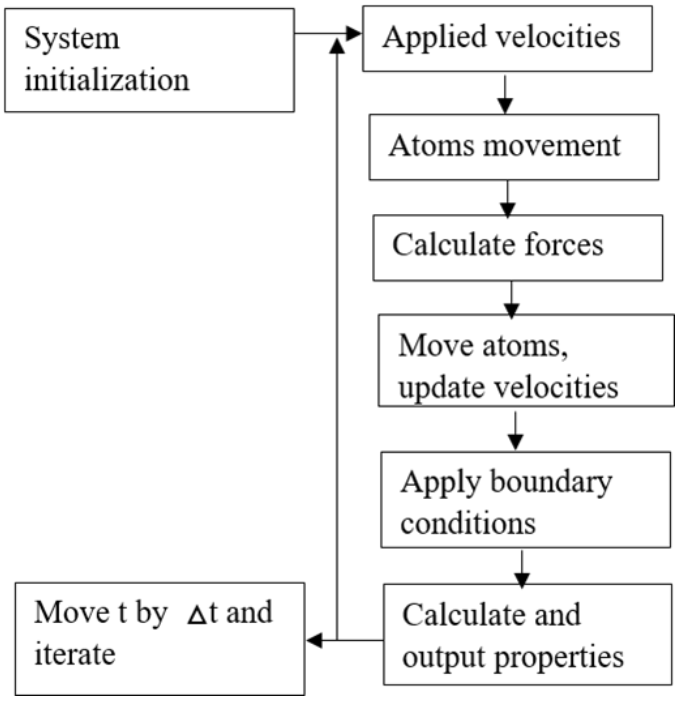

Figure 2.5 Basic flow chart for the molecular dynamics algorithm.

2.9.2 Classical molecular dynamics algorithm

Flow chart presented in Figure 2.5 shows that the essential steps for a classical molecular dynamics simulation. Firstly, the system is initialized (given an initial position, velocity, acceleration, charge, etc., for every atom). Then the atoms are moved based on the calculated interatomic forces. The new forces are calculated by using updated velocities. For this reason, atoms moved again, and then a boundary condition was applied. The based on boundary conditions and input parameters were calculated output properties for the allotted system. Finally, the time duration was defined for the whole system, and the simulation can move forward. Time step selection is essential for simulation because the integration of system properties is control by time steps. If the time step is so large, the integration of system properties does not converge. To avoid this shortcoming, we should test the system with

smaller time steps to ensure that it is the best for the system. Boundary conditions are also significant parameters for MD simulations. These boundaries are employed to isolate specific properties of the system and ensure certain thermodynamic properties are conserved. This dissertation used a periodic boundary condition. Table 2.4 shows major five types of boundary conditions are used in simulation systems.

Table 2.4 Different ensembles are defined, and the properties are kept constant.

Ensemble	Other names	Terms
NVE	micro-canonical	*N* (number of particles), *V* (volume), *E* (energy)
NVT	canonical	*N* (number of particles), *V* (volume), *T* (absolute temperature)
μVT	grand canonical	*μ* (chemical potential), *V* (volume), *T* (absolute temperature)
NPH	isoenthalpic-isobaric	*N* (number of particles), *P* (pressure), *H* (enthalpy)
NPT	isothermal-isobaric	*N* (number of particles), *P* (pressure), *T* (absolute temperature)

2.9.3 Density functional theory

The fundamental framework of density functional theory (DFT) is that the electron density's vital role play to generate all properties for a system [84]. The density functional theory assumes that the properties of the material can be determined by functionals (a function of another function) of the electron density. The algorithm operates by taking an initial electron density guess and following an iterative method that generates results that are self-consistent.

Once the input and outputs of the algorithm approach values within a specific tolerance, the result can be returned along with other calculated properties from that results. Once the values of the algorithm reach input and outputs within a specific tolerance, the result can be returned from that result along with other measured properties. The flow chart presented in Figure 2.6 shows a simplified of this method.

2.9.4 Historical context DFT

Table 2.5 shows a timeline of the main events in the development of DFT. The principle development was the Hartree self-consistent field (SCF) method in 1927; these methods were used to explain wave functions and ion energy approximations. The many-body time-independent Schrodinger equation was solved by Hartree fundamental principles. Fock was extended this method to ignore the initial approximation asymmetry of the wave function. Further simplification of the Hartree-Fock methods was later discovered and applied in the 1950s. However, it was not until the 1960s that the foundations of modern DFT were codified from the Hohenberg, Khon, and Sham methods. By introducing additional degrees of freedom to classical MD based on DFT, Car and Parrinello started working on unifying MD and DFT approaches in the 1980s. Recently, it has become practicable to simulate larger systems due to the increased availability of computing resources.

2.9.5 Density functional theory algorithm

The first approximation used is the Born-Oppenheimer approximation for simplifying calculations. The electrons travel much faster than the nuclei; thus, the electron and nuclear motion can be decoupled from each other [84]. During electronic structure measurements, the

nuclei are regarded as being fixed. *n(r)* is defined electron density, and $n(r)d^3r$ is the probability of an electron in the volume d^3r [85]. The electron density is

$$n(r) = \rho(r) = \sum_{i}^{N} \left|\varphi_i(r)\right|^2 \tag{2.6}$$

where $\varphi_i(r)$ is the single-electron wave function. The electron density $\rho(r)$ is the initial guess of the DFT algorithm to calculate a system's different properties, as shown in equation((2.6).

Table 2.5 Timeline of the related significant developments in density functional theory and quantum chemistry.

Year	Work	Author
1927	Hartree self-consistent field (SCF) methods [86]	Hartree
1951	Salter method to simplify the Hartree-Fock method [87]	Salter
1952	First use of Slater's method [88]	Pratt
1964	Inhomogeneous Electron Gas [89]	Hohenberg and Khon
1965	One electron exchange and correlation [90]	Khon and Sham
1966	First usage with an LDA pseudopotential of Khon-sham equations [91]	Tong and Sham
1985	Unified approach for Molecular dynamics and Density Functional Theory [77]	Car and Parrinello

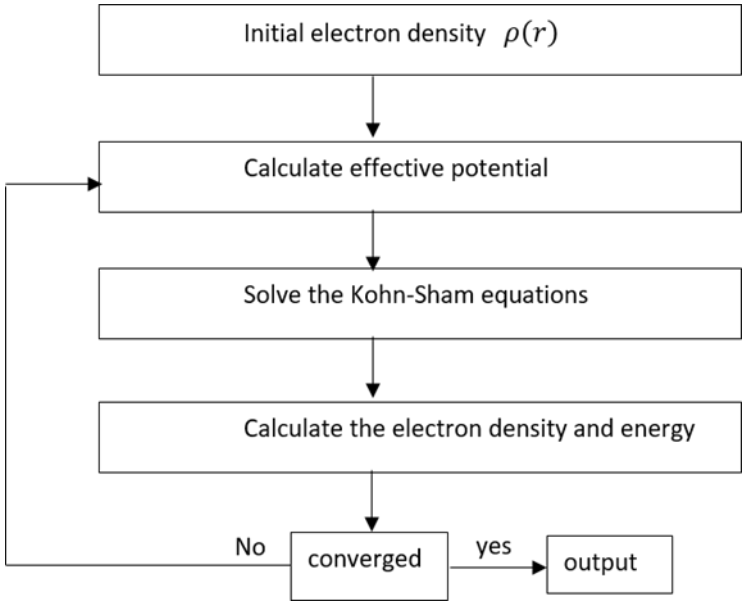

Figure 2.6 The algorithm of density functional theory.

$\rho(r)$ is determined as the summation of the probability of finding an electron based on each wave function, $\varphi_i(r)$. The effective potential is defined in equation ((2.7)

$$v_{eff}(r) = V_{en}(r) + \int \frac{\rho(r')}{|r - r'|} dr' + V_{xc}[\rho(r)] \tag{2.7}$$

as a function of both the electron density and the exchange-correlation terms, $V_{xc.}$ There are different ways to explain the exchange-correlation term in the system, and it is separated into two parts: one is the exchange, and another is a correlation. To solve the $v_{eff}(r)$ by using the following equation is

$$\left[-\frac{\hbar^2}{2m_e} + v_{eff}\right]\Psi_i = \varepsilon_i \Psi_i \tag{2.8}$$

Solving the equation (2.8 to find the new wave function which can be used to determine a new electron density is

$$\rho(r) = \sum_i |\Psi_i(r)|^2 \rightarrow E_{total}[\rho(r)] = \cdots, \quad (2.9)$$

The result is compared with the electron density from the first step, after evaluating the new electron density from equation ((2.9). The outcome and final properties can be calculated and recorded if they are within some convergence conditions set at the beginning of the calculation. The forces, pressure, total energy, eigenvalues of the wave equation, and more depending on the code parameters and the type of calculation, are among these properties.

2.9.6 Pseudopotential

There are additional steps involved with configuring the inputs while using the SIESTA code, namely the generation of appropriate pseudopotentials. A pseudopotential is a potential used to generate a wave function identical to the wave function generated by real atomic potentials, shown schematically in the Figure 2.7. The advantage of using a pseudopotential (introduced in 1934 by Hans Hellmann) is that it is a simpler form, and it is simpler to deal with the resulting wave function. The pseudopotential is built such that the core states of the all-electron (or full-potential) are omitted. The key advantage of this potential is the mathematically simpler definition of the valence electrons (fewer Fourier modes), making it feasible to use plane wave and other basis sets. In this case, the core electrons are viewed as frozen (they are known as the rigid ion core along with the nuclei) so that the valence electrons are the only ones that are specifically core considered. An auxiliary code for generating pseudopotentials is also included in SIESTA.

Table 2.6 A basic comparison of the basis sets form for DFT codes that are widely used.

Code	Basis set
VASP	Plane-wave (PW) [92]
SIESTA	LCAO (linear combination of atomic orbitals) [93]
ABINIT	PW [94]
CASTEP	PW [95]
Quantum ESPRESSO	PW [96]
WIEN2K	LAPW (linearized augmented plane wave) + LO (local orbital) [97]

The input consists of the atom, mass, orbital configuration, and occupation. There are different ways to define pseudopotentials and different approximations that are available to the user. Since testing the applicability of chosen pseudopotentials to the problem at hand is left to the end-user, it is sometimes a non-trivial task to generate the data required.

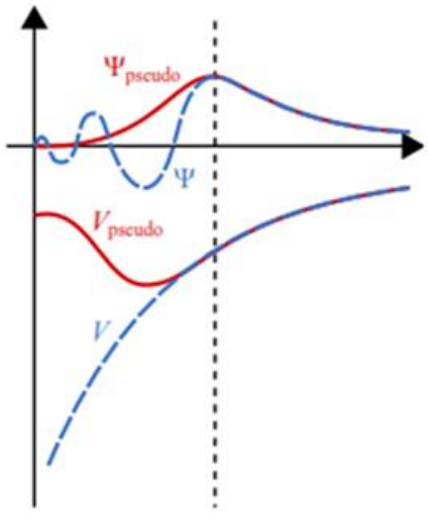

Figure 2.7 Schematic representation of the wave function and potential of an atomic potential and a pseudopotential [98].

For example, recent papers have attempted to produce better pseudopotentials that agree with VASP-based calculation results. SIESTA offers a database of LDA (local density approximation) and GGA (generalized gradient approximation) pseudo-potentials on its website. For any form of simulation, however, some of them are not properly designed, so it is essential to take the electron configurations and generate sufficient potentials from the bundled ATOM code (as of version 4.1, the ATOM code is not bundled directly with SIESTA for long; that version of the code is not used for the current work). Pseudopotentials are created by telling the code how far in space the different electron orbitals reach and the occupation of each valence orbital. Simulations using both electrons (core and valence) may also be performed but are unnecessary in most cases since the core electrons do not interact. In order to have empty atomic orbitals not included in the ones given by the database, generating a pseudopotential is often required; it is possible to create a custom one or change other simulation parameters. The primary problem with the formation of pseudopotentials in SIESTA is that there is no systematic development process. Recently, in the last five or so years, there has been a great deal of research into the creation of acceptable pseudopotentials for the SIESTA code. These efforts were designed to generate outcomes as similar as possible to other codes, most commonly VASP. This is particularly valid for heavier elements with several electrons and partially occupied orbitals of d and f valence. In particular, ZrN orbital configurations are significant for predicting how the atoms interact with the surrounding system; heavier cations need special attention.

2.9.7 Ab initio molecular dynamics

From both Table 2.2 and Table 2.4, It can be seen that both computational methodologies started to mature in the 1980s, with DFT gaining new approximations of exchange and

correlation and classical MD gaining viable methods with new thermostats to perform new types of dynamics. It was not far from combining the two, mainly due to the work of Car and Parrinello. However, computational strength has dawdled behind the theoretical frameworks. Large-scale simulations have recently become feasible, with the drastic increase in supercomputing resources' availability. Flow chart presented in has a force calculation step. Flow chart represents in Figure 2.6 can output forces. Combining these two components generates a beneficial synergy in which MD measures the position and motion of the atom, and DFT provides the interatomic forces in what is known as *ab initio* molecular dynamics or AIMD. AIMD simulations can be used in several codes.

The SIESTA 's built-in algorithms for dynamic simulations are used for the work discussed here. For running calculations, SIESTA offers a wide variety of ensembles, but the micro-canonical ensemble is used to ensure that the simulations can be performed within a reasonable period (see Table 2.2 for a partial list of ensembles; SIESTA is capable of running all the mentioned ones) [93]. The integrator used in the calculation of atom motion is also the simplest in the NVE (constant number of particles, constant length, and constant energy) ensemble, the velocity Verlet algorithm. Born-Oppenheimer and Car-Parrinello have two significant forms of AIMD [77]. Simulations based on Born-Oppenheimer use DFT to handle the forces and an MD algorithm of the user's choice to evaluate motion. Simulations based on Car-Parrinello leverage electronic as well as physical Degrees of freedom to perform calculations. Any type of dynamics can be more taxing to evaluate, depending on the intended use case. This work needs to understand how long it takes for the simulations to complete.

Since the AIMD used in the NVE ensemble only involves using DFT to generate the interatomic forces, a different code can also be written to serve as the MD calculator and take the forces from the calculations of the DFT. In the ASE (Atomic Simulation Environment)

python package and implementation of this is found [99]. The DFT measures in AIMD simulations take up the vast majority of computational complexity. Moving the atoms using the basic MD algorithm is far less computationally intensive.

It is necessary to eliminate as many variables as possible when simulating E_d events and to adjust parameters to minimize simulation time. Random velocities can lead to an increase in the energy needed to displace an atom from its lattice position, which is a concern since a longer simulation time results in more energy in the system [70,100,101]. Also, thermostats must be addressed when operating any other types of ensembles for atomic motion calculation. The atomic motion of the PKA and displaced atoms does not interfere with the thermostat in a PKA threshold displacement simulation since this would influence the effects of both the resulting defect structures and the energy needed to displace an atom. Because of this, the NVE ensemble is the clear option because, in addition to its lower computational cost, it does not rely on the thermostat for computing atom motion. With increased computing power availability, it is possible to perform AIMD-based calculations with more complicated materials.

Chapter 3

Experimental detail

3.1 Introduction

The transmission electron microscopy (TEM) has been developed as a very powerful tool for microstructural characterization of materials through the information of diffraction and structural images. High-energy electrons generated in a TEM lose their kinetic energy in materials through elastic and inelastic interactions, and they will cause elastic displacements of lattice atoms and electronic excitations in the specimen. In general, this feature might be a demerit of TEM since it induces damage in materials. On the other hand, this can be a great advantage for the irradiation damage study; it allows *in situ* observations of the nucleation-and-growth process of defect clusters in materials to discuss the kinetic behavior of point defects. This dissertation covers the nucleation-and-growth of radiation-induced defects in ZrN irradiated with high energy electrons at different energies and irradiation temperatures. The theoretical and experimental background of this research topic and the material of interest, ZrN, have been described in Chapter 2. This chapter will describe the basic principal of TEM, the specimen preparation procedure, and the experimental technique/condition used for data acquisition.

3.2 Transmission electron microscopy

A schematic diagram is presented in Figure 3.1 [102] to show the components of TEM. A high energy beam of electrons is allowed to pass through a thin specimen. Moreover, the interactions between the incident electrons and the nuclei of atoms and surrounding orbital

electrons can be used to observe features such as the crystal structure, features of microstructure like dislocations, chemical and elemental analysis, and so on. TEM has the same basic principles as optical microscopes but uses electrons instead of light. The achievable resolution for a wavelength λ is given by the diffraction limit δ [103] as the visible:

$$\delta = 0.61\frac{\lambda}{NA} \qquad 3.1$$

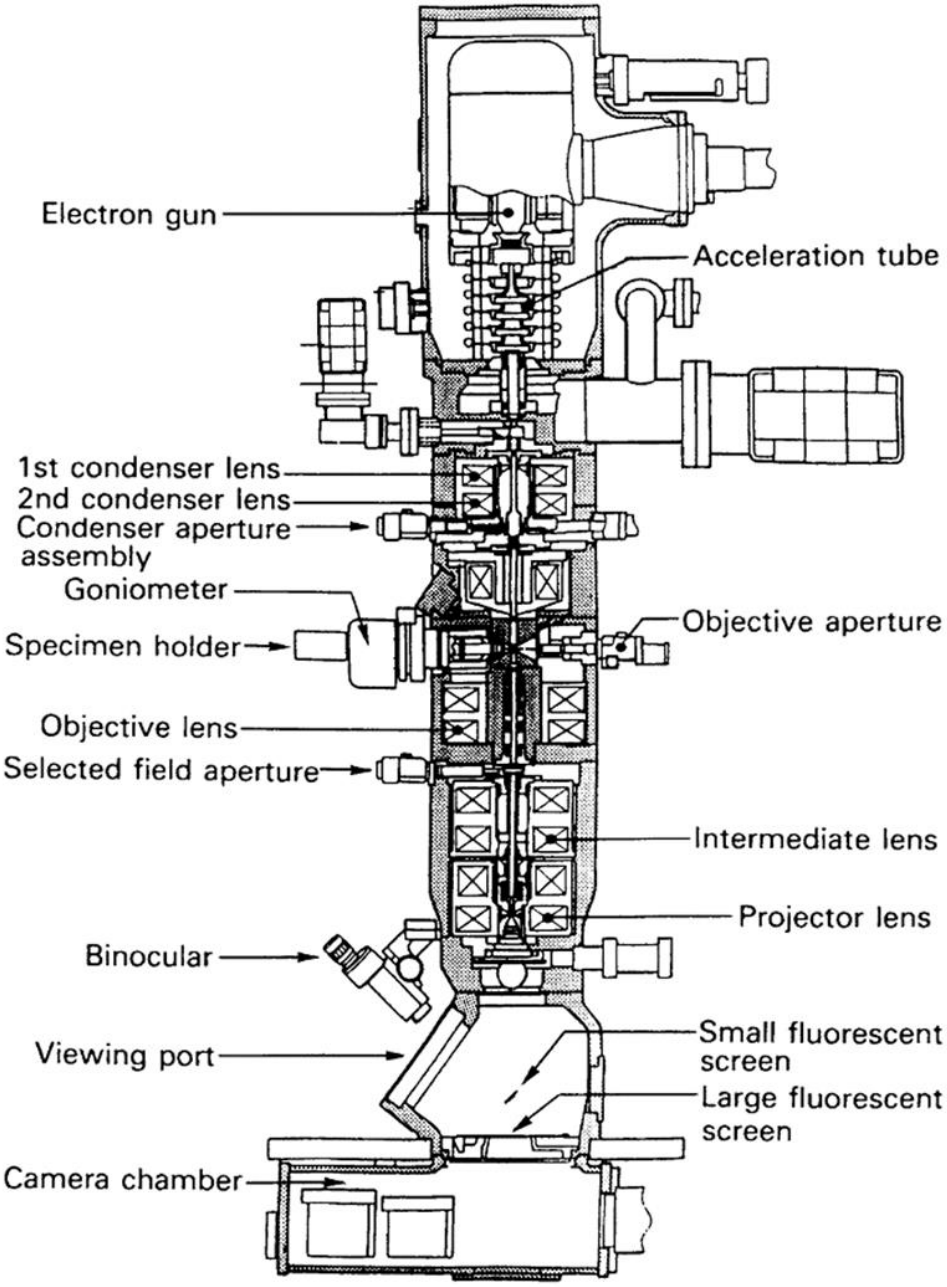

Figure 3.1 Schematic illustration of typical TEM with its components[102].

with numerical aperture, *NA*, which can be approximated by the angle of incidence $NA \approx \alpha \approx r_a/r_{wd}$, where r_a is the radius of the objective lens aperture and r_{wd} is the working distance. Optical microscopes can resolve with $\delta = 200\ nm$, but as the wavelength of electrons is much smaller than that of visible light, the optimal resolution achievable for TEM images is better than that of a light (optical) microscope. The TEM system uses electrical and magnetic fields to control the electron beam. The refraction law in optics is exchanged with Lorentz force in electrodynamics, but the electron optical system has similar diffraction limits as an optical system because they depend on the electron beam's wave nature [104]. The de Broglie wavelength λ of an electron with momentum p is given by

$$\lambda = \frac{h}{p} = h/\sqrt{2m_e E_b} \tag{3.2}$$

here h is Planck's constant. The electron has a rest mass m_e and energy, $E_e = m_e c^2 = 511$ keV . If an electron with charge q_e is accelerated from rest by an electrical potential U to the electron beam energy $E_b = q_e U$, it will have a wavelength of 1 nm at 1 eV decreasing to 1 pm at 100 keV, where it will be traveling with 50% of the speed of light.

The conventional bright-field (BF) and dark-field (DF) imaging techniques, as well as weak-beam dark-field (WBDF) imaging, are used in this research work. Figure 3.2 shows the ray's path in the image modes to form BF and DF images. The image found in the TEM study is formed by electron rays passing through the specimen. Instead of glass lenses, the TEM uses electromagnetic lenses to focus the electrons beam to be a small probe. Depending on the specimen's density and thickness, a part of the electrons are scattered and are interrupted by apertures inserted in the path of the electron beam. At the bottom of the microscope, the un-cutted electrons hit a fluorescent screen and/or a detecting camera such as a CCD camera,

which allows forming a shadow image of the specimen with its different parts displayed in varied darkness according to the electron intensity. It is noted here that all of the rays in the back focal plane is not necessary to form an image; preferably, a full image can be formed with only those rays passing through one point in the back focal plane. An image made with only those electrons that have been diffracted by a specific angle can be achieved by using an objective aperture at a specific location in the back focal plane. Thus, when the aperture is positioned to pass only the transmitted electrons, a bright-field (BF) image is formed, whereas a dark-field (DF) image is formed when the aperture is positioned to pass only some diffracted electrons.

The objective aperture is positioned to pass only the transmitted electrons, a bright-field (BF) image is formed, whereas a dark-field (DF) image is formed when the aperture is positioned to pass only some diffracted electrons. The features in an image originate from the diffraction contrast, which is the variation in the intensity of electron diffraction across the specimen. This diffraction contrast is achieved by inserting the objective aperture in the beam path. In the microscope, the typical size of the hole of objective apertures ranges from 0.5 to 20 μm in diameter. The aperture are movable with high mechanical precision and can be positioned around selected diffraction spots in the objective lens's back focal plane. In the diffraction mode, the image of both the diffraction pattern and the aperture is visible on the viewing screen, and the objective aperture can then be moved until it is in the desired position. When the objective aperture is positioned properly, the microscope is switched back into image mode, and either a dark-field or a bright-field image is formed. A second aperture named 'intermediate aperture' is positioned in the objective lens's image plane to confine the diffraction pattern to a selected area of the specimen. This technique is called 'selected area diffraction (SAD)'. The SAD pattern that appears on the viewing screen originates from the area of the

specimen selected in the image mode. The separation of the diffraction spots found in the SAD pattern can be used to determine the interplanar spacing in crystals. This technique is also used in this study to characterize the dislocation loops in irradiated ZrN specimens; the details of the SADP used will be discussed in later sections (Chapter 5).

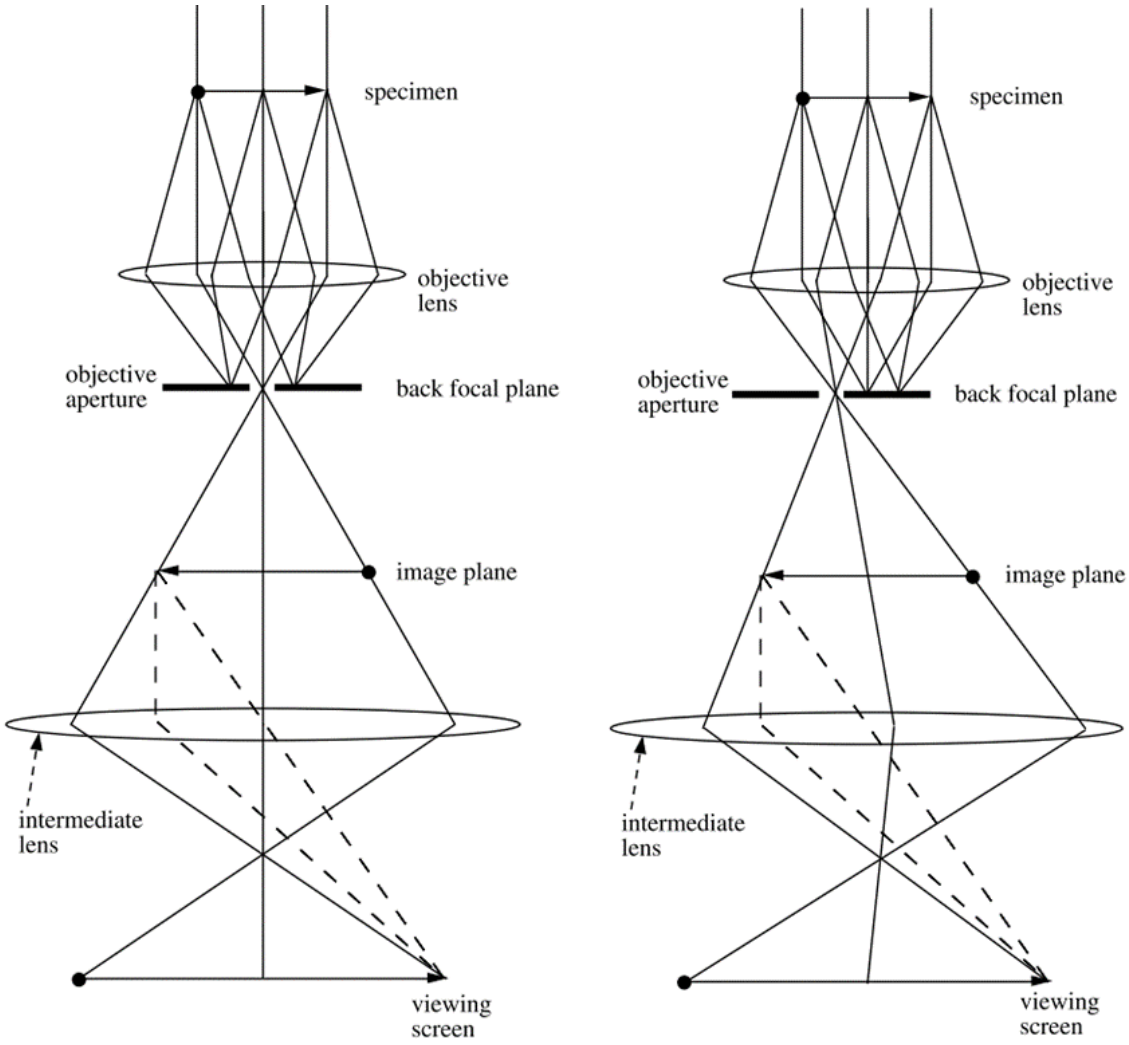

Figure 3.2 Ray path diagram of image formation in bright-field, BF (left) and dark-field, DF (right) mode [102].

The high voltage electron microscope Figure 3.3, which belong to The Ultra-microscopy Research Centre of Kyushu University, was used to perform *in situ* observation of radiation damage. Some characteristic features of HVEM are summarized in Table 3.1.

3.3 Specimen preparation

The sintered body of ZrN were provided by Dr. Seiya Takaki in Japan Atomic Energy Agency (JAEA). The procedure is described as follows in Figure 3.4: ZrN were prepared from corresponding metals through an intermediate synthesis of the hydride. A piece of Zr metals was heated at 963 K in a purified Ar-20% H_2 mixed gas flow for 20 h. The hydride was pulverized into coarse powders. These powders were heated at 1073 K for 1 h and 1573 K for 4 h in a purified N_2 gas flow and obtained the nitride powers.

The powders of ZrN nitride were ground by a high-speed planetary ball mill with a tungsten carbide (WC) pot and balls in order to ensure the homogenous and fine powders. The powders were molded at a pressure of 200 MPa and then loaded into an electric furnace.

Figure 3.3 JEM-1300NEF TEM (JEOL Ltd.) Ultra-microscopy Research Center, Kyushu University.

Table 3.1 Characteristic features of the HVEMs used in this research work

Specification	JEM-1300NEF (JEOL) Kyushu University
High Voltage	1.25 MeV
Stability of high voltage	8×10^{-7} min^{-1}
Cathode	LaB_6 single crystal
Beam current	Maximum 15 μA
Lens Configuration	Eight-step lens system; No image rotation
Magnification	×200 to 1,200,000
Resolution	0.12 nm
Spherical aberration coefficient	2.2 mm
Chromatic aberration coefficient	3.7 mm
Defocused point	Minimum 1 nm
Specimen Chamber Vacuum	2×10^{-6} Pa

The heat treatment for solid solution formation was performed at 1873 K for 6 h in the N_2 gas flow. The sintering pellets of the ZrN solid solution was obtained in a similar way to the solid solution preparation at 1973 K for 6 h in the N_2 gas flow. The sintered compacts were evaluated to be about 90% theoretical density with an average impurity oxygen concentration of 0.2 wt%, in which these values are similar to other samples prepared. Sample preparation for TEM is a long and involved process. The material has to be thinned to electron transparency, which is typically around 100 nm thick. Ceramic specimens, such as ZrN, can be very fragile, and the development of the final thinned sample must be done carefully.

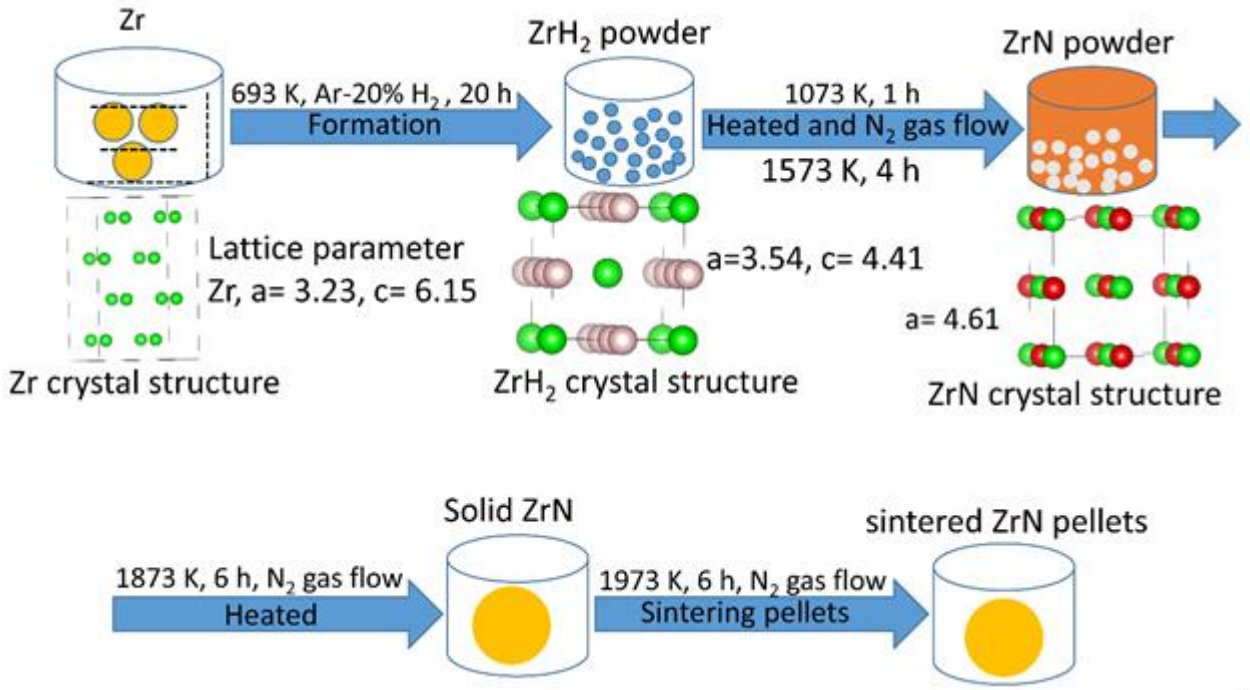

Figure 3.4 ZrN sample preparation flow chart.

Two methods for processing ZrN samples for TEM are used in the present study:

1. Conventional plan-view technique,
2. Cross-sectional view technique.

Each method provides different information. The plan-view sample is useful for *in-situ* observations of the virgin sample subjected to HVEM experiments, and also provides observations of ion-irradiated specimens from the direction parallel to the ion beam direction. This specimen preparation's weakness lies in the fact that there is no depth information of incident ions since it provides the projected image of all the transparent regions. On the other hand, the cross-sectional sample allows one the depth information of incident ions as the sample surface is observed at the edge.

3.3.1 Plan-view sample preparation

The sintered sample is glued to a sample holder block, and placed into an automatic

grinder/saw (Struers 1000, Refine Tec. Ltd.). The sintered sample was cut into 800 μm thickness and was polished with different sizes of SiC abrasive papers to reduce the thickness into 500 μm. The thinned samples were then glued to a slide glass, and a Gatan ultrasonic cutter is used to produce disk specimens with 3 mm in diameter. The 3 mm disk samples were polished to 150-160 μm in thickness by a mechanical process using fine oil diamond slurry (Musashino Denshi, INC.). The sample was then reduced to 20 μm in thickness by using a dimplier machine with a diamond past. The diamond past was used with different μm sizes of diamond particles, from 6 μm to 1 μm, with a glycerine lubricant. It is noted that during the cutting and polishing processes, water-based lubricants or polishing pastes were not used as far as possible but used oil-based ones, to prevent the absorption of hydrogen or OH- ions into the specimens. The final thinning step was done either by the ion thinning equipment of PIPS or Duo-Mill. The procedure for ion thinning will be described in Section 3.4.

3.3.2 Cross-sectional sample preparation

The cross-sectional TEM sample preparation procedure is much different from that for the conventional plan view sample. The 3 mm disk sample was cut in half so that there were two implanted faces. These faces were glued together with M-bond epoxy adhesive. The procedure for glue was done as follows: first, the specimen faces were thoroughly cleaned with acetone and ethanol. The premixed epoxy was kept refrigerated and must be pre-warmed for at least an hour to reduce the viscosity. A horse hair-brush was used to apply the glue by first wiping on filter paper to remove as much glue as possible. This has the effect of reducing the glue thickness between the two samples. The sample was then pressed face to face. Pieces of the silicon wafer were used on the opposite ends of the ZrN sample. They were cleaned and glued by the same method. This procedure finally made the sandwich, being virgin layer ZrN-

irradiated layer ZrN-virgin layer-ZrN, and it was placed into a vice and compressed with firm but gentle pressure to make M-bond squeezed out. In this condition, the sample was kept in an electric heater for at least 1 hour. The epoxied sample was glued to a glass slide and cut by a slow-speed diamond saw about 750 μm thick sample, which has the proper size of ≈3 mm in length and 1 mm in width. The thin slices were now laid down to show the edge-on view. The sample was then flattened on both sides by hand with a 15 μm diamond film. The diamond film used was Struers polycrystalline-diamond-impregnated diamond which is lubricated with oil. The sample was then polished by hand using diamond films with 15, 9, 6, 3, and finally 1 μm diamond on a wheel plate. Measurements of the sample thickness were taken during the polishing. These were used to view the extent of surface removal during polishing with the next film. Rotating the sample by 360° between each film facilitated observation of the previous film's scratches from the previous film under a low-power stereo microscope with top, side, and bottom lighting. With slow-to-moderate wheel speed, the tripod is moved in a circular motion no produce any parallel scratches. The sample was thinned, generally about 100 μm. The sample was thinned carefully to near 100 μm. The wax and oil were removed using acetone. The sample was then ion milled to perforation.

A TEM specimen must be thin enough to minimize the electron beam's diversity at the specimen's exit surface to form an image with appropriate short exposure time. TEM specimen preparation requires to keep the thickness of at least some regions of the specimen is within the thickness range of 10 nm to 1 μm. Practical details of the TEM specimen preparation technique are described elaborately in the textbooks [105,106] with a typical preparation sequence, such as ultrasonic disk cutting, dimpling, and ion-milling [107].

3.4 Ion milling procedure

The final thinning with ion mill technique was done either of a Gatan Duo-Mill or PIPS (Precision Ion Polishing System). The standard vacuum condition of Duo-Mill is < 8.3×10^{-5} torr. The Duo-Mill polishing has several steps to ion milling of specimens. The first step is to set the specimen at a beam incident angle of 10° with 6 keV of Ar ions. This condition was kept for 8-10 hours for ion-milling until creating a small hole in the sample surface. This condition was kept until the hole becomes at 200 μm in size. Secondly, the beam voltage was reduced to around 2 keV for 10 minutes at the minimum angle of 8°. In the third step, applying at 1 keV, the condition was kept for 30 minutes at the minimum angle of 7°. Finally, the argon gas damage was removed from the sample surface, with 0.5 keV for 30 minutes at the minimum angle of 7°. This equipment has a broader and dispersed ion beam and provides "gentle" milling of material. Hence, this equipment's sputtering rate is relatively slow, and it requires approximately 10 to 12 hours to make a thin-foil specimen for ZrN.

In the case of PIPS, the ion beam is much more intense than Duo-Mill, and the beam angle used is shallower, or 4° to 10°. The accelerating voltage was 5 keV, which produces very aggressive milling on the surface at angle 10°, so that it produces thin foil specimens within a short time. The PIPS has some advantages over the Duo-Mill; it has a shallow angle, reducing milling time. Its main disadvantages are that it can sputter material onto the sample and be too aggressive, such that it over mills the amorphous phase between grains preferentially. However, a final step polishing with reduced the accelerating voltage for 10 minutes acts to reduce this surface regions. The samples were thinned until perforation and then checked by light microscopy for its quality. When light microscopy showed sufficient quality, the sample was ready for TEM observations.

The cross-section specimens were prepared by a little differently recipe from plan-view specimens. Cross-section specimens were prepared using Ion Slicer (JOEL Ltd.) with 8 keV Ar-ion from a shallow angle 2.5 to the swift heavy-ion irradiation direction. After creating a small hole in the specimens, ion energy was reduced gradually to the final polishing energy of 1 keV, to minimize the Ar-ion damage. Then it was suitable to observe in TEM.

3.5 Irradiation conditions and data acquisition

3.5.1 In situ observation of defects in pristine ZrN

In situ observation of defect cluster formation and evolution of dislocation loops in pristine ZrN were performed at different irradiation temperatures from 873 to 1273 K with a range of constant incident electron energy 1.25 MeV. Irradiation experiments with 1.25 MeV electron energy were conducted by JEM-1300NEF (JEOL Ltd.) at The Ultra-microscopy Research Center of Kyushu University up to an electron flux of ~4.4×10^{22} $m^{-2}\cdot s^{-1}$. The electron irradiation was performed using a focused electron beam with a size of around 1-1.5 μm in diameter, which is assumed to be close to a Gaussian distribution. The nucleation-and-growth process was recorded *in situ* by bright-field (BF) TEM technique with a diffraction vector of $\boldsymbol{g}$ = 200. The details of the irradiation condition for pristine ZrN specimens are presented below. The $\boldsymbol{g.b}$ analysis of the dislocation loops at 1.25 MeV and 1173 K was performed to characterize the Burger's vector of loops. Electron beams illuminated near by along the <110> directions were used to check the visibility of dislocation loops at different *g* vectors.

3.5.2 Beam size and flux intensity measurement

The shape of the focused electron beam, used for *in situ* irradiation, was anticipated to be of a 2-dimensional Gaussian distribution [108]. The beam's shape Figure 3.5 and intensity

distribution was measured at an electron beam flux of $4.22 \times 10^{22} em^{-2}.s^{-1}$. The current was recorded with a Faraday cage at a distinct position of the electron beam, and then the electron flux at that position was calculated.

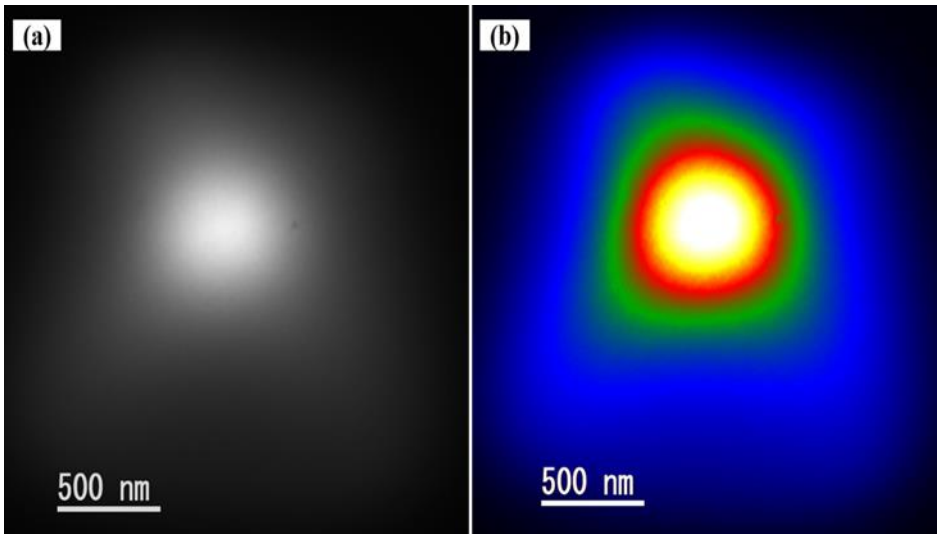

Figure 3.5 The electron beam size used in irradiation experiment in HVEM.

3.5.3 In situ observation of defect evolution in SHI ion-irradiated ZrN

Similar to the *in situ* observation of defect evolution under electron irradiation in pristine ZrN, the SHI-irradiated ZrN defects were also studied under the ambient temperature. ZrN specimens of around 150 μm thickness were prepared with the similar procedure described in section 3.3, and then, they were first subjected to (5×10^{15} m^{-2} and 5×10^{16} m^{-2}) Xe ion irradiation at room temperature to fluences of (5×10^{15} m^{-2} and 5×10^{16} m^{-2}) in Tandem Accelerator Facility at Japan Atomic Energy Agency-Tokai (JAEA) (Figure 3.6). Ion-irradiated ZrN specimens were subjected to the dimpling and ion-milling processes to prepare thin wedge-shaped foils suitable for TEM. The dimpling and ion-milling was done from the back side of the irradiated surface of specimen to observe the microstructure of the ion-irradiated region.

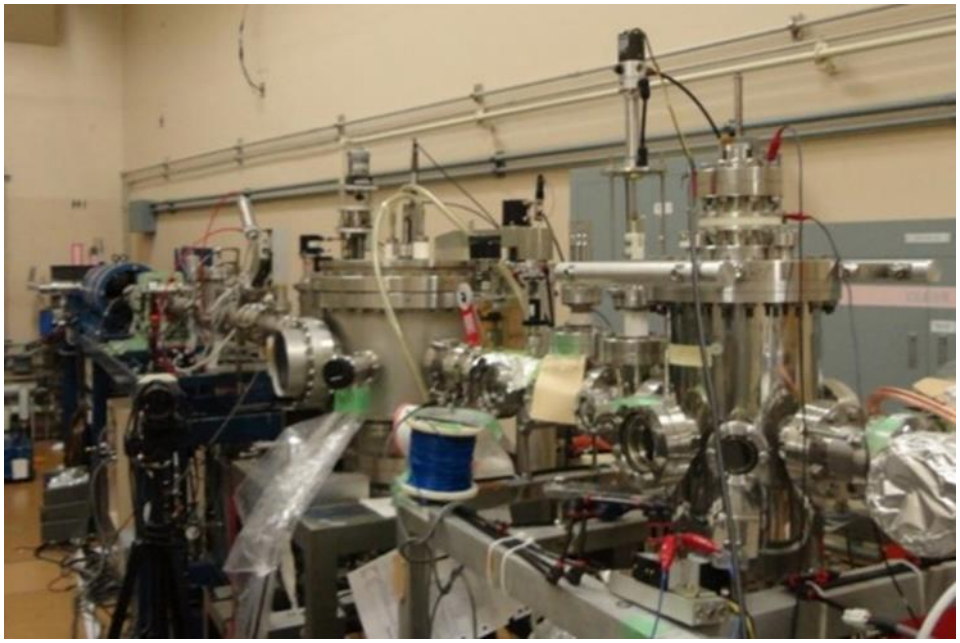

Figure 3.6 The Tandem accelerator in Japan Atomic Energy Agency (JAEA).

Chapter 4

Evaluation of threshold displacement energy by *Ab initio* molecular dynamics simulations

4.1 Introduction

The threshold displacement energy is one of the most important parameters to describe radiation effects in materials. As described in Chapter 1, however, information on the threshold displacement energy (E_d) in ZrN has not been reported in literatures. Further, when one perform ion irradiation experiments, E_d is the indispensable parameter for the evaluation of amounts of displacement damage (dpa) and concentration profile of implanted ions by using the Monte Carlo simulation code of SRIM [109]. Knowledge on the values of E_d for nitride compounds is unfortunately behind to other ceramic compounds, as values of E_d of some oxides and carbides are summarized in references [63,110–112]. Electrical resistivity measurements of the recovery process of electron irradiated TaC with the same rock-salt structure gave E_d values to be 42±2 eV for Ta and 28±6 eV for C [18]. Because of the lack of information for E_d in ZrN, previous investigations on ion-irradiated ZrN adopted E_d values of 35 eV for Zr and 25 eV for N [4,9,10,113] for the SRIM simulation, which is from the estimated values for ZrC [17] based on the reported values of TaC [18].

Ab-initio molecular dynamic (*ab-initio* MD, or AIMD) simulation provides an ideal tool to investigate the displacement energy, the formation and migration energy of point defects

in ceramic compounds [114,115]. It allows one to avoid the use of interatomic potentials, through which parts of substantial errors are introduced in the calculations for the estimation, such as values of E_d, with the classical molecular dynamics simulation [116]. Successful evaluations of E_d were reported using the AIMD technique, such as for ZrC [117], GaN [118], SiC [119], $Y_2Ti_2O_7$ [69], and fluorite oxides of ThO_2, CeO_2 and ZrO_2 [64]. AIMD also provides values of E_d with different orientations of primary knock-on atoms (PKAs). It is known that E_d is generally dependent on crystallographic orientations, especially for ceramic compounds with multiple sublattices and constituent atoms [64]. Information on the crystallographic directions is useful to understand the complicated collision process of ceramic compounds consist of multiple sublattices, and also indispensable for *in situ* experiments under irradiation of energetic particle, such as high voltage electron microscopy experiments [20] and Rutherford backscattering/channelling experiments [120,121], since those experimental techniques are applied in a single crystal or narrow region in single grain.

In this chapter, the threshold displacement energies (E_d) in ZrN are evaluated using *ab-initio* MD (AIMD) simulation. Investigation on different directions of PKAs for both Zr and N atoms, which covers the mostly whole regions of the stereographic triangle, provides anisotropic information of displacement damage process and the average values of E_d in ZrN.

4.2 Computational methods

The AIMD simulations were performed with a modified version of the SIESTA code [71,93]in the framework of density functional theory (DFT). Figure 4.1 shows the fundamental steps taken in configuring an AIMD simulation in SIESTA. The first step is to take an initial system configuration and find the ground state of the structure of interest. This usually includes the SIESTA pseudopotential database to be used and lattice geometries to be researched. In

this study, the pseudopotentials contained in the SIESTA database were used [93]: the norm-conserving Troullier-Martins pseudopotentials [122] factorized in the Kleinman-Bylander form [123], which was described as interactions between atoms and electrons.

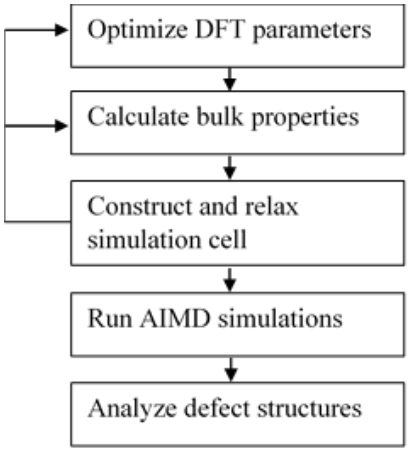

Figure 4.1 Illustrating the steps needed to configure an AIMD based Ed calculation. It may be required to go back and further optimize the stimulation parameters at any point in the figure.

The exchange-correlation functional was treated in the generalized gradient approximation (GGA), as parameterized by Perdew, Burke, and Ernzerhof (PBE) [124]. The reference valence electronic configurations $5s^2 4d^2$ and $2s^2\ 2p^3$ are used for Zr atom and N atom, respectively. The core radii of the pseudopotential for Zr atoms were 3.0 Bohr (5*s* electrons) and 2.68 Bohr (4*d* electrons), and the values for N atoms were 1.48 Bohr (2*s* electrons) and 1.48 Bohr (2*p* electrons). The minimum approach distance of PKAs with the largest energy in the simulation was larger than these radii.

The next is to completely relax the system to evaluate the ground state until the pseudopotential is correctly configured. This was achieved using the experimentally determined lattice constants and allowing the system to find the minimum energy. Then, along with modified DFT parameters, a necessary static DFT calculation was carried out on the relaxed structure (cutoff energy, K-point sampling in the Brillouin zone, and valence wave

function configurations). The convergence testing was performed to determine the suitable values of the cutoff energy and K-point mesh is shown in Figure 4.2(a) and (b). The cutoff energy 130 Ry (Rydberg) and a 4×4×4 K-point mesh supercell were simulations in this study. The valence wave functions were extended in the basis set of localized atomic orbitals, and double –ζ basis sets were used.

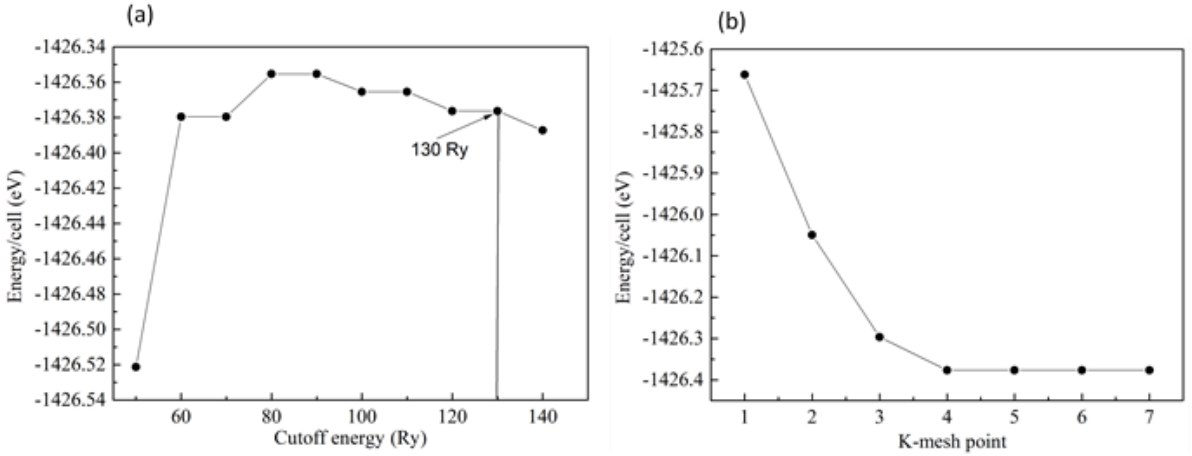

Figure 4.2 (a) The convergence testing plot for cut-off energy and (b) plot for K-mesh point for our simulation.

4.3 Bulk material properties

4.3.1 Lattice constant and bulk modulus

Once the initial system configuration is chosen and relaxed, it is possible to calculate bulk material properties. The determinations of the lattice constant and bulk modulus by fitting to an equation of state were calculated relating to the bulk properties. The Birch-Murnaghan equation of state [125] was used in this study. The Murnaghan equation of state as expressed by equation (4.1), which was first proposed by Murnaghan in 1944 [125], is a relationship between the pressure *P*, volume *V*, and modulus of incompressibility K_0, K_0' is a constant of material under expression as

$$P(V) = \frac{K_0}{K_0'}\left[\left(\frac{V}{V_0}\right)^{-K_0'} - 1\right] \tag{4.1}$$

In connection to *ab initio* calculations, the equation of state can be integrated along with the relationship $P = \frac{-dE}{dV}$ to yield equation (4.2). This will be the primary form of the equation utilized, because it is a direct relationship between the volume, energy, and bulk modulus of a material,

$$E(V) = E_0 + K_0 V_0 \left[\frac{1}{K_0'(K_0'-1)}\left(\frac{V}{V_0}\right)^{1-K_0'}\right] + \left[\frac{1}{K_0'}\frac{V}{V_0} - \frac{1}{(K_0'-1)}\right] \tag{4.2}$$

Later, the following equation of state (eq. (4.3) was suggested by Birch and Murnaghan based on the work by Murnaghan as described above [125]. The Birch-Murnaghan equation of state was, like the equation developed by Murnaghan, based around cubic symmetry in crystals. This particular equation is the third-order isothermal equation of state for the strain components,

$$P(V) = \frac{3B_0}{2}\left[\left(\frac{V}{V_0}\right)^{\frac{7}{3}} - \left(\frac{V}{V_0}\right)^{\frac{5}{3}}\right]\left\{1 + \frac{3}{4}\left(B_0' - 4\right)\left[\left(\frac{V}{V_0}\right)^{\frac{2}{3}} - 1\right]\right\} \tag{4.3}$$

Applying the same procedure as before with the Murnaghan equation of state, and integrate by pressure yields eq^{n} ((4.4),

$$E(V) = E_0 + \frac{9V_0B_0}{16}\left\{\left[\left(\frac{V}{V_0}\right)^{\frac{2}{3}} - 1\right]^3 B_0' + \left[\left(\frac{V}{V_0}\right)^{\frac{2}{3}} - 1\right]^2\left[6 - 4\left(\frac{V}{V_0}\right)^{\frac{2}{3}}\right]\right\} \tag{4.4}$$

where P is the pressure, V_0 is the reference volume, V is the deformed volume, B_0 is the bulk modulus, and B_0' is the derivative of the bulk modulus with respect to pressure. Taking

the simulation cell volume from an initial relaxation, a range of volumes is selected around that value, and the energy is computed for each volume using a static calculation. The resulting energy-volume curve is then fitted to (equation (4.4) using a Nelder-Mead optimization algorithm to find the best fit. With these optimized lattice constants and a value of the bulk modulus produced by the fitting algorithm, it is then possible to verify that the computational configuration selected produces reasonable simulations compared to other DFT and experimental work. The computation set up is then used to construct simulation supercells for performing the E_d simulations.

4.4 AIMD

The NVE (number of particles, volume, energy) microcanonical ensemble was used in the simulations. A 3×3×3 unit cell of ZrN containing 216 atoms was used together with periodic boundary conditions (PBCs) while maintaining a constant particle number and volume. Displacement damage spike affected atoms within half of the 3×3×3 supercell of ZrN for most of our simulations, in which the displacement spike did not overlap over the PBC; previous investigations on the evaluation of E_d also used a 3×3×3 supercell [126]. The methods for determining threshold displacement energies is shown in Fig. 4.3. The system was equilibrated at 50 K using the NVE ensemble with a time step of 1.0 fs up to a total time of 1 ps. Then, the AIMD simulations for evaluating of E_d were performed at 50 K using the equilibrated system with a fixed time step of 1.0 fs, since no significant difference was observed for the traces of the PKA and final defect configurations between two time steps of 0.5 fs and 1 fs, for the simulation of Zr PKAs along the [110] direction with an energy of 22 eV. The travel distance of PKAs with the time step was approximately 0.08 Å, and it took 15 time steps to travel half of the Zr-N distance to the [100] direction.

There are several definitions on E_d [71,119,127,128], and this work has followed the definition given in Ref.[128], in which E_d was defined as the minimum kinetic energy to produce a permanent defect, or Frenkel pair, in the crystal.

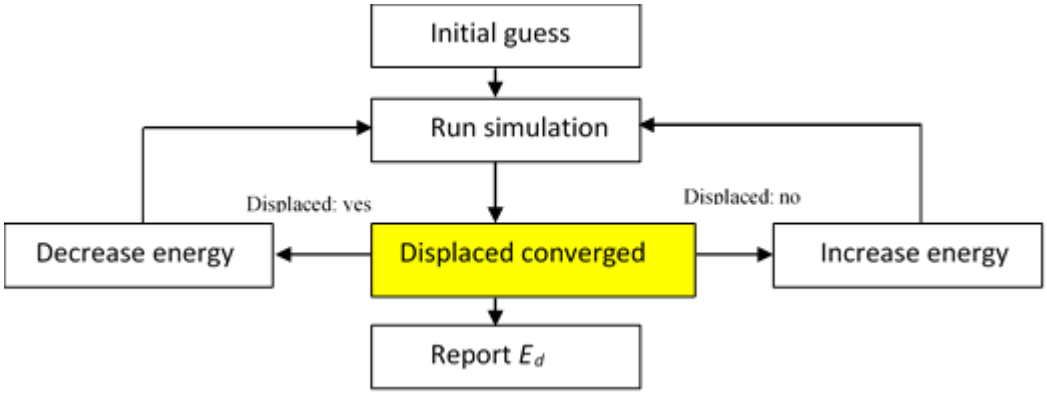

Figure 4.3 Methods for determining threshold displacement energies.

Evaluation of E_d was performed for seven crystallographic directions, which are <100>, <110>, <111>, <210>, <211>, <221>, and <321>, as those directions are shown in a unit cell of ZrN (Fig.4.4). These directions were also shown in a stereographic triangle, indicating that the simulated directions in this study cover most regions of the stereogram (Figure 4.5). Notably, the same type of atom as the PKA s located in the <110>, <211>, and <321> directions, whereas the opposite type of atom exists in the <100>, <111>, <210>, and <221> directions. Zr and N PKA simulations in the <110> direction were performed up to a total simulation time of 3 ps to monitor the stability of the Frenkel pairs is shown Figure 4.6. Frenkel defects were formed within 300 fs for both Zr and N PKAs, and no recombination of Frenkel defect was observed until 3 ps. For most PKAs investigated in this study, Frenkel defects were formed at approximately ≤ 300 fs and existed at the position until a simulation time of 600 fs. Therefore, the simulations were performed using a fixed time of 600 fs. Initially, the PKA energy was set to be 50 eV for all directions following the result in MgO [126]. If the initial PKA energy

displaced a lattice atom, the simulation process was repeated by reducing the energy by 10 eV. The values were then finely tuned to observe whether the PKA induces a Frenkel defect with a precision of 1 eV.

Figure 4.7 is shown with and without displacement events along the <100> direction for Zr PKA atom with an energy E_{PKA} = 38 eV and 39 eV, respectively. Here, we represent all atom traces at the end of simulations. From Figure 4.7(a) Zr_{PKA} atom traces back to the original lattice site position at the end of simulation that means no displacement event occurred and was not formed any Frenkel defects. On the other hand Figure 4.7 (b) when increased the kinetic energy by 1 eV to 39 eV apply on Zr PKA atom the blue colour traces was not back to the original lattice site.

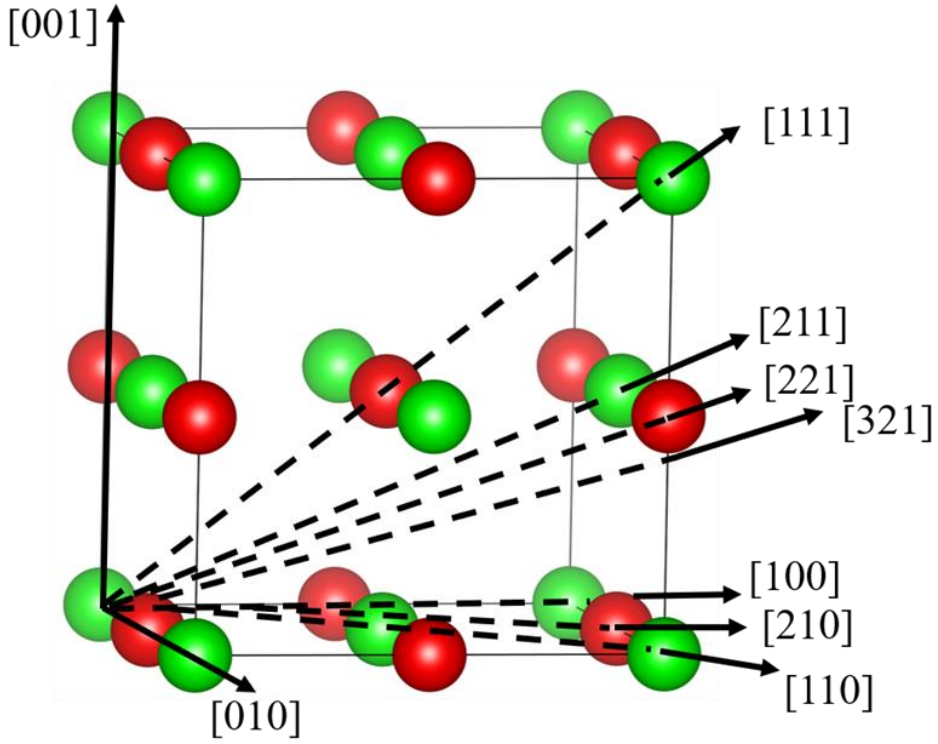

Figure 4.4 ZrN unit cell with crystallographic directions of [100], [110], [111], [210], [211], [221] and [321], which were investigated threshold displacement energies in this study. Red and green spheres represent N and Zr atoms, respectively.

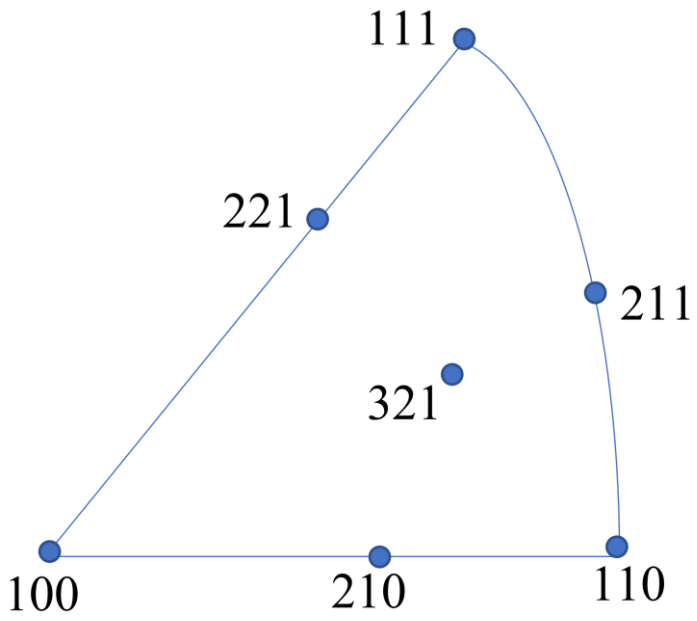

Figure 4.5 A stereogram of a cubic crustal structure showing lattice planes that were perpendicular to the PKA directions investigated in this study.

This mean displacement event was occurred to form a Frenkel defect. Sometimes PKA atom is still in motion at the end of the simulation that case simulation time must be increased and monitoring atoms movement. There are several more atoms in a real substance to transfer this energy so that it dissipates in the system. In small systems used in AIMD, this energy is retained inside the system because of restrictions on which types of thermostats can be used. The outcome cannot reflect real phenomena if too much energy is transferred to the system. If too much energy is allowed to dissipate to the rest of the atoms in the system, a displacement chain that requires a larger simulation cell will interfere with itself.

Results and discussion

4.4.1 Lattice constant and bulk modulus

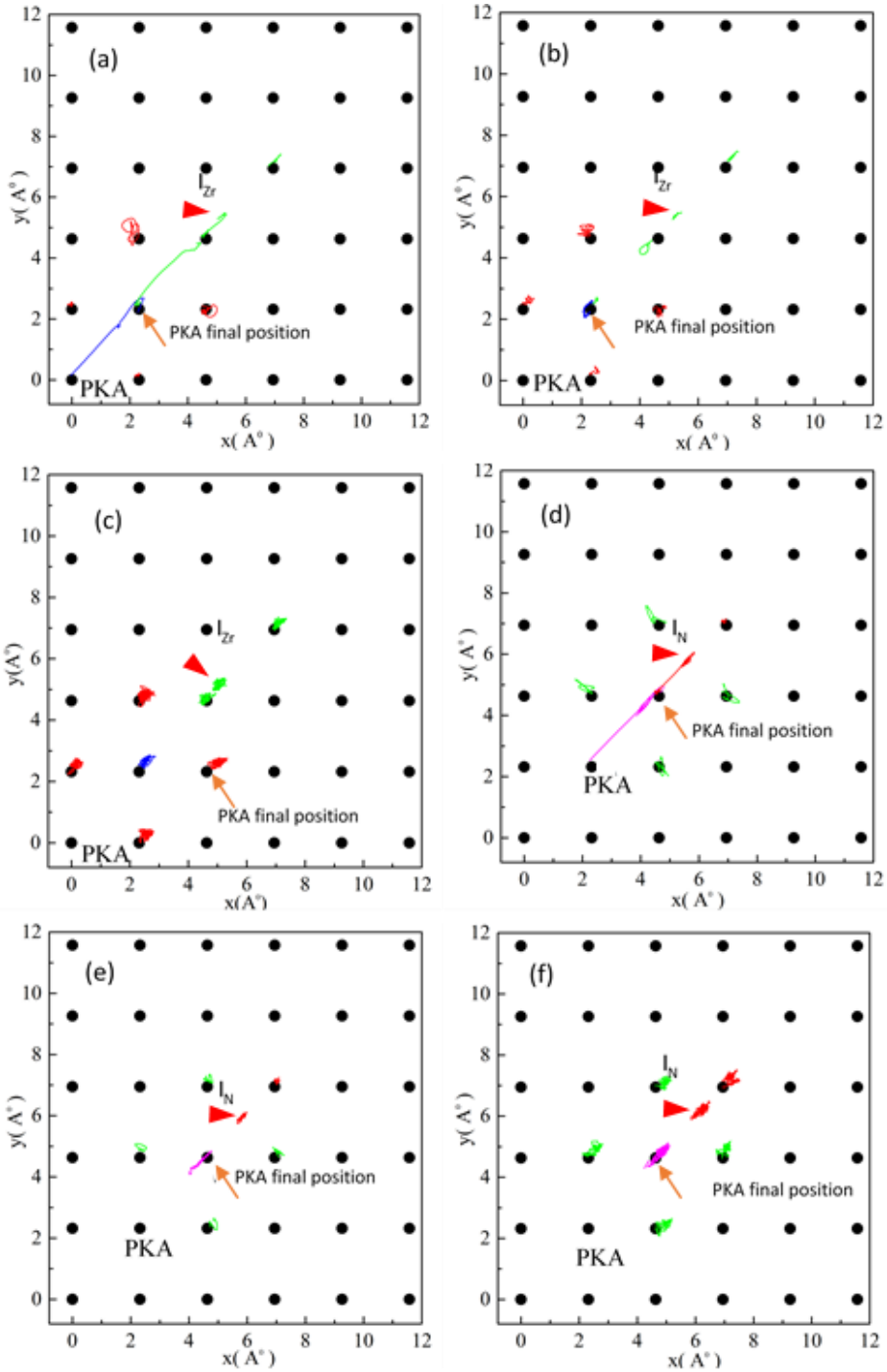

Figure 4.6 Traces of Zr and N PKAs and surrounding atoms with different observed time duration. (a)-(c): Zr PKAs with 22 eV in the [110] direction for (a) simulation time from 0-300 fs, (b) simulation time from 300-600 fs, and (c) simulation time from 600-3000 fs. (d)-(f) N PKAs with 16 eV in the <110> direction for (d) Simulation from 0-300 fs, (e) Simulation time from 300-600 fs, and (f) Simulation time from 600-3000 fs.

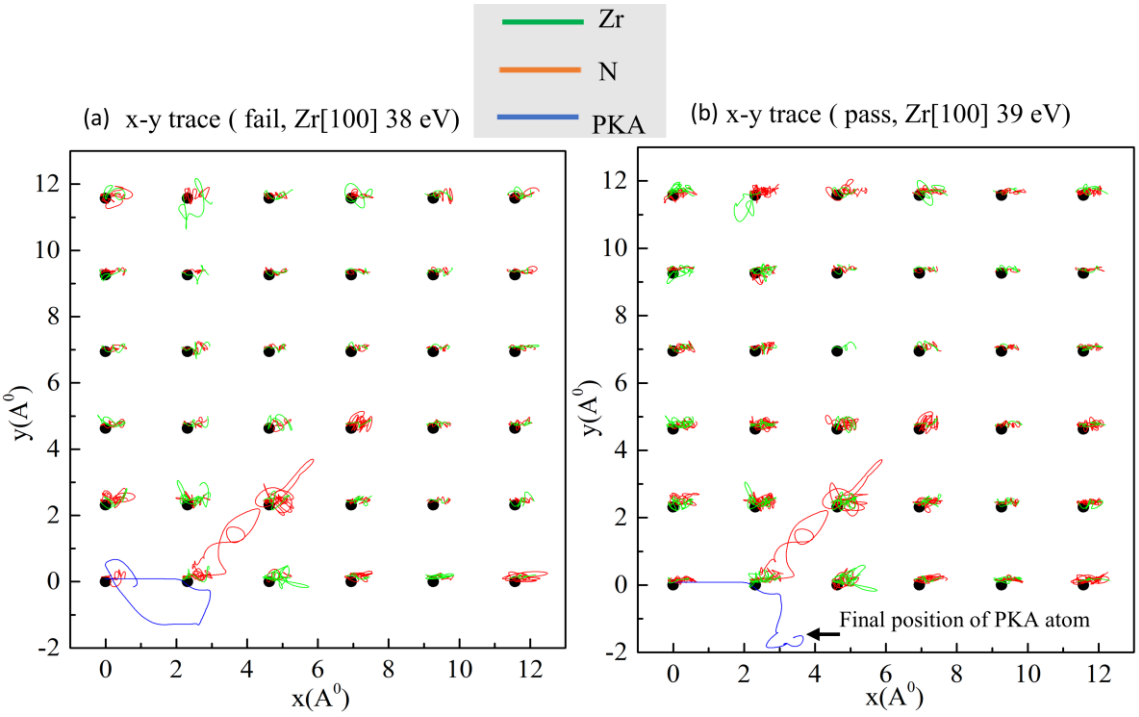

Figure 4.7 Traces of the x-y plane of a failure (left) and success (right) to produce a Frenkel pair. The difference in energy between the two is 1 eV.

Figure 4.8 depicts the variation in the energy of the system versus the volume of the unit cell. The data were fitted to the 4th-order Birch-Murnaghan equation of state to predict an equilibrium lattice parameter and a bulk modulus at the minimum energy point of the *E-V* curve. The calculated lattice parameter of 4.61 Å exhibited good agreement with experimental values of 4.585 Å [129] and 4.61 Å [130]. The calculated bulk modulus of 273 GPa also correlated with experimental values 267 GPa [130] and with the value of 246 GPa obtained by DFT calculations [131,132].

The results for calculated E_d values of Zr and N atoms are summarized in Table 4.1and Figure 4.9. The displacement energy was determined by tuning the PKA energy whether or not the PKA atom induces a Frenkel defect in the crystal as mentioned below. The simulation had run a sufficient time where the displaced atoms remained in a stable configuration. Table 4.1

also summarizes the values of d_{PKA}, defined as the distance between the initial and the final position of the PKA, and the final defect state for each PKA.

As shown in Table 4.1 and Figure 4.9 that the values of E_d are dependent on the type of atoms and crystallographic directions, varying from 15 eV to 50 eV for a N PKA along the <210> and <111> directions, respectively, although the crystallographic dependence was not large, as observed in pure fcc metals, such as for Cu [133]. This might be due to the crystal structure and difference in mass between the constituent atoms. The detailed collision process for each PKA atom is described below. The average value of E_d for each atom was evaluated from E_d values of seven crystallographic directions of <100>, <110>, <111>, <210>, <211>, <221>, and <321>, which includes high symmetry low index directions but also non high symmetric ones.

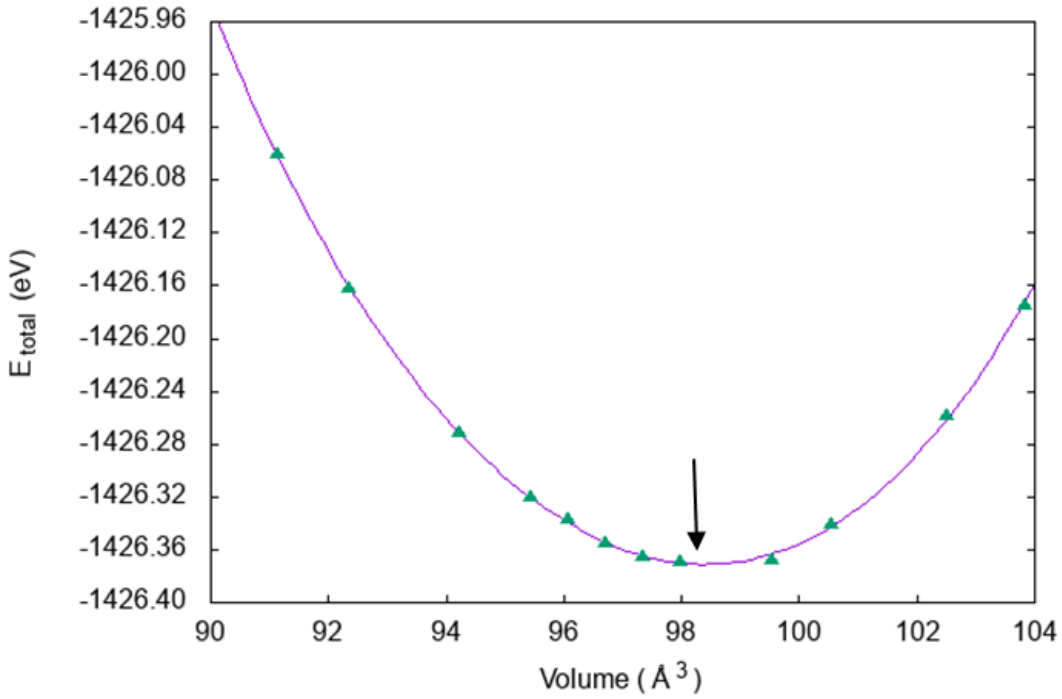

Figure 4.8 Energy of the ZrN unit cell versus volume. The curve is given by fitting to the Birch-Murnaghan equation of state. The arrow shows the point that represents the minimum volume calculated from the fit shown by the curve.

Table 4.1 Recoil direction, threshold displacement energy (E_d), the distance between initial and final position of the PKA (d_{PKA}), and the final defect state for each PKA are indicated.

PKA	Direction	E_d (eV)	d_{PKA} (Å)	Defect state
Zr	<100>	39	3.42	V_{Zr} + I_{Zr} with <111> split-type
Zr	<110>	22	2.4	V_{Zr} + Zr (PKA) $_{Zr}$+ Zr_{Zr}+ I_{Zr} with <111> split-type
Zr	<111>	31	3.15	V_{Zr}+ I_{Zr} with <111> split-type
Zr	<210>	45	4.64	V_{Zr}+ Zr (PKA) $_{Zr}$ + I_{Zr} with <111> split-type
Zr	<211>	25	3.27	V_{Zr}+ I_{Zr} with <111> split-type
Zr	<221>	35	1.76	V_{Zr}+ I_{Zr} with <111> split-type
Zr	<321>	31	4.45	V_{Zr}+ Zr (PKA) $_{Zr}$ + I_{Zr} with <111> split-type
	Zr sublattice weighted average			33 eV
N	<100>	39	2.26	V_N + N $(PKA)_N$ + I_N at tetrahedral interstitial site
N	<110>	16	3.90	V_N + N $(PKA)_N$ + I_N at tetrahedral interstitial site
N	<111>	50	1.87	V_N + N $(PKA)_N$ + I_N at tetrahedral interstitial site
N	<210>	15	3.68	V_N + I_N at tetrahedral interstitial site
N	<211>	35	1.44	V_N + I_N at tetrahedral interstitial site
N	<221>	25	2.43	V_N + N $(PKA)_N$+ N_N+ I_N at tetrahedral interstitial site
N	<321>	35	4.72	V_N + N$(PKA)_N$+N_N+N_N+N_N+ I_N at tetrahedral interstitial site
	N sublattice weighted average			29 eV

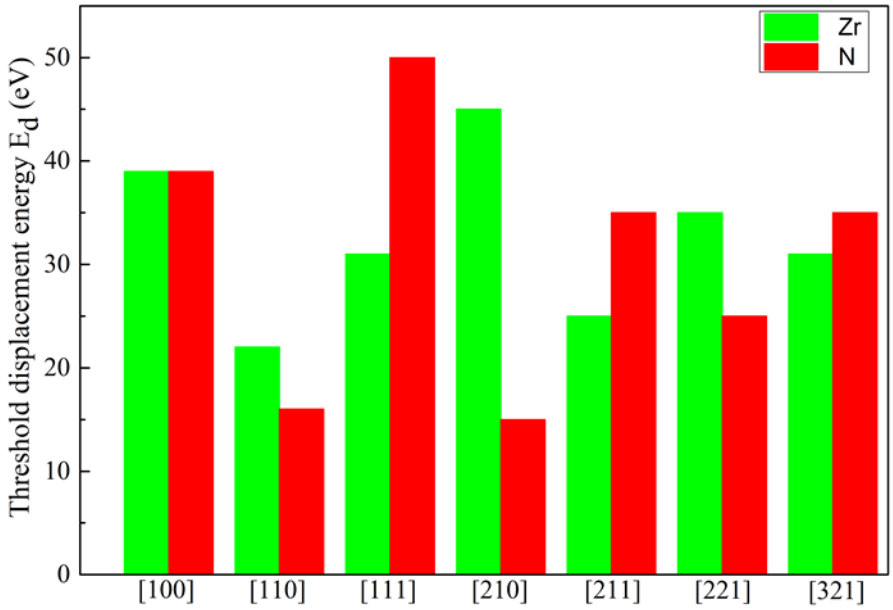

Figure 4.9 Comparison of Ed for the seven crystallographic directions in ZrN. Green and red bars represent Ed values of Zr and N atoms, respectively.

The weighted factor of each direction from the crystallographic symmetry of the rock-salt structure [117] was taken into consideration for obtaining the average values. Hence, the average values of E_d in ZrN were evaluated to be 33 eV and 29 eV for the Zr atom and N atoms, respectively, indicating a slightly higher value for Zr atoms. The evaluated E_d exhibited similar values and similar tendency between two types of atoms to those of other compounds with rock-salt structure: Ta (42±2 eV) and C (28±6 eV) of TaC obtained from electrical resistivity measurements [18], and Zr (37±1 eV) and C (16 ±1 eV) of ZrC from an initio MD simulation [117]. The small E_d value of the C atom in ZrC is discussed caused by the significantly lower value of E_d for the PKA along the <111> direction, which is attributed to atomic bonding between C atoms and the PKA during collision process [117].

Notably, the generation of PKA at 50 K is a stochastic process is shown in Figure 4.10. Atomic collision processes and traces of PKAs were significantly dependent on the type of

PKAs and crystallographic directions. Figure 4.11 depicts the traces of PKAs and a part of surrounding ions (a-c); the final configurations of the ions (d-f) of Zr PKAs initiated to low-index directions of [100], [110] and [111]. The Zr PKAs in the [100] direction (denoted as A in Figure 4.11 (a) collided with the nearest neighbor N atom (denoted as B in Figure 4.11 (a) and moved to an interstitial position labelled E. The recoiled N atom at position B received sufficient kinetic energy to interact with another N atom in the [110] direction at position C. The N atoms at B and C moved along the [110] direction and finally returned to each original lattice site. Accordingly, a Frenkel pair consisting of a Zr vacancy and a Zr interstitial was formed. The threshold displacement energy was determined to be 39 eV. The configuration of the Zr Frenkel pair is shown in Figure 4.11 (d) as a view of the atomic rows from the nearly [100] direction. The interstitial was observed as a split type along the <111> direction. Most of the interstitials exhibited <111> split-type configurations, as shown by the Zr PKAs generated in other directions. This is consistent with the DFT simulation results for metal nitrides with rock-salt structures, in which interstitials revealed a minimum energy split type along the <111> directions in ZrN [134].

To understand the effects of the uncertainties of the PKA generation, the traces of PKA and surrounding atoms were monitored under different initial conditions of PKAs with the same direction and energy. Simulations of the Zr PKAs with 39 E_d in the [100] directions were, therefore, performed for 11 different initial conditions obtained by changing the equilibration time of the supercell. The traces were confirmed to be qualitatively the same, and a Frenkel defect was formed for all conditions resulting the <111> split-type interstitial configurations. Similarly, simulations of N PKAs in the [110] directions under different initial conditions were confirmed to show qualitatively the same trace of PKAs and surrounding atoms. The

directional uncertainties at 50 K did not influence the determination of E_d and qualitative traces of PKAs, but influenced the final position of an interstitial atom. Furthermore, no anti-site defects were observed for Zr PKA in the [100] direction. Such anti-site defects were not formed for the Zr and N PKAs in all directions investigated in this study, as will be described below. Therefore, only formation of Frenkel defects was monitored within the simulation time of 600 fs.

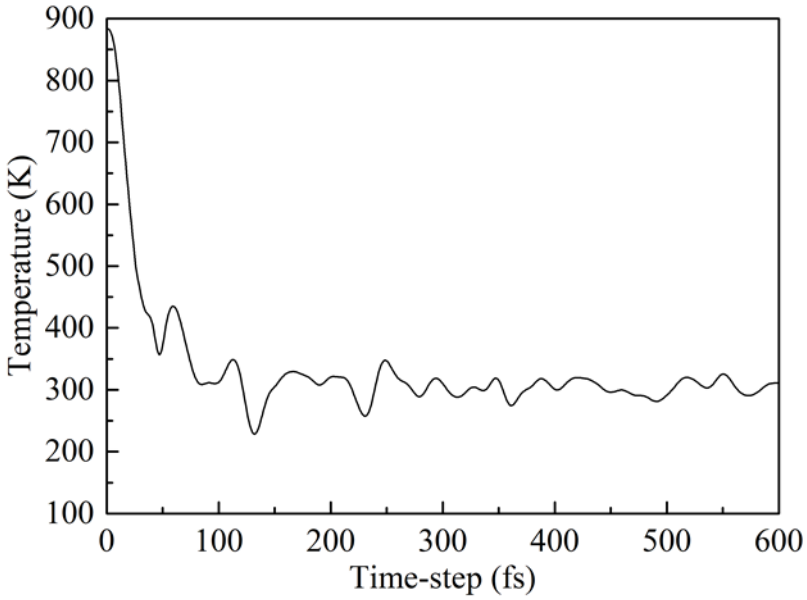

Figure 4.10 To show the generation of PKA is a stochastic process along [110] direction.

A Zr PKA directed to the [110] direction has shown to induce a sequential replacement collision within the [110] atomic row, as shown in Figure 4.11(b). The Zr PKA (denoted as A in Figure 4.11(b)) induced the replacement collisions with other Zr atoms, resulting the formation of a Zr vacancy at A and an interstitial Zr atom at D with a threshold PKA energy of 22 eV. The values of E_d in the [110] PKA direction were significantly lower than those in the [100] and [111] directions. The interstitial Zr atom revealed a split-type interstitial along the [111] direction as shown in Figure 4.11(e), which is one of the stable configuration of an interstitial atom in ZrN [135].

The displacement process of Zr PKA in the [111] direction is rather complicated, involving a rebounding event. As shown in Figure 4.11(c), the Zr PKA (denoted as A in Figure 4.11(c)) first collided with the neighbouring N atom along the [111] direction at position B, then the N atom was rebounded from an N atom at the next neighbour to the [110] direction. The Zr PKA resided temporarily on the vacant N ion site (B in Figure 4.11(c)), and was replaced by the rebounded N atom, resulting in Zr PKA being an interstitial atom of a <111> split-type at position D, which is also described in Figure 4.11(f)). The threshold Zr PKA energy in the direction of [111] was 31 eV. It is noted that no anti-site defects were formed for Zr PKAs for the three low index directions. Such anti-site defects were not formed for all directions of both Zr and N PKAs as described in later.

The recoil processes of N PKAs differed from those of Zr PKAs. Figure 4.12 shows the traces of PKAs and surrounding atoms together with the final configurations of atoms at the simulation time of 600 fs for N PKAs in the [100], [110], and [111] directions. In the case of the [100] simulation, the N PKA (denoted as A in Figure 4.12(a)) was rebounded from the nearest neighbor Zr atom along the [100] direction (denoted as B) and rebounded again with Zr atoms in the opposite [$\bar{1}$00] direction (denoted as C). Finally, the N PKA was moved to position E and replaced with the N atom at position E to induce an interstitial atom at the position F. Other collided Zr and N atoms returned to their original lattice sites within the simulation time. The threshold energy was determined to be 39 eV for this case. Interestingly, N interstitials were observed at the tetrahedral sites (Figure 4.12(a-c)), which is consistent with a report by DFT simulations in ZrN [134]. The preferable sites of the interstitials were clearly different for the Zr and N atoms.

The N PKA in the [110] direction exhibited a replacement collision with the neighbor N atom (denoted as B in Figure 4.12(b)), as observed in the Zr [110] PKA. The replaced N atom recoiled again with the next neighbor N atom and became an interstitial atom at position C with a threshold energy of 16 eV. The configuration of the defects is shown in Figure 4.12(e), revealing the formation of an N interstitial at the tetrahedral site and a vacancy.

The value of E_d in this direction was lower than those in the [100] and [111] directions, as observed for Zr PKA in the [110] direction. The N PKA initially directed along the [111] direction showed a complex defect process (Figure 4.12(c)), similar to the Zr PKA to the [111] direction. The N PKA (denoted as A) rebounded from the nearest neighbor Zr atom (denoted as B) along the [111] direction and moved to the $[\bar{1}\bar{1}\bar{1}]$ direction to collide with a Zr atom at the opposite side (denoted as D). The Zr atom at the position B received sufficient kinetic energy to push another Zr atom located in the [110] direction (described as C, located at the same (100) plane with the position B). Both Zr atoms finally returned to the original lattice sites within the simulation time. The N PKA moved along the [010] direction to the lattice site E and became an interstitial atom at F. Finally, an N interstitial was induced at the tetrahedral position together with a N vacancy at position A.

E_d was also evaluated in other directions, such as [210], [211], [221], and [321] for both Zr and N PKAs. The displacement processes for those directions were different or partly similar to those observed for low-index directions of [100], [110] and [111]. Some examples for these PKAs are shown in Figure 4.13 and Figure 4.14, and these will be described by comparing the results obtained in the low-index directions. The Zr displacement event initiated along the [210] direction is shown in Figure 4.13 (a) and (c). The Zr PKA collides with an N atom at the nearest

neighbor to the [100] direction and a Zr atom in the [110] direction (position B). After colliding with the Zr atom, the PKA interacted with an N atom at C, then was replaced with a Zr atom at the position D, resulting in the formation of a split-type Zr interstitial along <111> direction (described as E in Figure 4.13(a) and (c)). The Zr PKA directed along the [321] direction showed a displacement process similar to that of the Zr [210] event. The PKA recoiled the nearest neighbor N atom along the [100] direction, then interacted with Zr and N atoms at the position B. PKA interacts with Zr and N atoms in a (001) column at the position C, and ultimately becomes a split-type Zr interstitial in the <111> direction at position D.

The N PKA initiated in the [210] direction collided with an N atom located in the [110] direction (described as C in Figure 4.14(a)) and became an interstitial at a tetrahedral site (position D). The threshold energy in this direction exhibited the lowest value of 15 eV, similar to the N PKA in the [110] direction. Conversely, the [210] N PKA did not induce replacement collisions, as observed in the [110] PKA, presumably due to the deviation from the critical incident angle to induce the focusing collision. The N PKAs directed to [221] and [321] involves replacement collisions of N atoms along the [110] direction. An example of these N PKAs is shown in Figure 4.14(b) and (d) to the N [321] simulation. The PKA was deflected from a Zr atom at the nearest neighbor to the [100] direction and collided with an N atom at the position B with a shallow angle to the [110] direction to induce sequential replacement collisions up to the fourth nearest neighbor, ultimately forming an interstitial N atom at the position F.

Interestingly, within the recoil processes of [221] and [321] simulations, all collision events were occurred on the (100) plane, where the PKA atoms were initiated. The threshold energies were 25 eV and 35 eV for the [221] and [321] directions, respectively, and these values

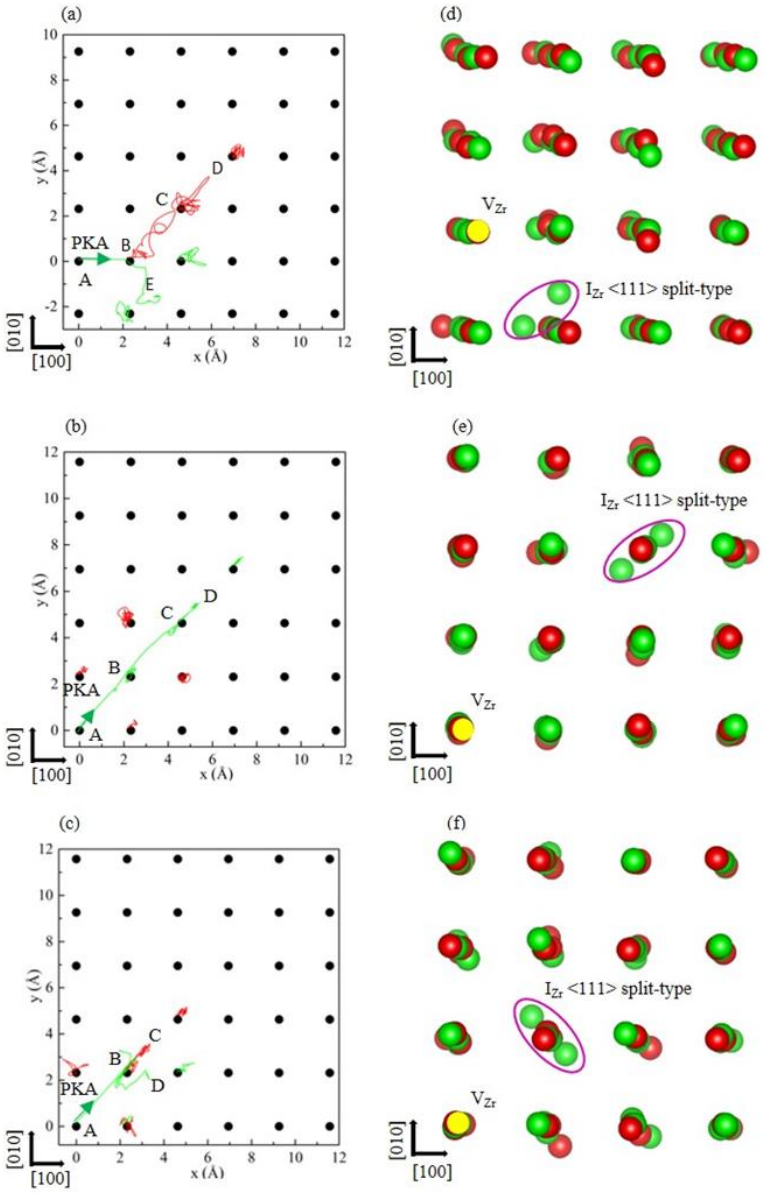

Figure 4.11 Traces of Zr PKAs in ZrN to initial directions of (a) [100], (b) [110] and (c) [111] projected on a (100) plane, represented as x [100] and y [010] axes. Black circles denote the position of the [001] atonic rows for the original lattice of ZrN, and the green and red lines describe the traces of Zr and N atoms, respectively, during the simulation of displacement process. Atomic configurations at the final simulation step are also shown from a view of nearly [001] direction, which is slightly inclined from the [001] direction for the easier view of atoms, for the PKAs directed to (d) [100], (e) [110] and (f) [111]. V_{Zr} and I_{Zr} are the vacancy and interstitial formed by the PKA, and the position of VZ is the one where PKA was initiated. The given PKA energies are 39 eV for (a) and (d), 22 eV for (b) and (e), and 31 eV for (c) and (f). The simulation time was 600 fs.

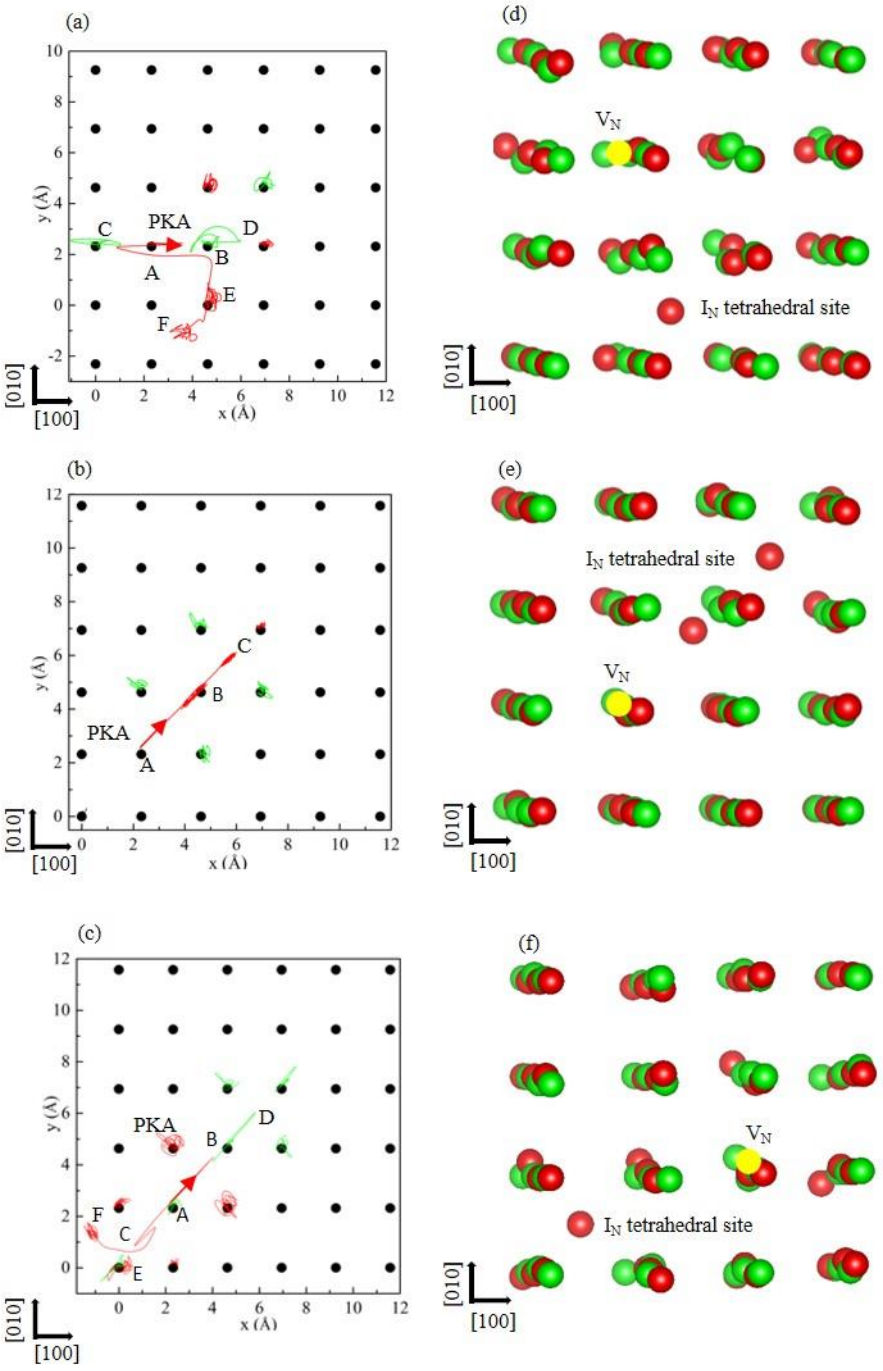

Figure 4.12 Same as Figure 4.10, but for N PKAs. Traces of N PKAs and surrounding atoms are shown for initial PKA directions of (a) [100], (b) [110] and (c) [111]. The corresponding atomic configurations at the final simulation step (600 fs) are also shown for PKAs directed to (d) [100], (e) [110] and (f) [111]. The given PKA energies are 39 eV for (a) and (d), 16 eV for (b) and (e), and 50 eV for (c) and (f).

were larger than the E_d value of the [110] PKA (16 eV). This is probably due to the slight deviation from the critical angle of the focusing collisions to the [110] atomic row. The N PKAs below the E_d values of the [221] and [321] directions were hardly induced sequential replacement collisions and atoms were finally returned to the original lattice sites without forming a Frenkel defect. The lower energy or velocity of the N PKAs below the threshold energy caused larger incident angles to the N atom at the position B to prevent the formation of sequential collisions.

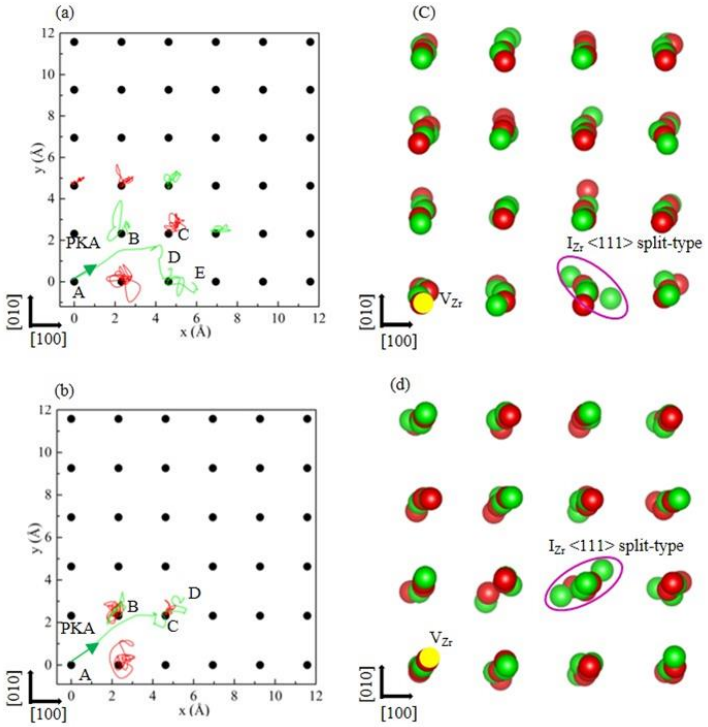

Figure 4.13 Traces of Zr PKAs initiated to (a) [210] and (c) [321] directions and surrounding atoms, projected on a (100) plane represented as x-y plane. Black circles denote the position of the [001] atonic rows for the original lattice of ZrN, and the green and red lines describe the traces of Zr and N ions, respectively. Atomic configurations at the final simulation step are also shown from a view of nearly [001] direction, which is slightly inclined from the [001] direction for the easier view of atoms for Zr PKAs to the direction of (c) [210] and (d) [321]. V_{Zr} and I_{Zr} are the vacancy and interstitial formed by the PKA, and the position of V_Z is the one where PKA was initiated. The given PKA energies are 45 eV for (a) and (c), and 22 eV for (b) and (d), respectively. The total simulation time was 600 fs.

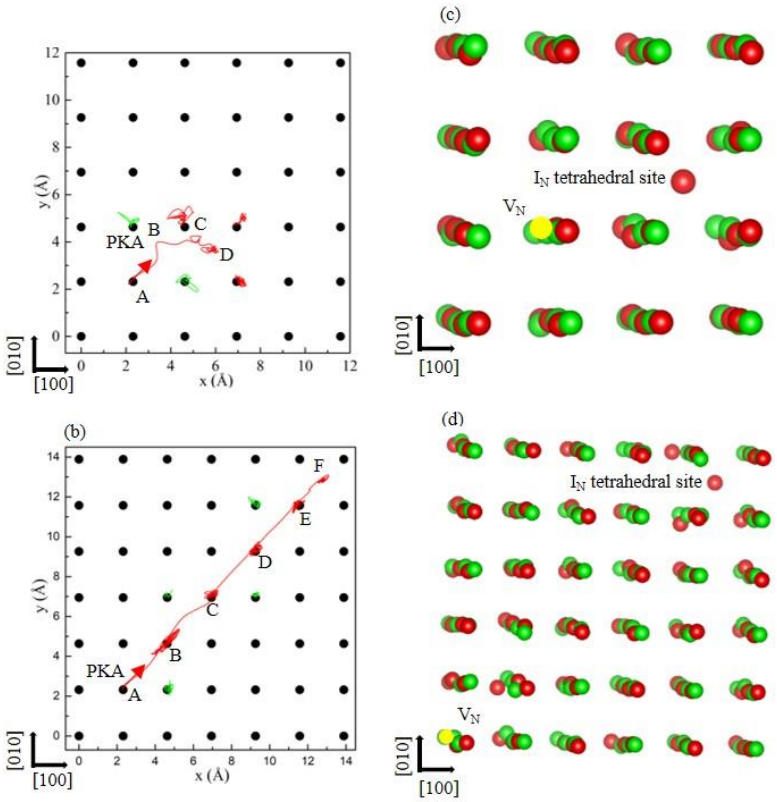

Figure 4.14 Same as Fig. 4.12, but for N PKAs initiated to the direction of (a) [210] and (c) [321]. Atomic configurations at the final simulation step are also shown from a view of nearly [001] direction for (c) [210] and (d) [221]. The given PKA energies are 15 eV for (a) and (c), and 35 eV for (b) and (d), respectively.

Figure 4.15 summarizes the number of observed events, or the number of induced interstitial atoms and replacement collisions per PKA, as a function of the E_d values. As described above, no anti-site defects were formed in ZrN for both Zr and N PKAs. This is a clear difference from others compounds, such as SiC [119,136], and spinel and pyrochlores with ionic bonding compounds consist of multiple cations [133,137]. Figure 4.9 reveals that lower values of E_d were observed in PKAs initiated in the [110] direction or those associated with the replacement collisions to the [110] atomic row. Similarly, the minimum values of E_d were observed in ZrC in the [110] direction, although an exception was observed for C PKA to the <111> direction [117]. In fluorite structure oxides, such as ThO_2, CeO_2 and ZrO_2, the

minimum value of E_d was observed in the [110] and [100] directions for cations and oxygen, respectively [64]. These results suggest that the crystallographic direction that yielded the minimum value of E_d was dependent on the crystal structures and types of atoms. However, notably, the minimum E_d was observed in the directions where the same kind of atoms were arranged in rows with a relatively smaller interatomic distance. This suggested that efficient energy transfer within the same types of atoms was an important factor for the displacement process in nitrides and oxides, which contain multiple sublattices with largely different masses. Another important factor was difference in the preferable configurations of interstitials between Zr and N atoms, because Zr interstitials existed preferably as a <111> split-type configuration, whereas N interstitials occupied tetrahedral sites is shown in Figure 4.16(a) and (b). This difference resulted in a significant variation in the displacement energy in the [210] direction. In particular, a Zr PKA was required to travel a longer distance to be a split-type <111> configuration as compared to N PKA, which is an interstitial at the nearest tetrahedral site.

The significant difference in E_d among the crystallographic directions also provided an important information for experiments using single crystal and nano-or micro-scale region, such as TEM and Rutherford backscattering/channelling experiments, because the estimated values of dpa might differ from the directions, and the oxides and nitrides might induce selective displacement damage or displacement damage with largely different displacement damage rates between cations and anions [20,22,62,112].

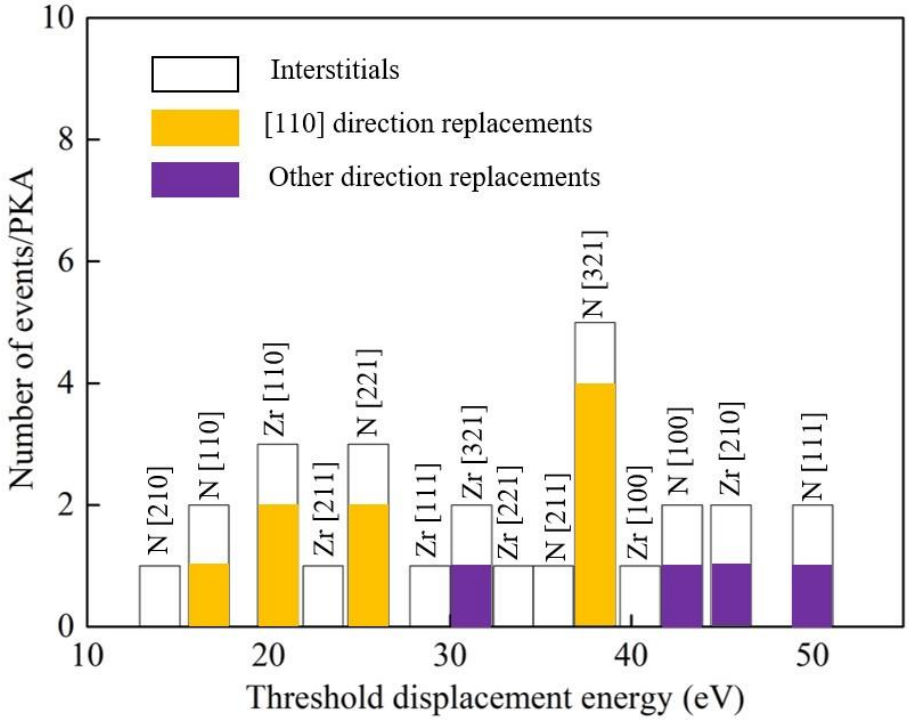

Figure 4.15 Number of replacements events and interstitial atoms observed for each PKA of different directions plotted as a function of threshold displacement energy.

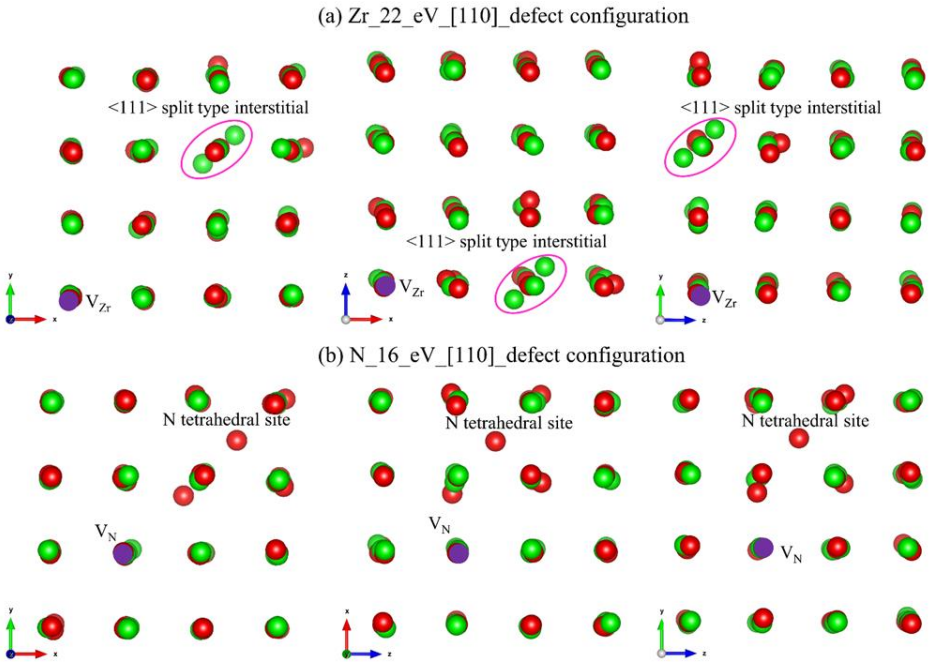

Figure 4.16 Typical examples of interstitial configurations. (a) showing a Zr intestinal <111> split-type and (b) N interstitial existing at a tetrahedral site.

4.5 Conclusions

AIMD simulations were performed to evaluate the threshold displacement energies (E_d) in ZrN along with seven different crystallographic directions. The weighted values of E_d were determined to be 33 eV and 29 eV for Zr and N atoms, respectively, exhibiting slightly larger values for Zr atoms. The values of E_d for both Zr and N atoms were dependent on the crystallographic directions, which ranged from 15 eV to 50 eV. Detailed monitoring of the traces of PKAs revealed that sequential replacement collisions to the [110] atomic row play an important role in the collision process, resulting in the lower values of E_d for both Zr and N atoms. Replacement collisions were also observed for PKAs deviating from [110] directions, such as N PKAs in the [221] and [321] directions, for which collisions occurred on the (100) plane where the PKA was initiated, resulting in sequential replacement collisions that satisfy the focusing condition. The results suggest that the efficient energy transfer to the directions where the same kind of atoms form a line is an important factor for the displacement process in ZrN containing two types of atoms with largely different mass. Furthermore, there are obvious differences in the preferable interstitial configurations: the <111> split-type configuration is preferable for Zr interstitials and N interstitials occupy the tetrahedral sites, which also influence the difference in the values of E_d.

Chapter 5

In-situ observation of radiation-induced defects in ZrN under electron irradiation in HVEM

5.1 Introduction

Zirconium nitride (ZrN) is a compound with the NaCl type crystal structure, described as Fm-3m in Wycoff notation, and has a superior feature that can accommodate plutonium and minor actinides up to (20-40)% in atomic fraction to form a solid solution [138,139]. This chapter deals with the nucleation-and-growth process of defect clusters in ZrN under electron irradiation using a high voltage electron microscope (HVEM). As described in Chapter 4, the threshold displacement energy (E_d) is an important parameter for the radiation damage process. The simulation study in Chapter 4 revealed that E_d are dependent on the crystallographic direction to range from 15 eV to 50 eV for N atoms and 22 eV to 45 eV for Zr atoms, respectively. The weighted average values of E_d in ZrN were evaluated to be 33 eV and 29 eV for Zr and N atoms, respectively, from the several crystallographic directions investigated, indicating a slightly higher value for Zr atom than N atom. High-energy electron irradiation using HVEM is a powerful tool for the fundamental investigation of radiation damage in materials, which allows one dynamical observation of the nucleation-and-growth-process of defect clusters under the production of isolated Frenkel defects [19,140,141]. It is also noted in ceramic compounds that values of E_d can be different on each sublattice (or be different from cations and anions), and this causes unbalance of the production rate of point defects between

the two sublattices. Previous investigations showed the formation of non-stoichiometric dislocation loops in fluorite-type compounds, such as ceria (CeO_2) [20,21] and yttria-stabilized cubic zirconia ($Y:ZrO_2$) [22], consists of solely with oxygen ions. However, at the present moment, there is very much limited information on the production and kinetics of point defects in ZrN, such as for the migration energy of point defects and the nature of defect clusters.

It is important to emphasize again that the mass number is significantly different between Zr and N atoms. The transferred energy from energetic particles, therefore, can be largely different between these atoms Figure 5.1 shows the displacement cross-section of Zr and N ions in ZrN against electron energy under an assumption of the values of E_d of 22 eV for Zr and 16 eV for N based on the evaluation described in Chapter 4 for the direction of <110>. Our experimental conditions were slightly inclined about 2° to 3° angle from the actual crystallographic symmetry. For this reason, the displacement of both atoms due to electron irradiation energies little different compared to theoretical simulation result along <110> directions. Figure 5.1 shows that both Zr and N atoms are displaced with 1.25 MeV electron irradiation, whereas only N atoms are displaced with electrons approximately less than 0.8 MeV. The nucleation-and-growth process of defect clusters was investigated as functions of irradiation time, temperature, and energy to discuss the nature of defect clusters and the migration energy of point defects.

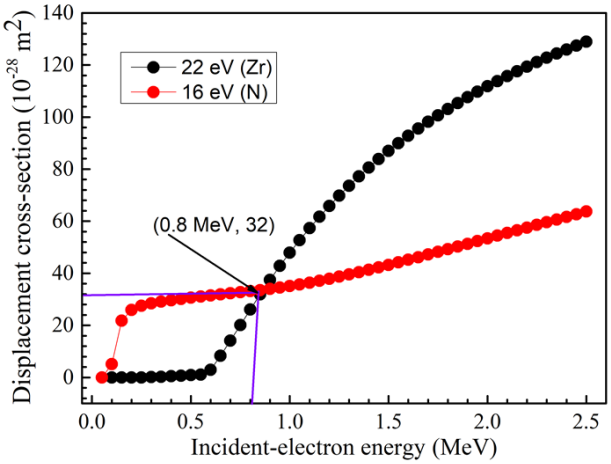

Figure 5.1 Simulation results of elastic displacement cross-section for Zr and N ions as a function of incident electron energy. Displacement cross-section is plotted with threshold displacement energies along the <110> direction 16 eV for N and 22 eV for Zr, respectively.

5.2 Materials and Experimental procedure

The sample preparation was elaborately described in Chapter 3. *In-situ* observations of the nucleation-and-growth process of radiation-induced defects were performed at different irradiation temperatures ranging from 873 K to 1273 K under electron irradiation with 1250 keV by using a high voltage electron microscope (JEM-1300NEF, JEOL Ltd.) at Ultra-microscopy Research Centre of Kyushu University, and different electron irradiation energies ranging from 400 keV to 1250 keV at constant temperature 973 K. The HVEM and a conventional TEM (HC-2100, JEOL Ltd.) were used for the microstructure observations. The electron irradiation and observation were performed using a focused electron beam with a size of around 1 μm in diameter, which is assumed to be close to a Gaussian distribution, under a constant electron beam flux of 4.4×10^{22} $m^{-2}\cdot s^{-1}$ at the centre position. The electron beam flux was measured with a Faraday cup inserted between a projection lens and fluorescence screen. The nucleation-and-growth process of defect clusters was recorded *in-situ* with a CCD camera (Gatan Orius SP450 HV) by using bright-field (BF) or weak-beam dark-field (WBDF) TEM

technique. TEM observations were performed for irradiated specimens with 1250 keV electrons using a conventional TEM and a high-resolution scanning TEM (STEM) with JEM-ARM 200CF (JEOL. Ltd,) at an accelerating voltage of 200 kV.

5.3 Defect clusters formed with 1250 keV electrons at different temperatures

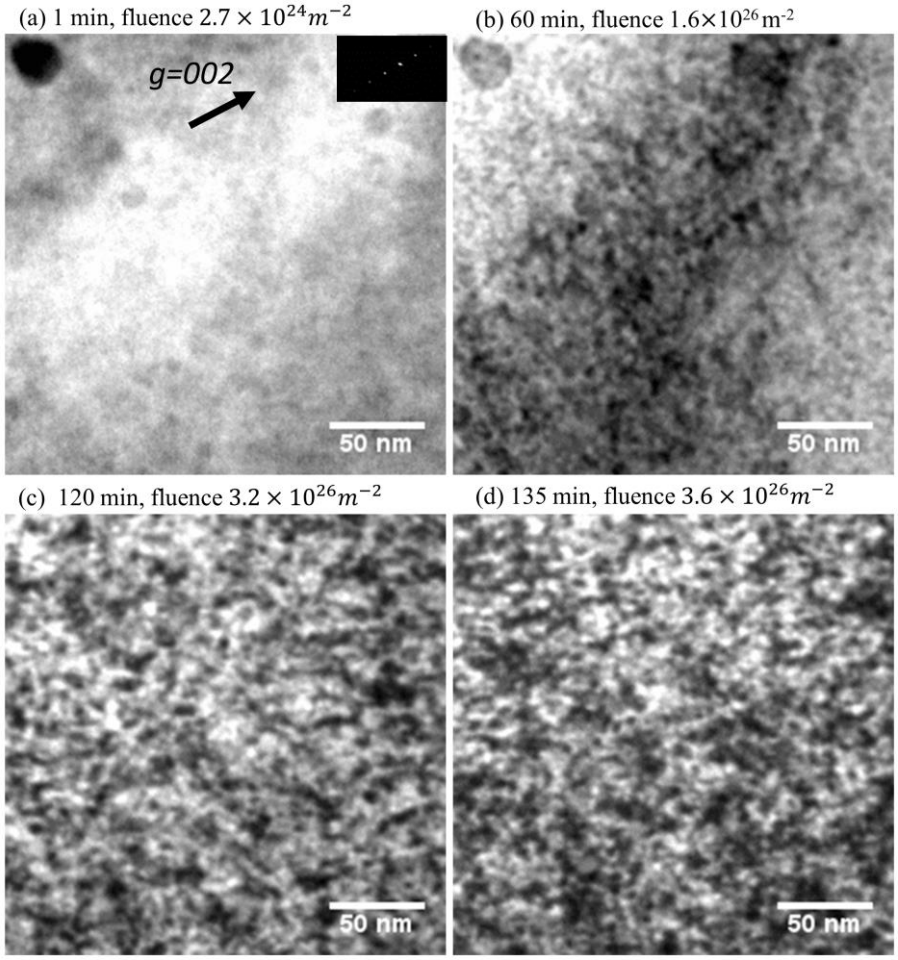

Figure 5.2 Bright field images of ZrN irradiated with 1250 keV electrons at 873 K in a HVEM with a flux of 4.4 $\times 10^{22}$ e m^{-2}s^{-1} for different irradiation time.

Figure 5.2 shows a sequential change of BF TEM images of ZrN irradiated at 873 K under irradiation with 1250 keV electrons. The images were taken with a systematic diffraction vector of $\boldsymbol{g}$ = 002 from the incident electron beam direction inclined around 3° from a <110>.

As shown in Chapter 4, values of E_d in the <110> direction are relatively low compared to other directions: values of E_d are 22 eV and 16 eV for Zr and N atoms, respectively, their by the electrons with 1250 keV are expected to induce displacement damage on both Zr and N atoms in the <110> direction (Figure 5.2). As shown in 5.2 (a) at the early stage of irradiation, no contrast of defect clusters was observed. Tiny dot contrast with around 2-3 nm in size appeared after an incubation time of around 20 min. The defect clusters were observed to increase the density and size with irradiation fluence to cover the whole irradiated region at a high fluence (Figure 5.2 (b)-(d)). At the higher temperature of 973 K, the tiny dot-contrast was observed also at the irradiation time at 20 min shown in Figure 5.3 (a).

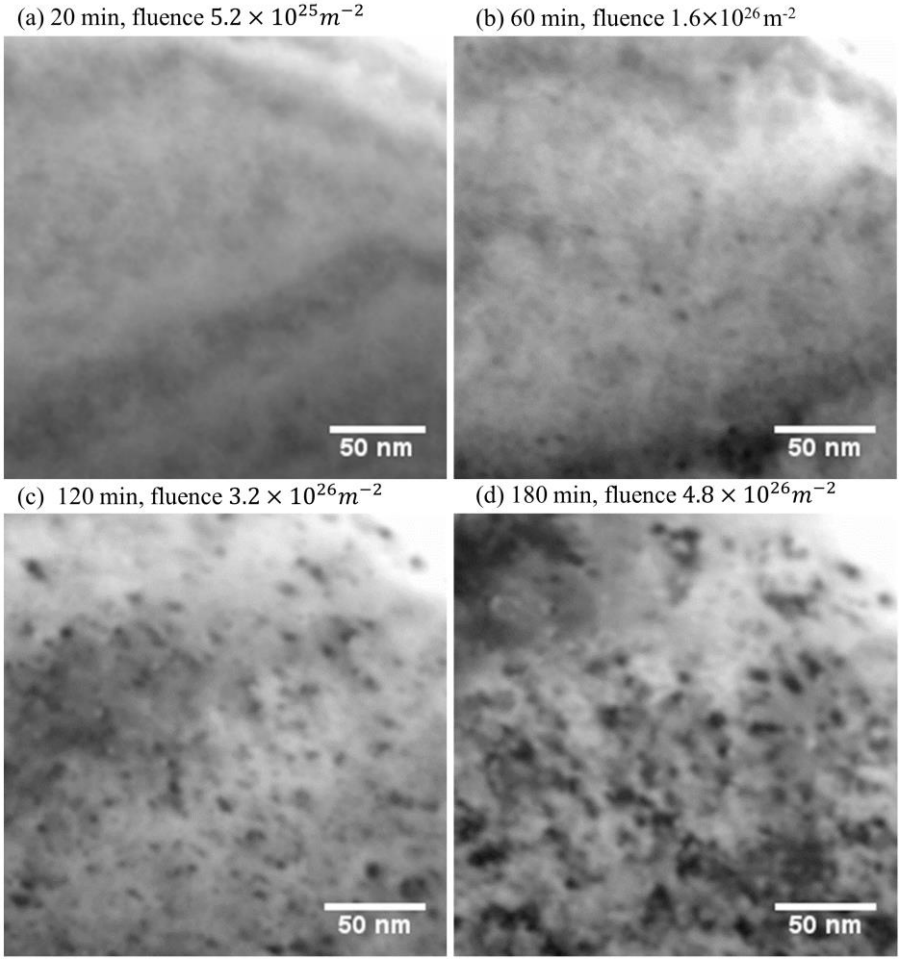

Figure 5.3 Bright field images of ZrN irradiated with 1250 keV electrons at 973 K in a HVEM with a flux of 4.4×10^{22} e m^{-2} s^{-1} for different irradiation time.

After 60 minutes electron irradiation, the defect were clearly observed with the increase of density. The defect clusters increased their size and the number density with irradiation time as shown in Figure 5.3 (c-d). The defect density became saturated at irradiation time of 120 min. The density of defect clusters and their size were lower and higher at 973 K than those at 873 K. At higher irradiation temperature of 1273 K a few tiny dot contrast was observed after 10 min of irradiation, as shown in Figure 5.4 (a). The defect clusters grew up gradually, as shown in Figure 5.4 (b)–(d).

5.3.1 g·b analysis of dislocation loops

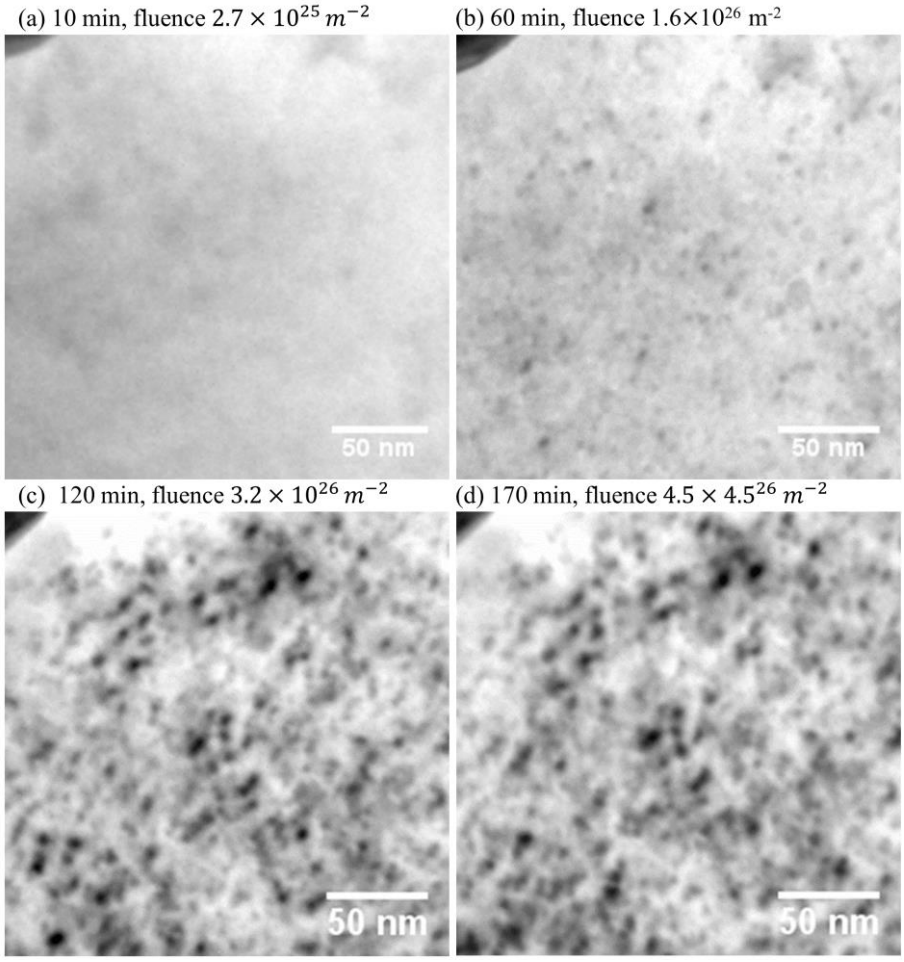

Figure 5.4 Bright field images of ZrN irradiated with 1250 keV electrons at 1273 K in a HVEM with a flux of 4.4 $\times 10^{22}$ e m^{-2} s^{-1} for different irradiation time.

The formation of dot contrast at higher temperatures as described in Section 5.3.1 is similar to the previous reports of ZrN irradiated with 2.6 MeV proton ions [9] and 300 keV Kr ions [9]. To understand the nature of the defect clusters formed under high energy electron irradiation, $\boldsymbol{g} \cdot \boldsymbol{b}$ analysis was performed to the defect clusters, where $\boldsymbol{g}$ is the diffraction vector for taking micrographs and $\boldsymbol{b}$ is Burgers vector. interstitials. shows examples of BF-TEM images of ZrN irradiated with 1250 keV electrons at 1173 K, taken with different diffraction vectors of $\boldsymbol{g} = 022, 002, 02\bar{2}, 020, 1\bar{1}1, 2\bar{2}0,$ and $\bar{1}11$. Defect clusters denoted as *A, B, C, D, E, F, G, H, I, and J* are seen in Figure 5.5 (a) as tiny dot contrast. Namely, all those defect clusters are visible at the diffraction condition of $\boldsymbol{g} = 022$. For another diffraction vector with $\boldsymbol{g} = 002$, all defect clusters are invisible except for *A* (Figure 5.5 (b)). Similarly, we show BF-TEM images with diffraction conditions with different $\boldsymbol{g}$ in interstitials. Figure 5.5 (c), (d), (e), (f), and (g). We performed the analysis on the visibility of 30 dislocation loops of dot contrast, based on the invisibility criterion $(\boldsymbol{g} \cdot \boldsymbol{b} = 0)$. 80% of the defect clusters was determined to have Burgers vector in parallel to *<110>* directions, and 20% of the contrast was not determined satisfactory. This is consistent with Burgers vector of dislocations in ZrN, or $\boldsymbol{b}$ = ½ <110> [142] determined by $\boldsymbol{g} \cdot \boldsymbol{b}$ analysis of TEM images formed by the quenching from a high temperature of 1200° C. Based on the results on the $\boldsymbol{g} \cdot \boldsymbol{b}$ analysis and the expected displacement damage condition for both Zr and N atoms, the nature of defect clusters formed in ZrN under 1250 keV electron irradiation is presumably the perfect-type dislocation loops with stoichiometric composition, suggesting both displaced Zr and N interstitials are included in the dislocation loops with keeping their charge neutrality.

The areal density of dislocation loops in ZrN was measured at regions of similar specimen thickness as a function of irradiation time, and the values are shown with logarithmic scale in Figure 5.6 for different irradiation temperatures of 873 K, 973 K, 1173 K and1273 K.

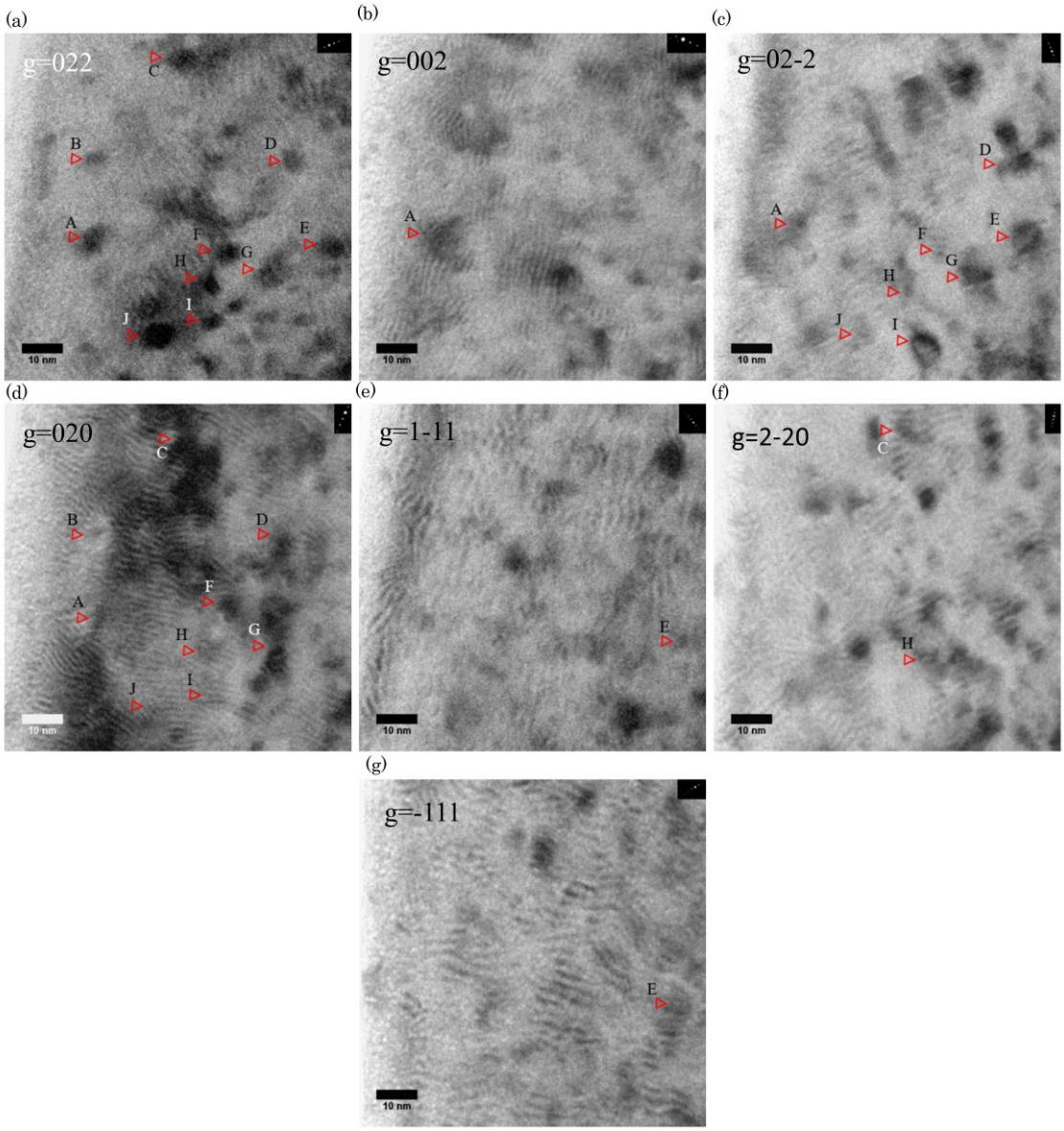

Figure 5.5 BF images of the defect clusters in ZrN irradiated with 1250 keV electrons at 1173 K with $\boldsymbol{g} = 022, 002, 02\bar{2}, 020, 1\bar{1}1, 2\bar{2}0, \bar{1}11$. The electron beam direction is nearly along the [100] and [110] direction for different g vectors.

At the early stage of irradiation, the density of the dislocation loops is seen to increase with a constant power index with an experimental error shown in Fig. 5.6 and evolves to saturation values at irradiation time or fluence longer than around 3000 sec or 1.3 $\times 10^{26}$ e m^{-2}. It is emphasized that the saturation of dislocation loops were achieved after long time irradiation.

This is clearly different from the density-time dependence of electron irradiated pure metals of Cu, Au, Mo, and Au [143] and Nb-Zr alloys [140], where the density of dislocation loops was saturated within the early stage of electron irradiation. Similarly, the density of dislocation loops showed a constant value, or the saturation in MgO at the begging of electron irradiation [141]. Those results reveals that the nucleation of loops is completed for materials whose nuclei of loops is di-interstitials, or a pair of anion and cation interstitials. The slope of the log-log plot, was evaluated by the least square methods to be 0.69 ± 0.02 (873 K), 0.67 ± 0.03 (973 K), 0.79 ± 0.04 (1173 K), and 0.72 ± 0.03 (1273 K).

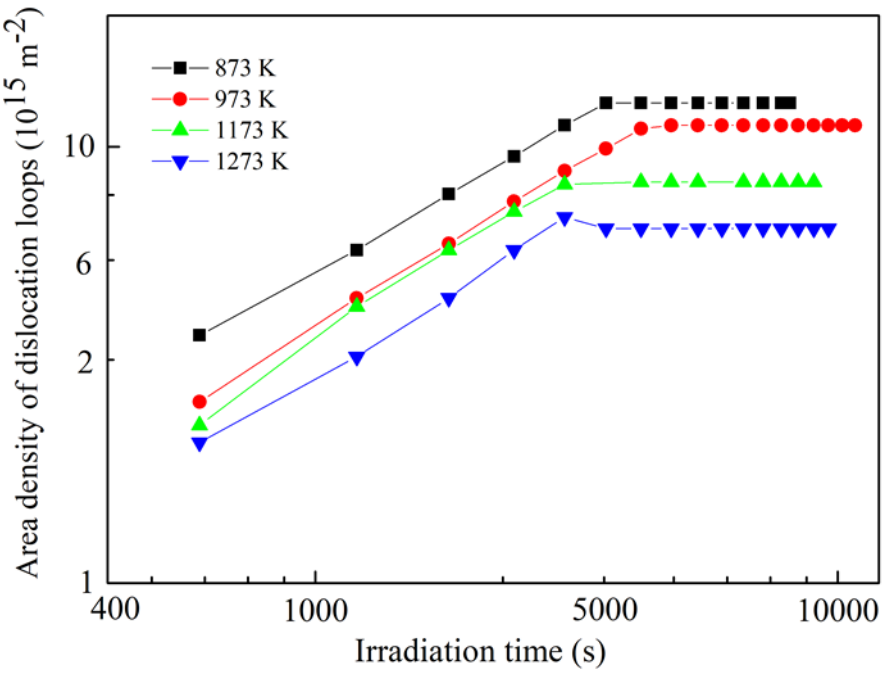

Figure 5.6 Temperature dependence of the saturated areal density of dislocation loops in ZrN under irradiation with 1250 keV at an electron flux of 4.4 ×10^{22} e^{-} m^{-2} s^{-1}.

The results shown in Figure 5.6 suggest that the nucleation process of dislocation loops presumably follows the same kinetic process at the present irradiation temperatures. It is also seen that the saturation density of dislocation loops is dependent on irradiation temperature.

Namely, the lower density is obtained at higher irradiation temperature. The average size of dislocation loops increases linearly with irradiation time without significant dependence among the irradiation temperatures of 873 K to 1273 K as shown in Figure 5.7 and 5.8.

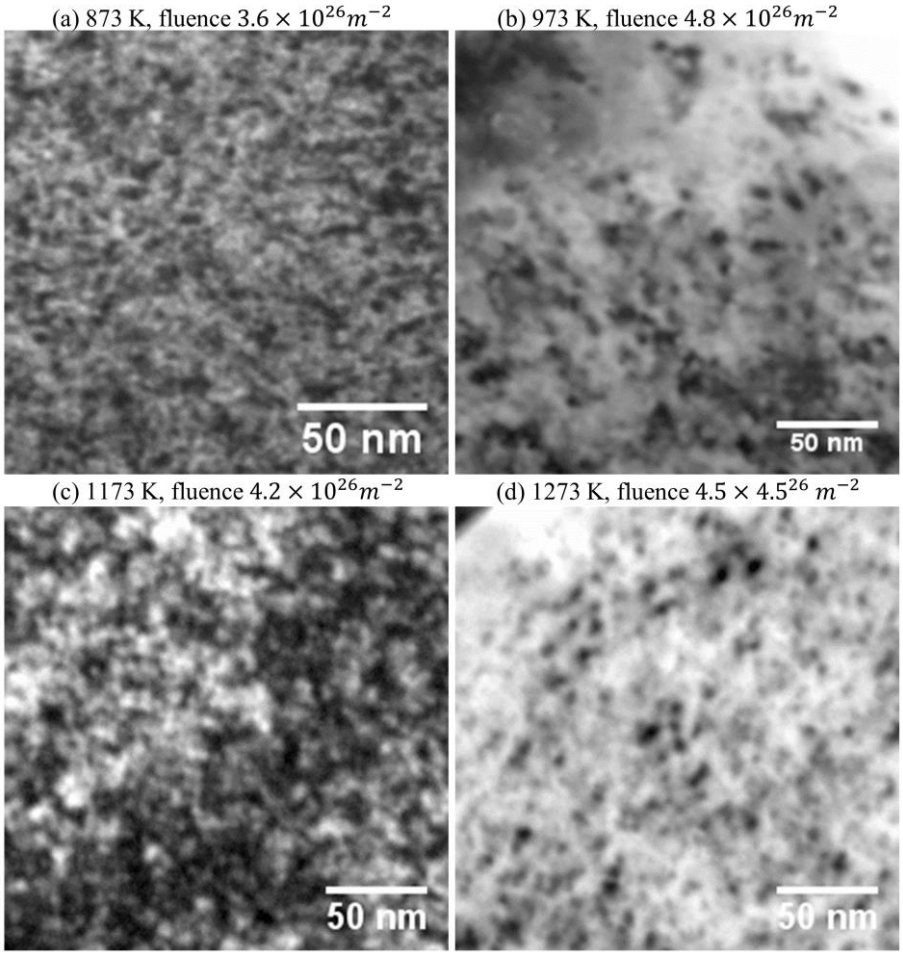

Figure 5.7 BF images of dislocation loops formed in ZrN irradiated with 1250 keV to a flux about of 4.4 $\times 10^{22}$ e m^{-2} s^{-1} at (a) 873, (b) 973, (c) 1173 (WBDF), and (d) 1273 K. These micrographs are taken with $\boldsymbol{g}$ = 002.

The nucleation-and-growth of dislocation loops under electron irradiation should be controlled by the thermally activated diffusion process of point defects since isolated Frenkel defects are produced under electron irradiation. If the nuclei of dislocation loops are assumed to be di-interstitials or a pair of Zr and N interstitials, the concentration of dislocation loops is

expected to saturate in a shorter time of irradiation under the typical electron flux (~10^{-4}~10^{-3} dpa/sec), as described for some metals and MgO.

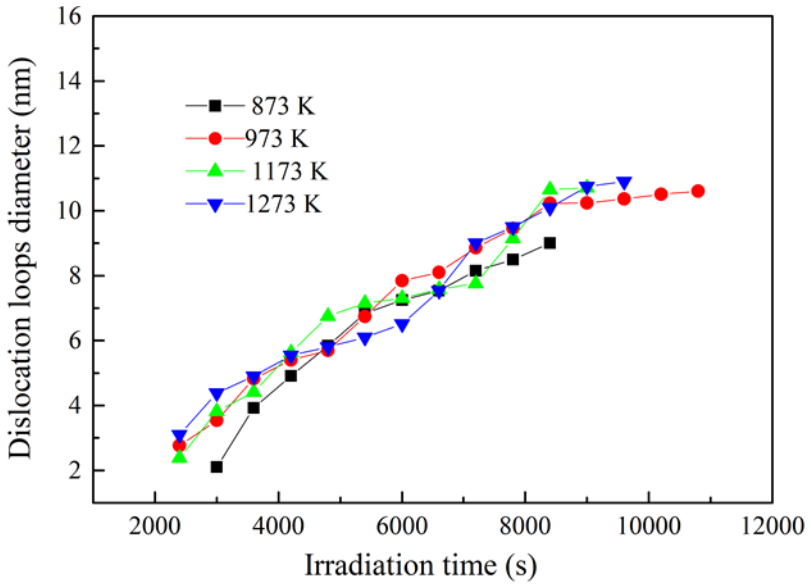

Figure 5.8 Typical plots of loop diameter versus irradiation time in ZrN. The loops grow with the relation $D \alpha t^n$, where D is the diameter of loops, t the irradiation time and n a constant independent of t.

On the other hand, some ceramic compounds are known for the slow nucleation of loops. For example, TiC_{1-x} did not show the saturation of loop density at the early stage of irradiation, but showed the gradual increase of the density. This is attributed to the existence of structural vacancies at the C sublattice due to the nonstoichiometric composition. A high concentration of structural vacancies is discussed to promote the recombination of interstitials, resulting the slow nucleation of dislocation loops. The particular nucleation feature in ZrN shown in interstitials. is not cleared at the present time. One possible explanation is that ZrN has a wide range for non-stoichiometric composition as ZrN_{1-x}. This may induce the recombination of displaced N interstitials with the structural N vacancy sites as discussed for TiC_{1-x} and depress the concentration of interstitial atoms necessary for the nucleation of dislocation loops.

If a pair of Zr and N interstitials are the nuclei of interstitial-type dislocation loops (C_L), the rate equation theory gives that the saturated density of loops are dependent on electron flux and the mobility of interstitials as follows [144],

$$C_L \, \alpha \, (C_M \, \varphi / M_B)^{1/2} \tag{5.1}$$

where C_M is the saturated density of loops, φ is the electron flux, and M_B is the mobility of interstitials expressed by the following equation.

$$M_B = v \exp\left(-\frac{E_M^I + B}{kT}\right) = v \exp(-\frac{E_M^{I'}}{kT}) \tag{5.2}$$

here, v is the vibration frequency of atoms, k is Boltzmann constant, E_M^I and B are the migration energy of interstitials and that of impurities. $E_M^{I'}$ is the migration energy of interstitials which takes impurity effects into consideration [144]. To insert Equation ((5.2) into ((5.1) and take logarithmic, then one can obtain the relationship between C_L and $1/T$,

$$lnC_L = lnA + \frac{1}{2}(\frac{E_M^{I'}}{kT}) \tag{5.3}$$

where A is a constant equivalent to displacement cross-section of atoms. Figure 5.9 plots the least-square approximation between C_L and $1/T$, and the relationship gives a good linear correlation (Figure 5.9). From the equation (5.3), the slope of Figure 5.9 gives the value of the migration energy of interstitials of rate controlling species, or presumably Zr atoms. To calculate the migration energy using fluencies dependent experimental data at different electron irradiation temperatures. After long time electron irradiation to become dislocation loops

saturate stage, for this reason, flux dependence electron irradiation observation little complicated and time consumed. The evaluated of migration energy of interstitial atoms is (0.48 ± 0.07) eV and this is the first evaluation of interstitial migration energy in ZrN. The validity of the evaluated value is difficult because of the no literature values, but this is close to the interstitial migration energy of 0.6 eV for Al interstitial ions in α-Al_2O_3 [145].

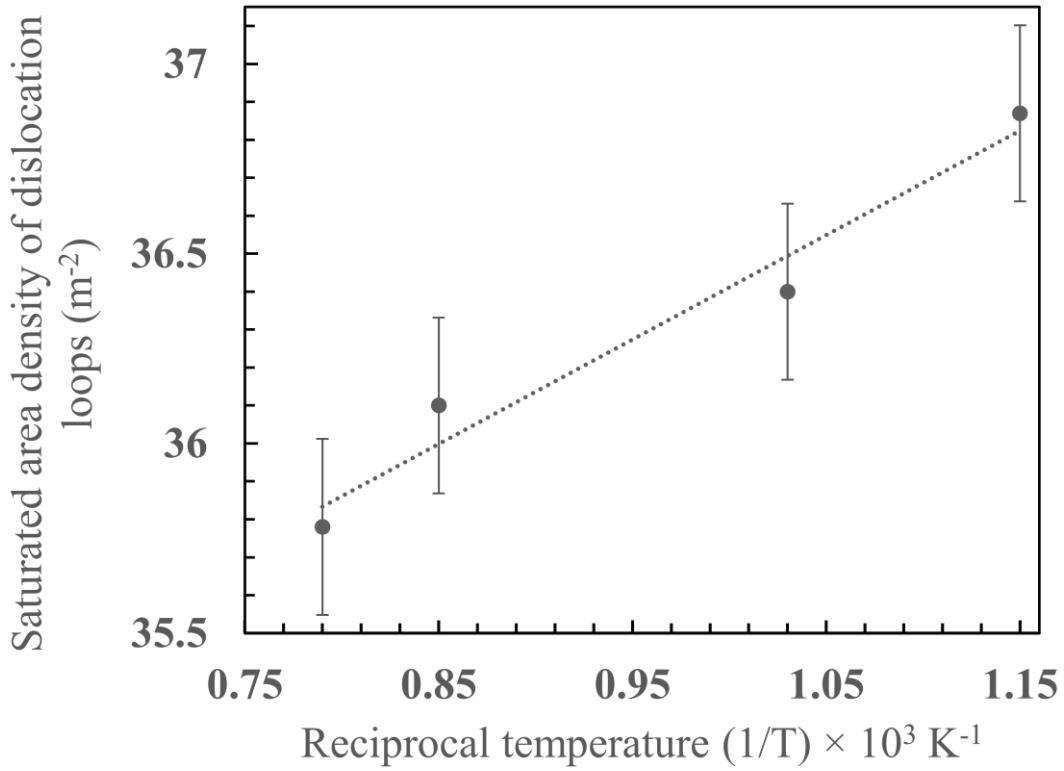

Figure 5.9 Temperature dependence of the area density of dislocations loops in ZrN under irradiation with 1.25 MeV electron flux of 4.4 ×10^{22} e m^{-2} s^{-1}.

5.4 Electron energy dependent dislocation loop formation

As described in Section 5.1, the displacement cross-section in ZrN showed that only N atoms are displaced selectively in ZrN at energies less than around 600 keV, and the displacement cross-section for Zr and N atoms showed an approximate same value at energy of 800 keV. The displacement cross-section evaluation was performed under assumptions of

22 eV and 16 eV for Zr and N atoms, respectively, which correspond to the E_d values in the <110> direction, where the microstructure observations were carried out. In conclusion, electron irradiation in ZrN induces the point defect formation only for N atoms at energies less than around 600 keV, and both N and Zr atoms at energies higher than the energy, although some errors for the energy can be expected.

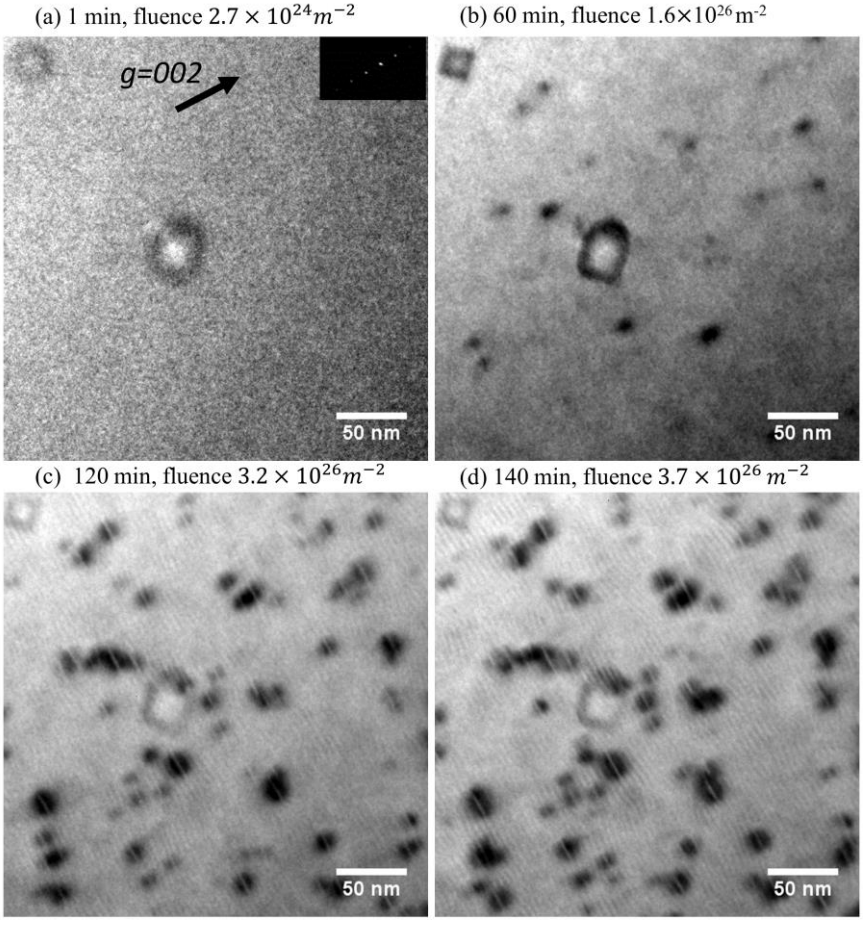

Figure 5.10 Bright field images of ZrN irradiated with 400 keV electrons at 973 K in a HVEM to a flux of 4.4×10^{22} e m^{-2} s^{-1} for different irradiation time.

Zirconium nitride (ZrN) specimens were irradiated with 400 keV electrons at a temperature of 973 K. Figure 5.10 shows a sequential change of the bright field (BF) micrographs in ZrN irradiated with 400 keV electrons at a constant flux of 4.4×10^{22} e m^{-2} s^{-1}. In the BF micrograph of Figure 5.10 (a), no defect clusters are visualized after 1 min irradiation.

A small number of defect clusters appeared to be nucleated under the irradiation condition at approximately 15 min irradiation, and those are clearly seen at 60 minutes irradiation as shown in Figure 5.10 (b). The size and density of defect clusters increased with increasing irradiation time (Figure 5.10 (c-d)). It is anticipated from Figure 5.1 that N atoms are displaced at incident electron energies higher than around 150 keV, while no Zr atoms are displaced under 400 keV electron irradiation. The estimated values of displacement damage rate (dpa/sec) with the electron flux used in this study (4.4×10^{22} e m^{-2} s^{-1}) for N and Zr atoms are 4.84×10^{-5} s^{-1} and 0, respectively, with the average values of E_d obtained in this study ($E_{d,N}$ = 29 eV, $E_{d,Zr}$ = 33 eV). Namely, electron irradiation with 400 keV is obviously a selective displacement condition for N atoms.

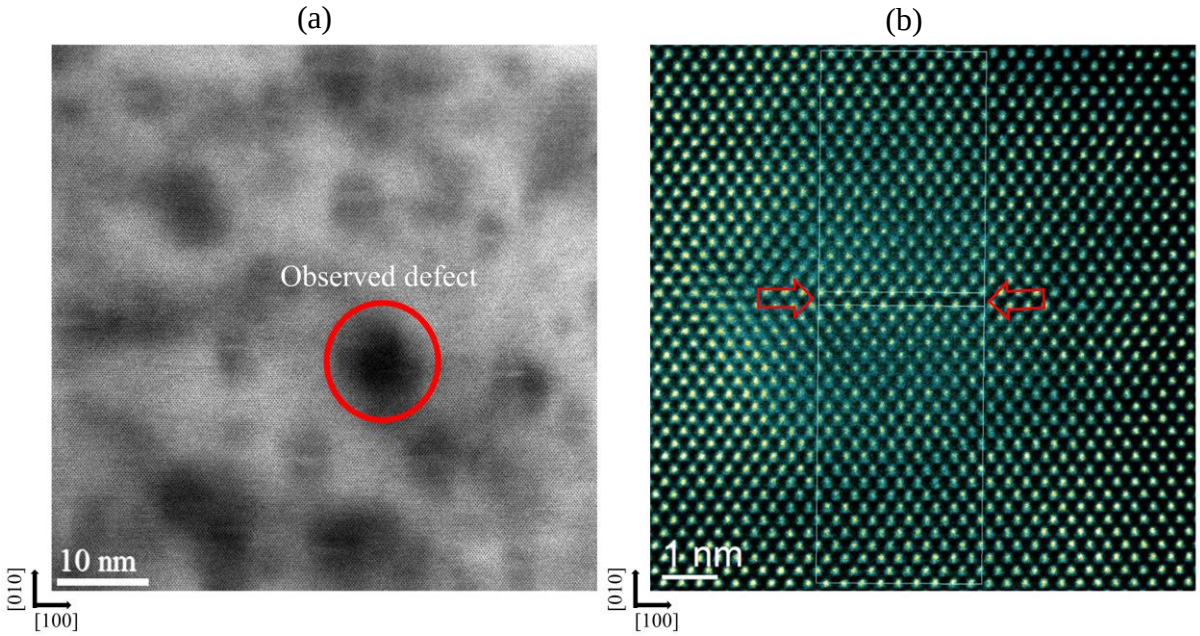

Figure 5.11 HAADF STEM image of dislocation loops in ZrN irradiated with 400 keV electrons at 973 K. Observation was performed with an accelerating voltage of 200 kV.

High-angle annular dark field (HAADF) technique with scanning transmission electron microscopy (STEM) imaging was applied to the dislocation loops formed with 400 keV electron irradiation. Figure 5.11 shows the HAADF-STEM images of dislocation loops with

(a) low magnification and (b) high magnification for the region indicated in (a). Figure 5.11 (a) shows that dislocation loops lie at {100} planes accompanying strong strained regions around the defects. Figure 5.11 (b) represents the atomic image of dislocation loops, showing the Zr atomic columns from the <110> direction. The contrast of HAADF-STEM technique is proportional to the square of *z* (*z*: atomic number), therefore, the image reflects mainly the atomic columns of the heavier elements. It is important to note that there is no additional Zr layers at the position of the dislocation loop (denoted by two arrows in Figure 5.11 (b)). The (100) plane of rock-salt structure consists both Zr and N atoms with the same composition. Therefore, if the additional plane of the dislocation loop retains the stoichiometric composition, the plane should include Zr atoms. The image shown in Figure 5.11 suggests that the dislocation loop accompanying strong strain contrast consists of solely N atoms. Conclusively, electron irradiations with 400 keV induces the interstitial-type non-stoichiometric dislocation loops consist of N atoms lying on {100} planes. This is the first observation of those nonstoichiometric dislocation loops in ZrN, and similar result observed in fluoride type oxides such as CeO_2, cubic zirconia [21].

5.4.1 Irradiation energy with 600 keV in ZrN

Figure 5.12 displays *in-situ* sequential TEM images of ZrN irradiated at 973 K by a focused electron beam with 600 keV. The BF TEM images were shot at a diffraction condition of $\boldsymbol{g}$ =002, and the electron beam direction was close to <110>. No defect clusters or dislocation loops were observed in the specimen after 5 minutes electron irradiation (Figure 5.12 (a)). The black dot-contrasts with a size of a few nm were started to be nucleated at 10 minutes irradiation. The black dot contrasts increased in size and the density to cover the whole irradiation area as shown in Figure 5.12 (b-d). At the saturated fluence, the size of dislocation

loops was 10-12 nm in average. The corresponding displacement damage at a fluence of 4.4×10^{22} e m^{-2} with 600 keV electrons was N 0.38 dpa and 0 dpa for N and Zr atoms, respectively. The nature of the dislocation loops was same with those observed with 400 keV electrons. However, the defect density was higher for 600 keV electron irradiation compared to 400 keV electrons.

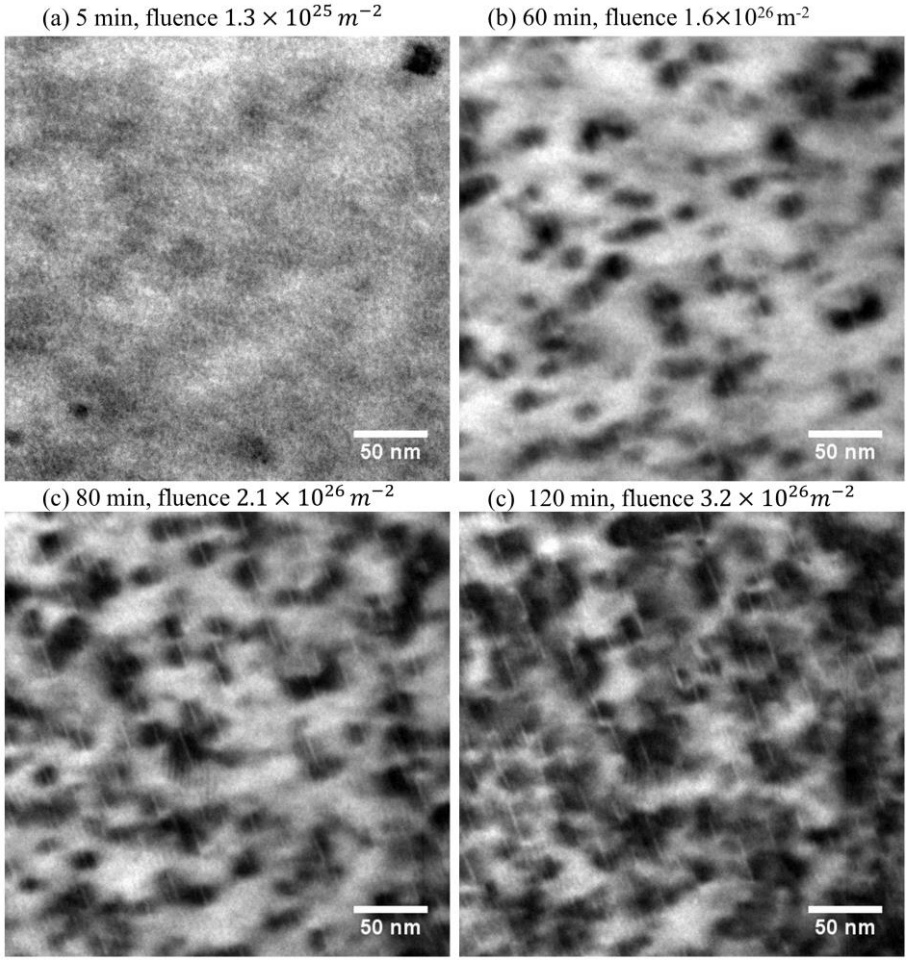

Figure 5.12 Bright field images of ZrN irradiated with 600 keV electrons at 973 K in a HVEM to a flux of 4.4×10^{22} e m^{-2} s^{-1} for different irradiation time.

5.4.2 Irradiation energy with 800 keV in ZrN

Figure 5.13 exhibits the sequential *in-situ* BF TEM images of the defects nucleated in ZrN specimen with 800 keV electron irradiation at 973 K at a flux of 4.4×10^{22} e/m^{2}s. At the initial irradiation time of about 1 minute, there was no visualized black dot-contrast (Figure 5.13(a)). We are monitoring the microstructure change during electron irradiation for approximately 2 hours in this conditions. The defect clusters nature was similar with those observed under 400 keV and 600 keV electron irradiation. In this condition, the size of defect clusters was small, and the density of defect clusters higher compared to 400 and 600 keV.

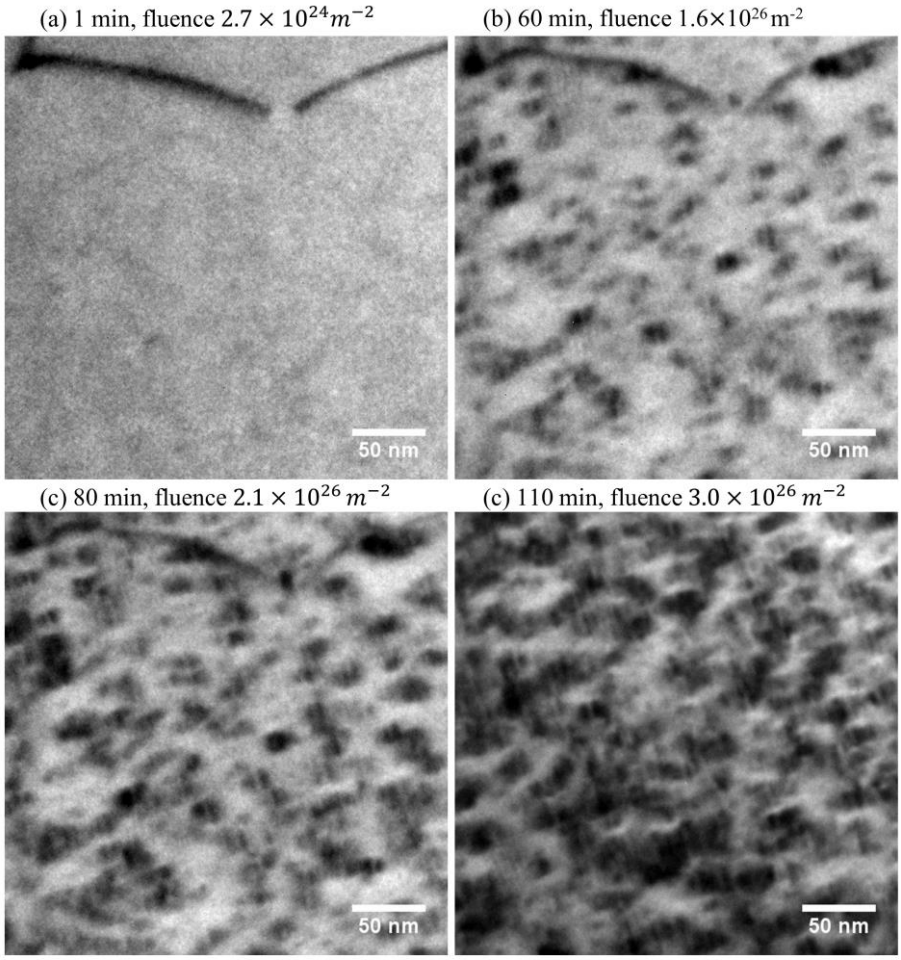

Figure 5.13 Bright field images of ZrN irradiated with 800 keV electrons at 973 K in a HVEM to a flux of 4.4×10^{22} e m^{-2} s^{-1} for different irradiation time.

5.4.3 Formation of perfect dislocation loops induced with electron irradiation 1000 keV

Figure 5.14 shows the BF-TEM micrographs of the microstructure of the defects nucleated in ZrN with 1000 keV electron irradiation at a constant flux of 4.4×10^{22} e $m^{-2}s^{-1}$ and temperature of 973 K. The black dot-contrasts were started to nucleate from the earlier of irradiation than 400 keV, 600 keV, and 800 keV. No black dot-contrasts were observed at an initial irradiated time (Figure 5.14 (a)). Increasing irradiation time also increased the density and sizes of dot-contrast (Figure 5.14 (b-d)). In this case, perfect type dislocation loops were formed as dpa values similar as shown in Figure 5.1. Interstitial-type non-stoichiometric dislocation loops of about more than 10 nm in diameter were only formed after electron irradiation at range 400 to 800 keV.

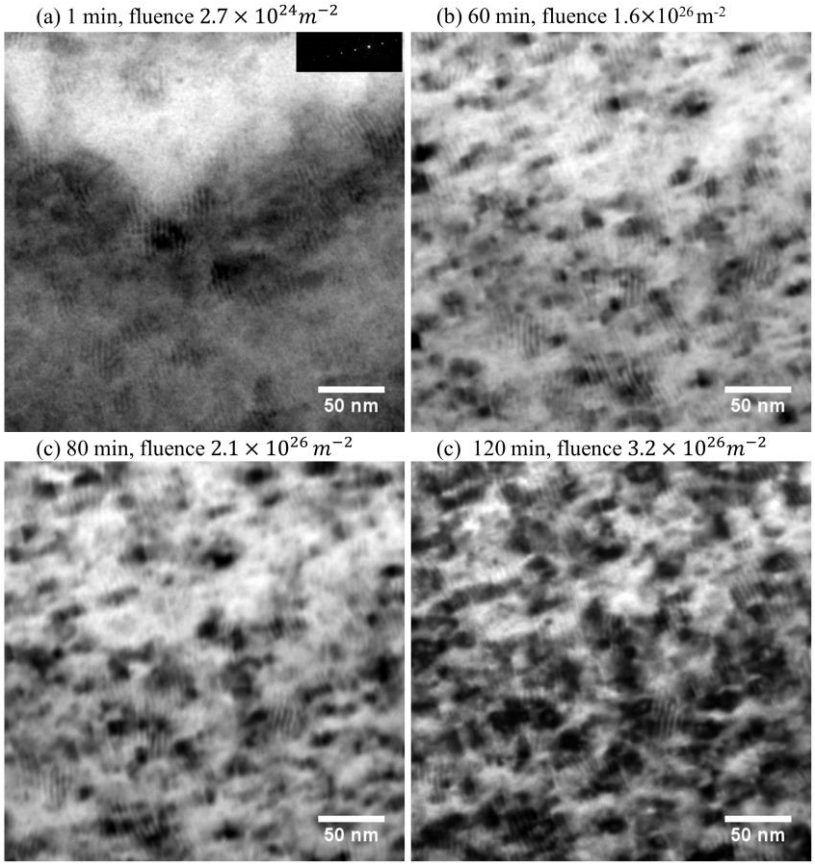

Figure 5.14 Bright field images of ZrN irradiated with 1000 keV electrons at 973 K in a HVEM to a flux of 4.4×10^{22} e m^{-2} s^{-1} for different irradiation time.

The defect clusters was formed different under 1000 keV electron irradiation energy compared to the lower electron irradiation energies from ranging 400 keV to 800 keV. It was clear evidenced from Figure 5.10, Figure 5.12, and Figure 5.13 to form plate type dislocation loops, however, from Figure 5.14 to show only black dot contrast. The density of defect clusters also increased and size decreases compared to lower irradiation energy. From this observation, we conclude that above 800 keV to form a perfect stoichiometric dislocation loops under electron irradiation energy. In contrast, the nature of interstitial-type perfect dislocation loops of ½<110>{110} and the segment of dislocations were formed with electron irradiation at 1250 keV.

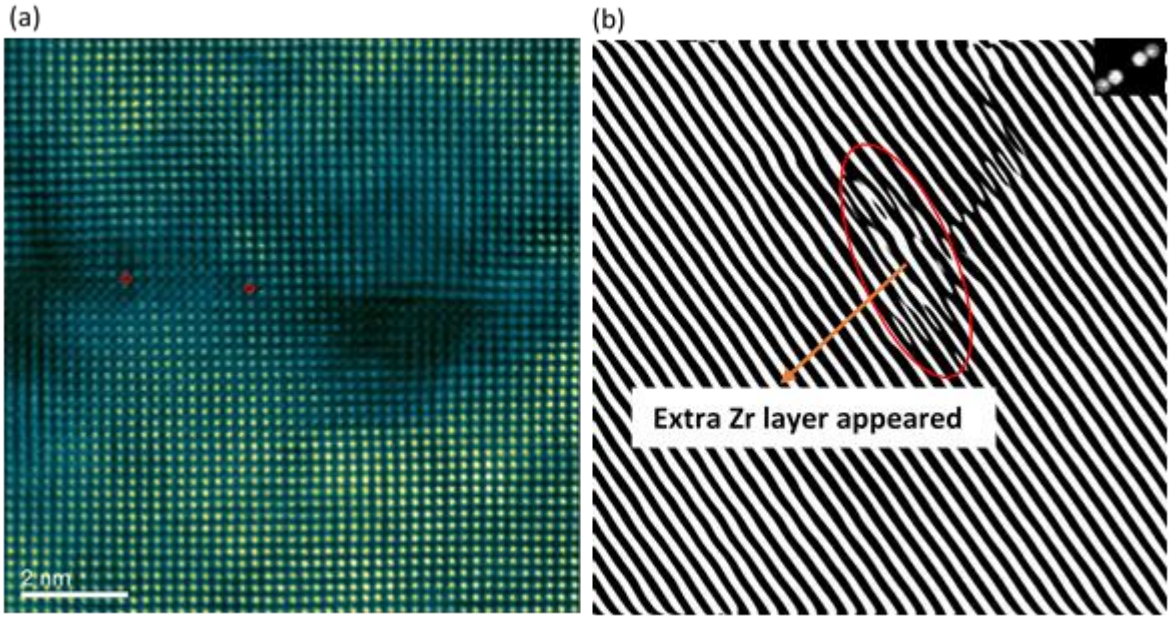

Figure 5.15 (a) HAADF-STEM image of dislocation loops in ZrN irradiated with 1250 keV electrons at 1173 K. Observation was performed with an accelerating voltage of 200 kV. (b) is an inverse FFT image of a dislocation loop in (a).

We also confirmed the formation of interstitial type perfect dislocation loops in the specimens irradiated at different temperatures 1273 K and 1173 K with 1250 keV Figure 5.15 (a-b). The formation of perfect dislocation loops revealed the knock-on displacements not only

for the nitrogen ions but also for the zirconium ions in ZrN using electron irradiation at 1250 keV. At higher electron irradiation energy with 1250 keV irradiated specimen area to observed HAADF STEM at 200 keV. Figure 5.15 (a) is shown easily understood another Zr atom layer appeared. Figure 5.15 (b) is shown inverse FFT also easily visualized the displacement occurred Zr atom in higher irradiation energy. As described early part of the result and discussion on microstructure changes with 1250 keV at 973 K with the same fluences.

5.5 Conclusions

A series of *in situ* irradiation experiments was performed on ZrN at different temperatures ranging from 873 K to 1273 K under high energy electron irradiation with 1250 keV, and energies from 400 keV to 1000 keV at a constant temperature of 973 K. We have carried out the investigation on the nucleation-and-growth process of perfect-type stoichiometric dislocation loops. Observation and analysis of radiation-induced defects of ZrN, the following conclusions are drawn.

Energetic electrons with energy 1250 keV for different temperatures are found to persuade defect clusters with Burgers vector parallel to the <110> directions. The growth behavior of dislocation loops is found not only depend on the electron energy but also depend on irradiation time and temperature. Electron energy 1250 keV is enough to form defect clusters in ZrN with perfect-type stoichiometric dislocation loops formed at 1250 keV electron irradiation.

The interstitial migration energy of Zr ion was estimated by the growth behavior of perfect dislocation loops from 1250 keV electron irradiation at 873 K to 1273 K and was found from slope is (0.48±0.07) eV.

The formation of perfect-type stoichiometric dislocation loops irradiation temperature is an important parameter. The interstitial type perfect dislocation loops of the *½<110>* type were formed 1000 keV and 1250 keV electron irradiations. Electron irradiations greater than 1000 keV induced not only N ions but also Zr ions with an atomic mass 6.5 times larger than that of N ions in ZrN. The ratio of the displacement rate of Zr and N sublattices, induced by the incident electron energies, controls the evolution of dislocation loops.

Chapter 6

Defect formation and accumulation in ZrN irradiated with swift heavy ions.

6.1 Introduction

Zirconium nitride (ZrN) is a potential candidate as ceramic targets of inert matrix fuel (IMF), and this compound can form a solid solution phase with transuranium (TRU) nitrides. It is, therefore, important to investigate the radiation responses of ZrN subjected to fission fragments. Fission fragments are high energy heavy ions or swift heavy ions (SHIs), and their typical energies of range from 70 MeV to 100 MeV. Most of the kinetic energy is dissipated in the fuel by electronic stopping, and there by high-density electronic excitation is an important factor for controlling the defect formation and microstructure evolution caused by SHIs. Unfortunately, however, limited investigations have been reported on ZrN irradiated with SHIs. Recently, Ogarkov et al. and Kuzenetsov et al. [45,46] observed the structural stability of ZrN irradiated by swift heavy ions of 167 MeV Xe, and they found that SHI irradiation induces no significant change of microstructure in ZrN. Also, Vuuren et al. [146] reported the radiation tolerance of nano-structured ZrN irradiated with 167 MeV Xe ions.

This chapter provides some insights into the radiation damage response of ZrN caused by SHIs of 200 MeV Xe. Transmission electron microscopy (TEM) was used to take the images of the defect clusters as a function of ion fluence and the penetration depth of ions.

6.2 Experimental procedure

6.2.1 Swift heavy ion (SHI) irradiation

Sintered ZrN sample fabrication and preparation was elaborately explained in Chapter 3. Surface of the specimens with 3 mm in thickness was polished to reduce to be 150-160 μm in thick and then irradiated with 200 MeV Xe ions at an ambient temperature under vacuum to fluences ranging from 3×10^{15} m^{-2} to 3×10^{16} m^{-2} using a Tandem Accelerator at Japan Atomic Energy Agency (JAEA). The electronic (S_e) and nuclear (S_n) stopping power of 200 MeV Xe ions were calculated by the SIRM (Stopping and Range of Ions in Matter) code [109], and the calculated result is shown in Figure 6.1. The value of S_e at the specimen surface is 31 keV/nm, and it gradually decreases to be zero at a depth of 11 μm. On the other hand, the value of S_n is negligible (<0.1 keV/nm) compared to S_e at the shallow depth, and it shows a peak at a depth of 11 μm. The value of S_e induced by FFs in nuclear fuel/target materials is around 20 keV/nm at the position where FFs are generated. It is noted, therefore, that the electronic stopping power used in the present study (31 keV/nm) is higher than the value of S_e in Zr-based nitride fuel and targets. The high value of S_e in this study is considered to make it easier to detect the microstructural change by depositing more energy the materials.

The irradiated specimens were thinned by mechanical and ion-thinning to be suitable to transmission electron microscopy for plan-view and cross section-view observations. Details of specimen preparation can be seen in Chapter 3. Examination of cross-section specimens allows the microstructure to vary against the values of S_e. Based on the results of cross-sectional observations, microstructure evolution by fission fragments in nuclear fuels, whose standard S_e values of 20 keV/nm, can be estimated. *In situ* observations of defect cluster formation and evolution of dislocation loops were performed at room temperatures at an accelerating voltage of 200 kV by using a TEM of 2100-HC (JEOL Ltd.) at the Ultramicroscopy Research Centre of Kyushu University.

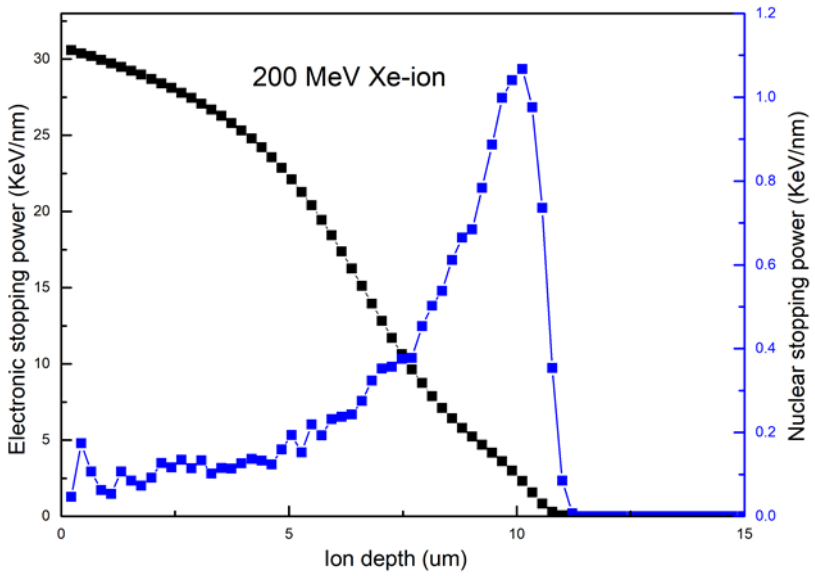

Figure 6.1 Depth profiles of electronic stopping power and nuclear stopping power of 200 MeV Xe ions in ZrN calculated by SIRM code.

6.3 Results and Discussion

Microstructure comparison between irradiated and unirradiated in ZrN specimen is shown in Figure 6.2 of BF-TEM images of plan-view samples taken from the near zone axis [110] with the diffraction vector of $\boldsymbol{g}$ = 002. The BF-TEM image of the unirradiated ZrN specimen at the surface region (Figure 6.2 (a)) shows no defect clusters and dislocation lines. This means that the Ar-ion milling process damage did not induce defect clusters in unirradiated samples. On the other hand, specimens irradiated with SHIs are observed with high-density dislocation lines and networks at the surface region for both fluences of 3×10^{15} m^{-2} and 3×10^{16} m^{-2} as shown in Figure 6.2 (b) and (c), respectively.

Figure 6.3(a) and (b) show plan-view bright-field (BF) images of an identical region in ZrN irradiated with 200 MeV Xe-ions to a fluence 3×10^{16} m^{-2} taken at an under-focus and an over-focus condition. Typical features of Fresnel contrast with white or black dot contrast were not observed in Figure 6.3. As a result, it confirms that ion-track formation was not induced in ZrN

specimens with SHI irradiation up to an electronic stopping of 31 keV/nm. This is a clear difference from oxide ceramics, such as CeO_2 and $MgAl_2O_4$, in which ion tracks with Fresnel contrast was observed higher than around 15 keV/nm.

It is also noted that Moire fringes appeared in ZrN specimen (indicated in Figure 6.2 (b) when we continued observations in the TEM approximately for 2 hours. This is probably due to the oxidation at the surface (formation of ZrO_2 at the surface). The similar observations were also reported during the observation in ZrN irradiated with 300 keV Kr ion [147], and it was different from ZrC [9].

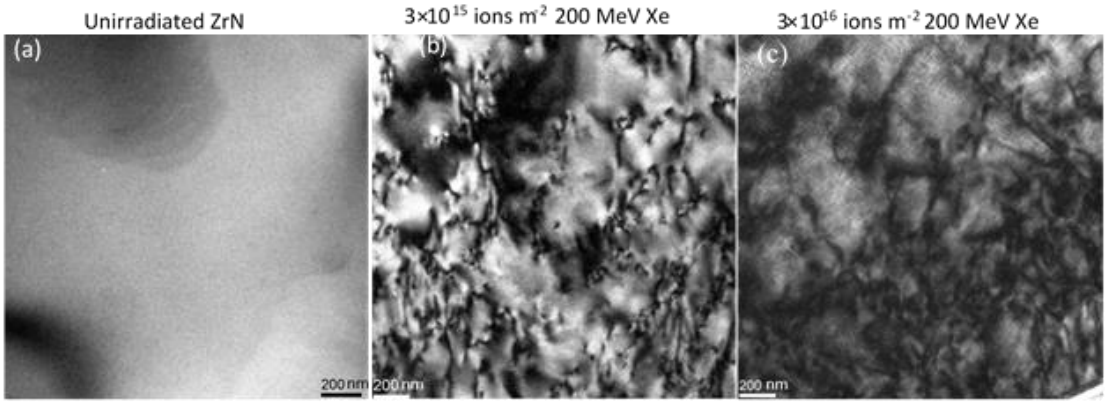

Figure 6.2 The microstructure of the unirradiated ZrN (a) and the irradiated ZrN ((b)and (c)) imaged with $\boldsymbol{g}$ = 002 near zone [110].

According to Benyagoub et al. [148], when low energy ions of 700 keV were irradiated to ceramics to induce partial or full amorphous regions, the melting temperature of amorphous regions were lower than those of the crystalline regions. SHI irradiation induce thermal sipkes more easily in amorphous or highly disordered regions. The interface between molten and crystalline regions will recover to crystalline state by epitaxial recrystallization. The recrystallization mechanism is an important factor to separate crystalline material and disordered regions in materials.

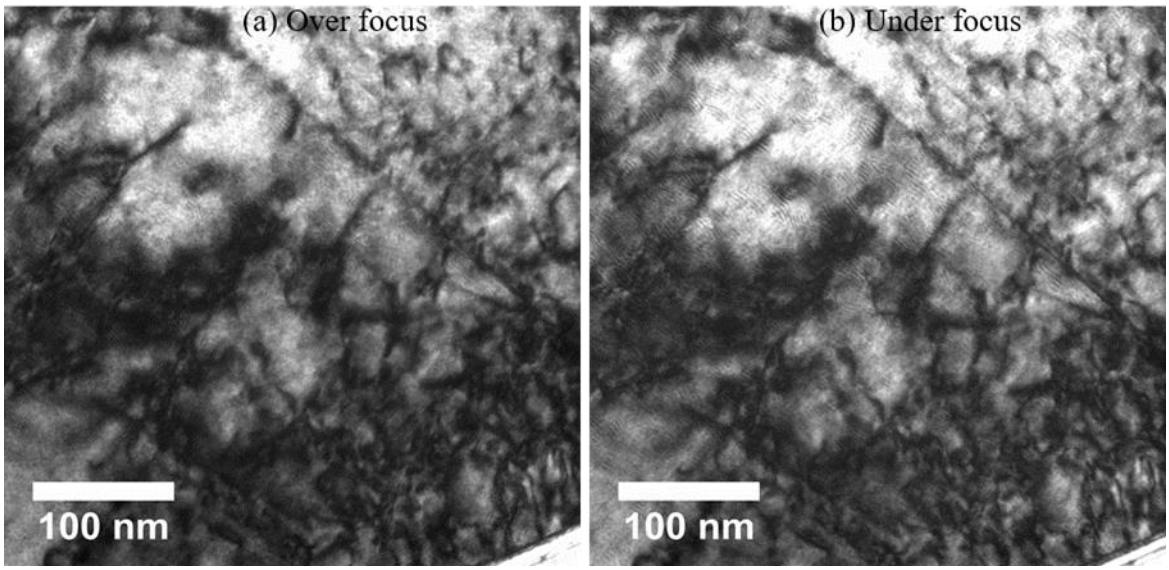

Figure 6.3 Plan-view microstructures from BF images of ZrN irradiated at ambient temperature with 200 MeV Xe ions to a fluence 3×10^{16} ions m^{-2}, taken with a kinematical diffraction condition with under-focus (a) and over-focus (b) conditions to observe the core damage regions no ion tracks with Fresnel-contrast.

Re-crystallization was occurred more quickly due to the very high mobility of lattice atoms in the liquid phase. According to Sahoo et al.[149], SHIs produce mainly vacancies inside ion tracks, which enhance recrystallization processes upon thermal annealing by lowering the energy required for the initiation of defect migration [150]. However, the ion-track formation was observed in oxide ceramics (e.g., CeO_2 and ZrO_2) [151]. One of the regions to form ion tack in oxide materials having a low melting temperature, as a result, recrystallization may not be easy in oxides. On the other hand, nitride ceramics have a high melting temperature, metallic features, and high electrical conductivity, there by easily recrystallization may occur easily in nitride ceramics than oxide ceramic materials. These properties are an important factor to prevent the ion-track formation for any materials.

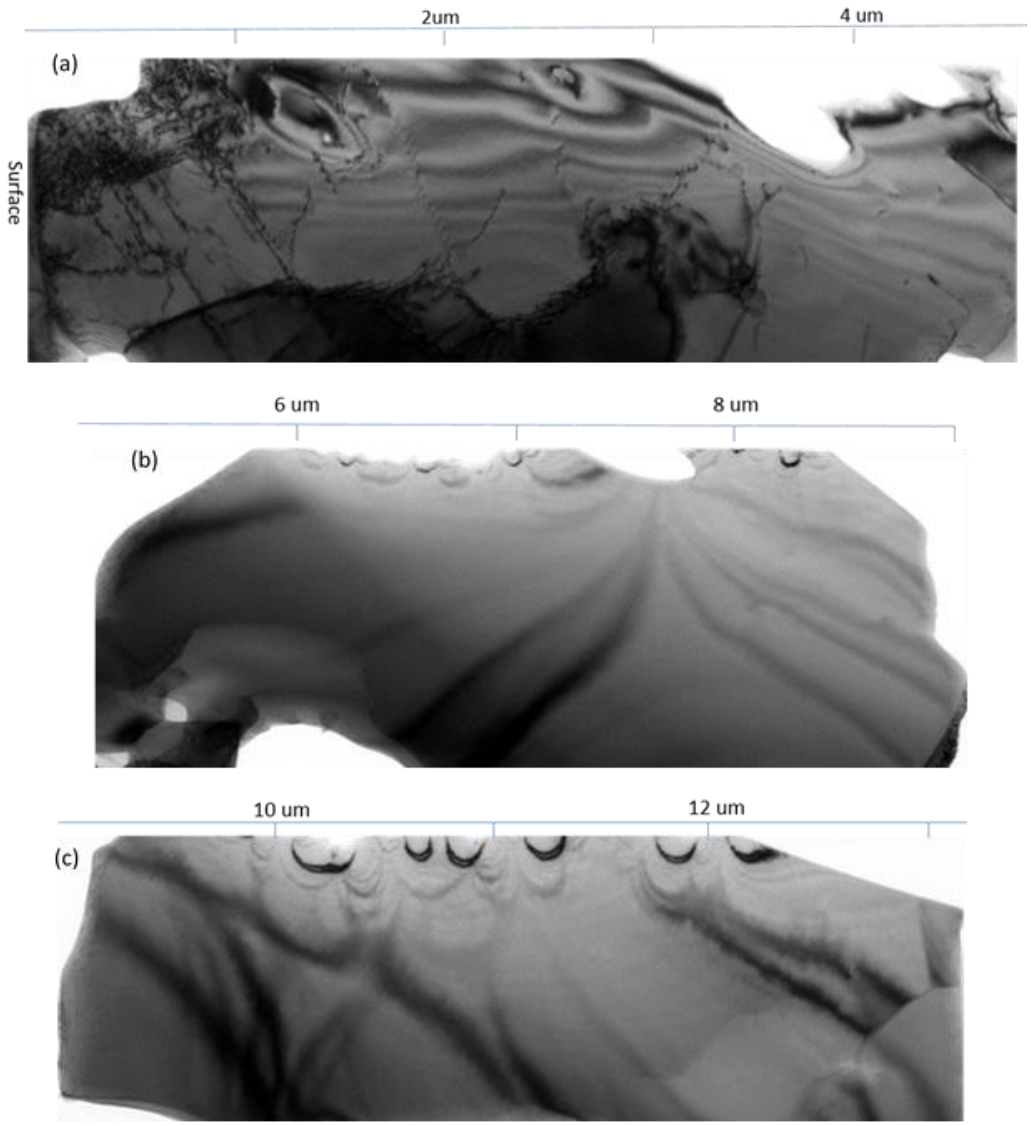

Figure 6.4 Cross-section BF image in ZrN irradiated at room temperature with 200 MeV Xe ions to a fluence 3×10^{15} ions m^{-2} in the (a), (b), and (c) in the micrograph.

6.3.1 Cross-sectional observations

Figure 6.4 shows BF images of a cross-sectional ZrN specimen irradiated with 200 MeV Xe ions at an ambient temperature to a fluence of $3 \times 10^{15}\ m^{-2}$. Figure 6.4 covers the whole the penetration depth of 200 MeV Xe ions (~10 µm). Tangled dislocation lines and small dislocation loops were observed at the shallower region up to the depth of 4 µm. Small

dot contrast was observed, on the other hand, at depth deeper than around 6 μm. According to the accumulation study of ion tracks in oxide ceramics, the density of ion tracks does not reach the saturation value at the fluence of more than 1×10^{16} m^{-2} [9]. Although ion tracks were not obserded in ZrN as described above, the results obtained by oxdes [9] suggest that the high density electronic exitaion damage does not overlap in ZrN at the fluence of 3×10^{15} m^{-2} to 3×10^{16} m^{-2}. Therefore, the microstructure evolution shown in Figure 6.4 was caused by an impact from single incident ions, but not by the overlaps of electronic excitation damage.

Figure 6.5 exhibits the high magnification BF images taken at different penetration depth of ions It is clearly seen dislocation lines in Figure 6.5(a) and (b), and dot contrast in (c) and (d).No dot-contrast was observed at the depth of 11and 12 μm as shown in Figure 6.4. This satisfies the SIRM simulation result shown in Figure 6.1. It is emphasized that the dislocation lines were formed at depth with high and low values of electronic and nuclear stopping power, respectively. As discussed above, the dislocation lines were formed from the impact of single incident ions with the electronic stopping power.

Shows Figure 6.6 depth-dependent microstructure of ZrN specimen, irradiated with 200 MeV Xe ions to a high fluence of $3\times10^{16}\ m^{-2}$. If we assume the same size of recovery region with CeO_2 [151] and $MgAl_2O_4$ [152] (15 μm in diameter), the fluence of 3×10^{13} m^{-2} corresponds to induce the overlap of electronic excitation damage for around several times. Similarly to the low fluence microstructure (Figure 6.4 and Figure 6.5), dislocation lines and networks were observed at the shallow depths approximately to 2 μm in depth. With increasing the penetration depth of ions, black dot contrast appeared at around 3 μm in depth, and the dot contrast was observed up to the depth of around 11 μm. This depth-dependent microstructure evolution is similar to corresponds to the range of 200 MeV Xe ions estimated by SIRM code (Figure 6.1) as qualitatively same with that developed at the fluence of 3×10^{15} m^{-2}.

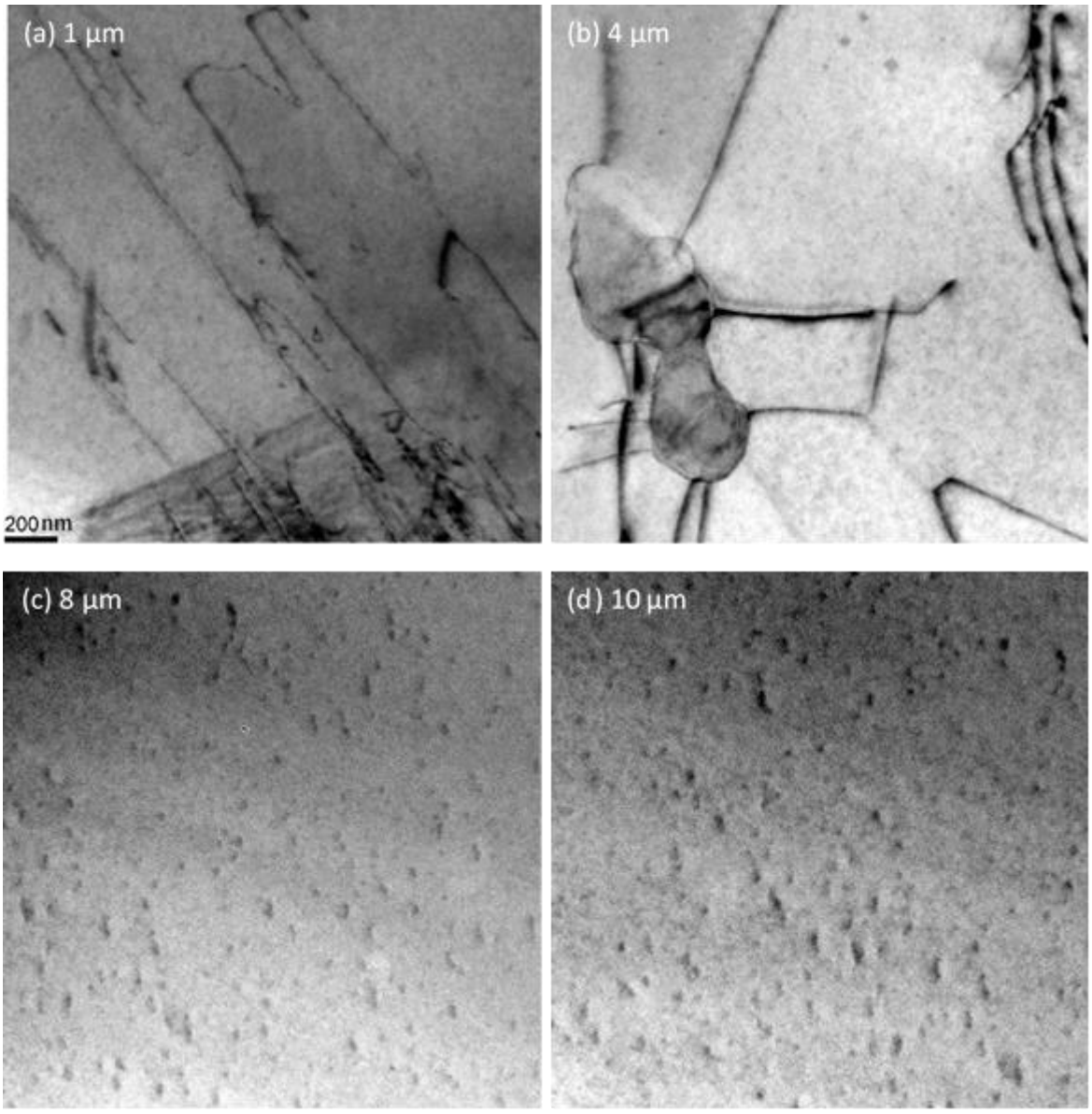

Figure 6.5 Cross-section BF images of ZrN irradiated with 200 MeV Xe ions to a fluence 3×10^{15} ions m^{-2} at a depth of (a) 1 µm, (b) 4 µm, (c) 8 µm, and (d) 10 µm.

The dot-contrast appeared at depth of 3 µm and 6 µm for fluences of 3×10^{16} m^{-2} and 3×10^{15} m^{-2} , respectively, and showed no contrast beyond the depth of 11 µm. The density of dot contrast was found to decrease with increasing the penetration depth of ions is shown in Figure 6.7. This result indicates that the dot contrast was induced by the electronic stopping

but not the nuclear stopping was found to decrease with increasing the penetration depth of ions.

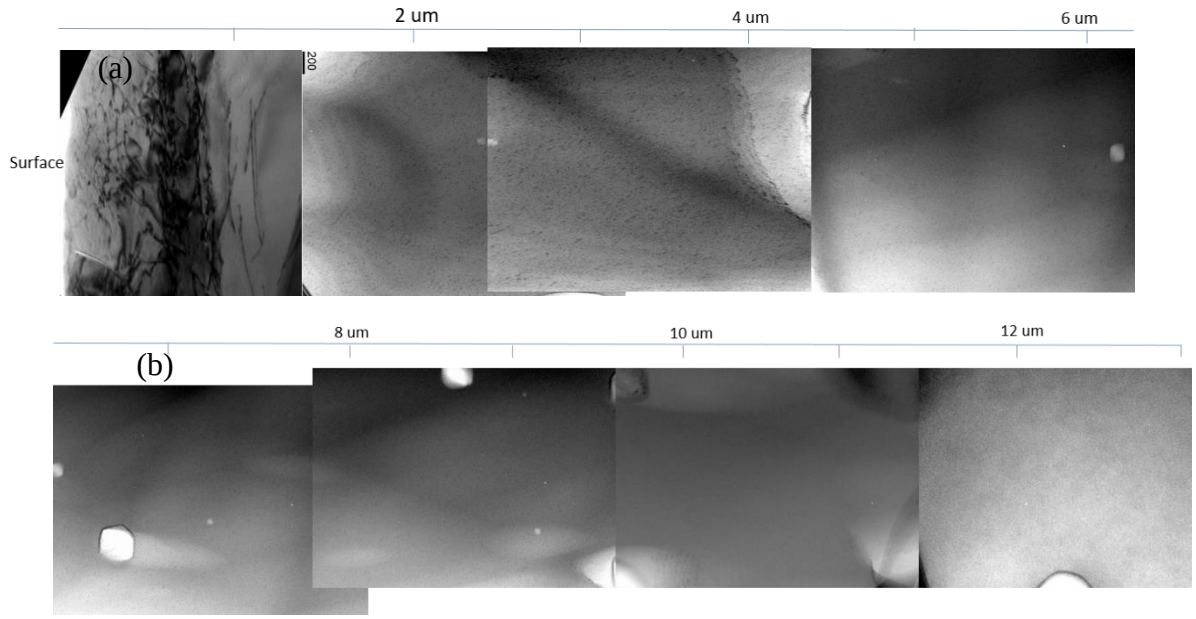

Figure 6.6 Cross-section BF image in ZrN irradiated at room temperature with 200 MeV Xe ions to a fluence 3×10^{16} ions m^{-2} in the (a) and (b) in the micrograph.

The threshold value of S_e for the dot contrast formation was estimated to be about 3-4 keV/nm (corresponding to the value of S_e at a depth between 10 and 11 μm). The difference in the contrast and the shape of two kinds of defects, or dislocation lines and dot contrast, revealed that those defects are different in nature. The nature of the dot contrast, such as the habit plane and Burger's vector, has not been clarified in this study. This is indispensable work in the future. There might be a possibility that the dot contrast is the defect with non-stoichiometric composition consist of only N atoms. Higher electronic stopping power at the shallower depth may induce displacements of both Zr and N atoms during the thermal spike regime, and presumably induce perfect dislocation lines when the region recovers. In the middle depth regions, N atoms might be preferentially displaced from the lattice sites to form the different

type of dot contrast defect. It can be clearly mentioned, however, that radiation response of ZrN with respect to SHIs is different from oxide ceramics. ZrN showed the superior response to 200 MeV Xe ion irradiation, and the detailed microstructure analysis is necessary as the future work to understand the physical mechanism and radiation tolerance of ZrN to SHI irradiation.

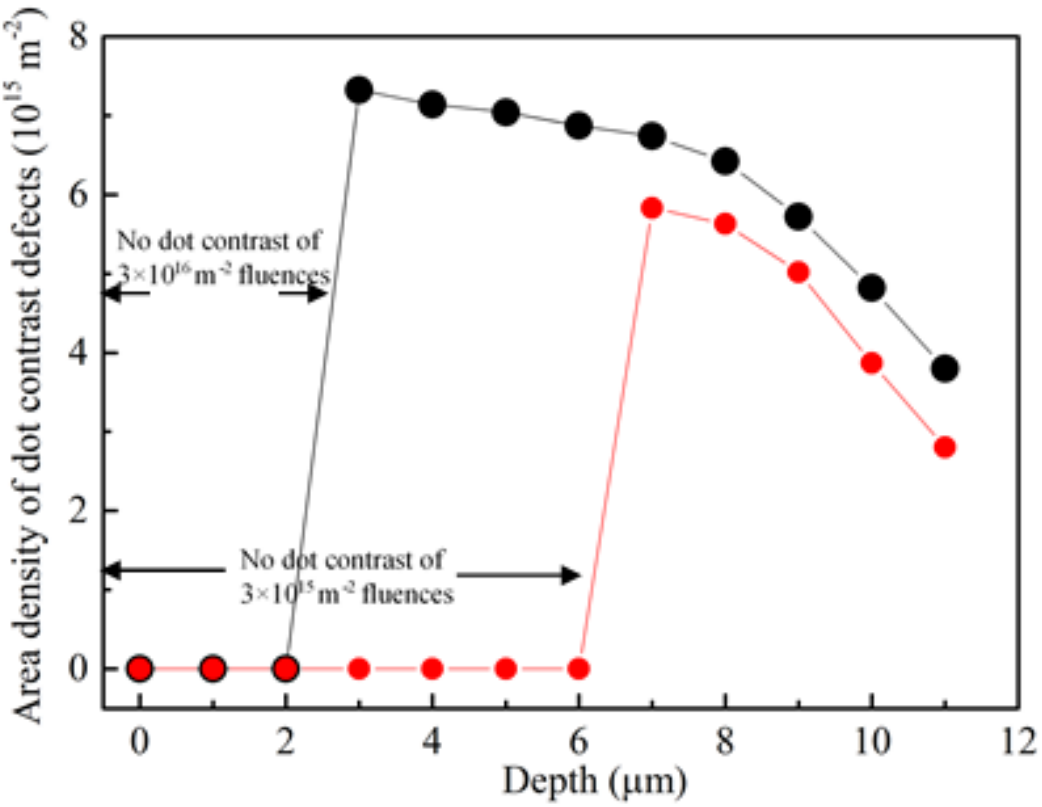

Figure 6.7 shows the areal density of dot contrast for ZrN specimens irradiated to a fluences of 3×10^{15} ions m^{-2} and 3×10^{16} ions m^{-2} with 200 MeV Xe ions.

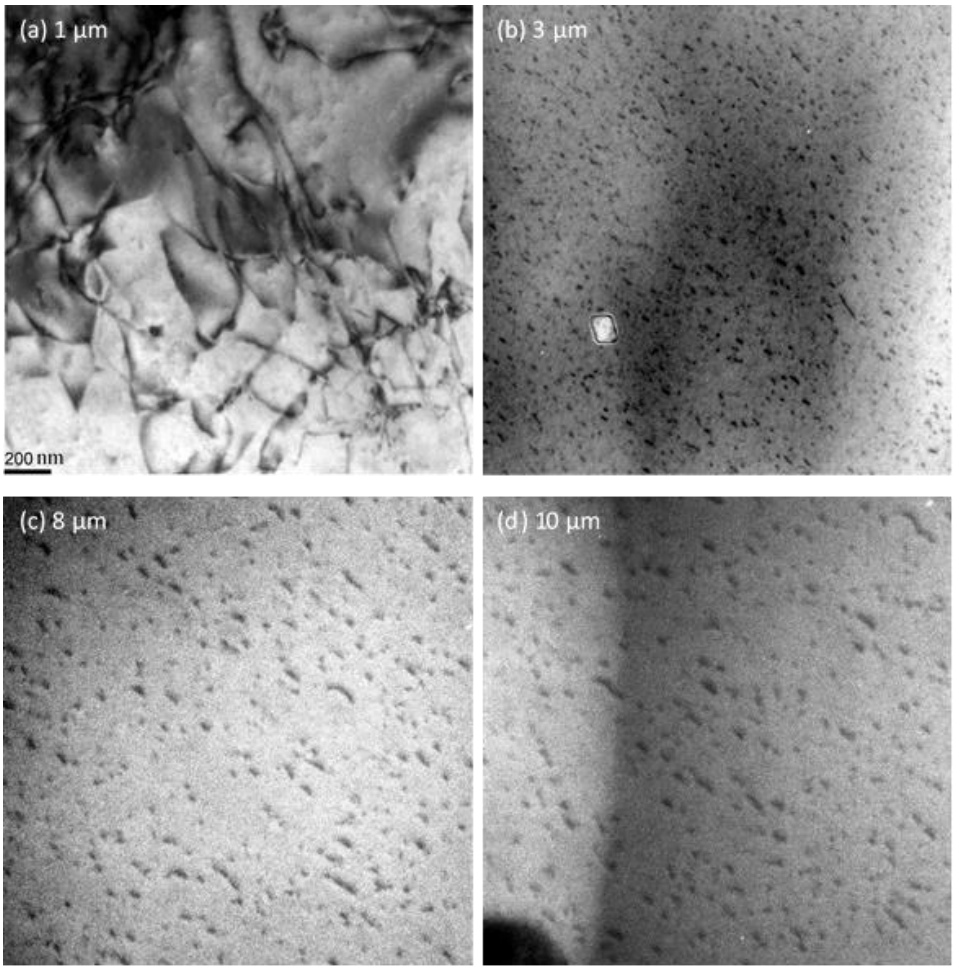

Figure 6.8 Cross-section BF images of ZrN irradiated with 200 MeV Xe ions to a fluence 3×10^{16} ions m^{-2} at a depth of (a) 1 µm, (b) 3 µm, (c) 8 µm, and (d) 10 µm.

The size of small black dot-contrast approximately similar up-to (3-11) µm depth regions. The SIRM depth profile shown in Figure 6.1 that the electronic excitation nearly zero, and nuclear stopping power are maximum at 11 µm. Ion-track was not observed at this stage. The high magnifying BF images as shown in Figure 6.8 for higher fluences. In the present study, the depth penetration observed by TEM and depth profile simulation using the SIRM code is consistent. That means nuclear excitation is not affected in ZrN specimen with 200 MeV Xe SHI irradiated. From this observation, preliminary concluded that the ZrN specimen is a strong radiation resistance material under high energy irradiated Xe ions.

6.4 Conclusions

We have investigated microstructure evolution in ZrN irradiated with 200 MeV Xe ions using TEM transmission electron microscopy.

The followings are drawn as conclusions in the present study:

- Ion-track formation was not induced in ZrN specimens with SHI irradiation up to an electronic stopping of 31 keV/nm. The high density of electron excitation was not overlap in ZrN fluences of 3×10^{15} m^{-2} to 3×10^{16} m^{-2}.
- Radiation damage with high-density electronic excitation induced dislocation lines, small dislocation loops and dot-contrast. The dot-contrast appeared at depth of 3 μm and 6 μm for fluences of 3×10^{16} m^{-2} and 3×10^{15} m^{-2}, respectively, and showed no contrast beyond the depth of 11 μm. Which are qualitatively consistent with SIRM depth profile for higher fluence. The density of dot contrast was found to decrease with increasing the penetration depth of ions.
- The microstructure evolution was caused by an impact from single incident ions, but not by the overlaps of electronic excitation damage. The high density of electron excitation evolves microstructure dependent on the penetration depth of ions, including small dislocation loops, dot-contrast, and line dislocations. Electron excitation was discussed to play an important role not only to induce dislocation loops, but also enhances migration of point defects, which are induced either by elastic or electronic stopping power.

Chapter 7

Concluding Remarks

7.1 General conclusions

Zirconium nitride (ZrN) is an essential material for nuclear industry to simulate inert matrices transuranium nuclear fuel for advanced reactor (e.g. ADS, FBR etc). It is now considered one of the potential matrices to be used as a target material for the transmutation of minor-actinides. ZrN would be subjected to various irradiations as a fuel matrix, e.g., alpha ray, beta ray, gamma ray, x-ray, neutrons, and enormous kinds of fission fragments that could chemically, thermally, and mechanically degrade the fuel/target materials. Therefore, researching the evolution of radiation damage in ZrN in acute circumstances has become a meaningful way to develop radiation tolerant materials. The experimental and simulation work's thrust in this dissertation was to investigate the production of point defects and nucleation-and-growth of defect clusters under various electron irradiation conditions and evaluation of threshold displacement energy by AIMD simulation. In this final chapter, the works done on ZrN under this dissertation will be summarized, and some areas that merit future research will be briefly described.

The threshold displacement energy, E_d, is one of the essential parameters in the radiation damage investigations. AIMD simulations were performed to evaluate E_d values in ZrN as a first attempt in this research field along with seven different crystallographic directions. The weighted values of E_d were determined to be 29 eV and 33 eV for the N and Zr atoms, respectively, exhibiting slightly larger values for Zr atoms. The values of E_d for both atoms were dependent on the crystallographic directions, which ranged from 15 eV to 50 eV. The minimum values of E_d for the N and Zr atoms were 16 eV and 22 eV, respectively, in the [110]

direction. Stable configurations of interstitial atoms were found to be tetrahedral sites and <111> split-type configurations for N and Zr atoms, respectively. It was also noted that replacement collisions along the <110> direction plays an important role for the collision process. Those features influence the difference of E_d values between Zr and N atoms, and among the initial PKA directions.

Systematic series of *in-situ* electron irradiation experiments were performed in a HVEM at temperatures ranging from 873 K to 1273 K under constant fluence and electron energy with 1250 keV. In situ experiments with different electron energy were also performed ranging from 400 keV to 1250 keV at a constant temperature of 973 K. In this condition, two different types of defect clusters were observed: those were non-stoichiometric dislocation loops and perfect stoichiometric dislocation loops. At electron energies ranging from 400 keV to 800 keV, non-stoichiometric dislocation loops, which is considered to include only N atoms, were observed, whereas at energies between 800 keV to 1250 keV, perfect-type stoichiometric dislocation loops were observed. All electron irradiation experiments were conducted by JEM-1300NEF (JEOL Ltd.) at a constant electron flux of ~4.4×10^{22} e $m^{-2}\cdot s^{-1}$. The migration energy is an important factor to investigate the radiation damage for any materials. The evaluation of migration energy is 0.48±0.07 eV with 1250 keV electron irradiated at different temperature in ZrN.

ZrN specimens were also irradiated with 200 MeV Xe^{14+} ions at Tandem-Accelerator facility of Japan Atomic Energy Agency-Tokai up to a fluence of 3×10^{15} m^{-2} to 3×10^{16} m^{-2}. This is a simulation experiment of fission products generated in the fuel/target materials, and the most energy loss was occurred by electronic stopping power. Ion-irradiated specimens was subjected to TEM observations in two ways: one is a plan view observation, and the other is a cross-sectional observation. The former was used to judge the formation of ion tracks or not with Fresnel contrast, and the later was used to observe microstructure as a function of the

penetration depth of incident ions. There were no ion track formation in ZrN irradiated with 200 MeV Xe ions. However, dislocation networks and small number of dislocation loops were observed at the surface region (up to 2 μm). With increasing the penetration depth, black dot contrast appeared to up to 11 μm in depth for the specimen irradiated to higher fluence. These dot contrast decreased with increasing the depth, and are considered with electronic stopping power but not with nuclear stopping power.

Based on the *ab-initio* molecular dynamics simulation (AIMD), *in-situ* electron irradiation experiments, and swift heavy-ion (200 MeV Xe) irradiation experiments in ZrN, the contributions of this dissertation are summarized below the followings:

- The threshold displacement energy was calculated using AIMD simulation. E_d values were strongly dependent on the crystallographic directions. E_d for Zr atoms was bracketed as $22 \leq E_{d,\,Zr} \leq 45$ in eV and E_d for N atoms was $15 \leq E_{d,\,N} \leq 50$. The weighted average values were 29 eV and 33 eV for the N and Zr atoms, respectively.

- Detailed monitoring of the traces of PKAs revealed that sequential replacement collisions to the [110] atomic row play an important role in the collision process, resulting in the lower values of E_d for both Zr and N atoms.

- Furthermore, there are obvious differences in the preferable interstitial configurations: the <111> split-type configuration is preferable for Zr interstitials and N interstitials occupy the tetrahedral sites, which also influence the difference in the values of E_d.

- The nucleation-and-growth process of dislocation loops was observed *in situ* at

temperatures ranging from 873 K to 1273 K under a constant electron irradiation energy with 1250 keV. The areal density of defect clusters increased with increasing irradiation time and around one and half hours became saturate. This defect clusters (dislocation loops) were perfect type stoichiometric dislocation loops. It was confirmed that from *g.b* analysis based on visualized and non-visualized creation of dislocation loops at identical region of irradiated ZrN specimen at different beam condition (e.g.*B*=[100], [110]). Further diffraction vector analysis to show about 80% dislocation loops were performed ½<110> burgers vector.

- The ratio of the displacement damage in cation and N sublattices in ZrN, induced by the incident electron energies, was a principal factor for inducing defect clusters nucleation-and-growth process.

- Migration energy is one of the important parameter to induce nucleation-and-growth process. The migration of vacancies and interstitials to be dependent on irradiation temperature and electron energy. The migration energy of Zr atom is evaluated 0.48±0.07 eV from temperature dependent observation.

- At electron irradiation energy blow around 800 keV only N atoms were displaced. Above 800 keV irradiation energy was observed perfect type dislocation loops. This phenomenon was confirmed from HAADF analysis using STEM microscope.

- No ion-track formation was observed in ZrN specimen with 200 MeV Xe swift heavy-ion irradiated an accelerating voltage of 200 kV.

7.2 Directions for future research

Recently, nuclear scientist tries to apply ZrN as a surrogate material of the nuclear fuel/target to understand the microscopic insights. However, the mechanism of displacement damage accumulation of defect clusters has not been fully understood yet. The experimental and simulation works conducted during this dissertation have helped to enhance the fundamental understanding of the production of point defects and the microstructure evolution. However, there remain quite a few challenges down the road before getting a radiation-resistant material to use in a practically harsh radiation environment.

It is emphasized that further systematic *in situ* electron irradiation investigations with the energy below 400 keV and above 1.25 MeV are necessary. Comprehensive studies with other advanced experimental characterization techniques, such as Rutherford backscattering spectrometry and channelling (RBS/C) and x-ray diffraction (XRD) with different sensitivities the radiation damage along with MD simulation, could be employed to the well-controlled stoichiometric compound of ZrN_{1-x}, since most of fabricated sintered bodies are considered to be stoichiometric composition.

My dissertation provides only primary idea about defect kinetics of nitride ceramic materials in ZrN. In future to observe more below energy around 100 keV to find the minimum irradiation energy to displaced N atoms. In the future simulation investigates, it might be interesting to create a vacancy in ZrN crystal as the initial condition, and observe effects of structural vacancies on the collision processes, which may influence the values of E_d and the configuration of vacancies and interstitials. It is noted that ZrN has no well established MEAM potential yet. For the cascade damage observation, DFT is not suitable because of the extremely long calculation time. Cascade damage observation needs a larger supercell. MEAM potential

is suitable for such type defect production and observation. In the future, I am interested in developing a new MEAM potential suitable for ZrN material to observe cascade damage phenomenon.

References

[1] (2019, April). IAEA-Power Reactor Information System (PRIS). Available:https:// www.iaea.org/PRIS/home.aspx.

[2] A. D. Brucklacher, F. Maschinenbau, Fed. Rep. Ger. Avil.INIS, Report,INIS-mf-5402, 1978.

[3] A. K. Sengupta, C. Ganguly ($Pu_{0.7}U_{0.3}$)N fuel for fast breeder test reactor-thermal conductivity and chemical compatibility with Ss 316 and sodium, Trans. Indian Inst. Met. (1990) 43 (1) 31.

[4] G.W. Egeland, J.A. Valdez, S.A. Maloy, K.J. McClellan, K.E. Sickafus, G.M. Bond, Heavy-ion irradiation defect accumulation in ZrN characterized by TEM,GIXRD, nanoindentation,andheliumdesorption,J.Nucl.Mater.435(2013)77–87. https://doi.org/10.1016/j.jnucmat.2012.12.025.

[5] M. Takano, A. Itoh, M. Akabori, K. Minato, Hydrolysis reactions of rare-earth and americium mononitrides, J. Phys. Chem. Solids. 66 (2005) 697–700. https://doi.org/10.1016/j.jpcs.2004.06.083.

[6] M. Takano, Experimental evaluation of solid solubility of lanthanide and transuranium nitrides into ZrN matrix, J. Nucl. Mater. 440 (2013) 489–494. https://doi.org/10.1016/j.jnucmat.2013.02.008.

[7] K.E. Sickafus, H. Matzke, K. Yasuda, P. Chodak, R.A. Verrall, P.G. Lucuta, H.R. Andrews, A. Turos, R. Fromknecht, N.P. Baker, Radiation damage effects in cubic-stabilized zirconia irradiated with 72 MeV I+ ions, Nucl. Instruments Methods Phys. Res. Sect. B Beam Interact. with Mater. Atoms. 141 (1998) 358–365. https://doi.org/10.1016/S0168-583X(98)00217-1.

[8] K. E. Sickafus, R. W. Grimes, J. A. Valdez, A. Cleave, M. Tang, M. Ishimaru, and S. M. Corish, C. R. Stanek, and B. P. Uberuaga, Radiation-induced amorphization resistance and radiation tolerance in structurally related oxides, Nat Mater,. (2007) vol. 6 pp.217–23.

[9] Y. Yang, C.A. Dickerson, T.R. Allen, Radiation stability of ZrN under 2.6 MeV proton irradiation, J. Nucl. Mater. 392 (2009) 200–205. https://doi.org/10.1016/j.jnucmat.2009.03.040.

[10] L. Jiao, K.Y. Yu, D. Chen, C. Jacob, L. Shao, X. Zhang, H. Wang, Radiation tolerant

nanocrystalline ZrN films under high dose heavy-ion irradiations, J. Appl. Phys. 117 (2015). https://doi.org/10.1063/1.4917381.

[11] V. V. Uglov, G. Abadias, S. V. Zlotski, I.A. Saladukhin, I. V. Safronov, V.I. Shymanski, A. Janse van Vuuren, J. O'Connell, V. Skuratov, J.H. Neethling, Features of microstructure of ZrN, Si3N4 and ZrN/SiNx nanoscale films irradiated by Xe ions, Vacuum. 143 (2017) 491–494. https://doi.org/10.1016/j.vacuum.2017.03.015.

[12] S. Takaki, M. Takano, N. Ishikawa, Progress in Nuclear Science and Technology, Prog. Nucl. Sci. Technol. (2017) 2–5.

[13] A.J. van Vuuren, Swift Heavy Ion Radiation Damage in Nanocrystalline Zrn, (2014).

[14] D.T. Olive, H. Ganegoda, T. Allen, Y. Yang, C. Dickerson, J. Terry, Using a spherical crystallite model with vacancies to relate local atomic structure to irradiation defects in ZrC and ZrN, J. Nucl. Mater. 475 (2016) 123–131. https://doi.org/10.1016/j.jnucmat.2016.04.004.

[15] M. Pukari, P. Olsson, N. Sandberg, He, Kr and Xe diffusion in ZrN - An atomic scale study, J. Nucl. Mater. 438 (2013) 7–14. https://doi.org/10.1016/j.jnucmat.2013.02.077.

[16] L. Jiao, Enhanced Radiation Tolerance of Ceramic Thin Films by Nano-structural Design, (2015) 66–78.

[17] D. Gosset, M. Dollé, D. Simeone, G. Baldinozzi, L. Thomé, Structural evolution of zirconium carbide under ion irradiation, J. Nucl. Mater. 373 (2008) 123–129. https://doi.org/10.1016/j.jnucmat.2007.05.034.

[18] D. Gossett, J. Morillo, C. Allison, C.H. de Novion, Electron irradiation damage in stoichiometric and substoichiometric tantalum carbides tacx, part 1: Threshold displacement energies, Radiat. Eff. Defects Solids. 118 (1991) 207–224. https://doi.org/10.1080/10420159108221360.

[19] M. Kiritani, H. Takata, Dynamic studies of defect mobility using high voltage electron microscopy, J. Nucl. Mater. 69–70 (1978) 277–309. https://doi.org/10.1016/0022-3115(78)90249-0.

[20] K. Yasunaga, K. Yasuda, S. Matsumura, T. Sonoda, Electron energy-dependent formation of dislocation loops in CeO2, Nucl. Instruments Methods Phys. Res. Sect. B Beam Interact. with Mater. Atoms. 266 (2008) 2877–2881. https://doi.org/10.1016/j.nimb.2008.03.204.

[21] K. Yasuda, S. Matsumura, S. Takaki, T. Yamamoto , M. Kutsuwada, Atomistic observation of electron irradiation-induced defects in CeO_2, Adv. Mateials Nucl. Energy. 1514 (2013) 93–98.

[22] K. Yasuda, C. Kinoshita, S. Matsumura, A.I. Ryazanov, Radiation-induced defect clusters in fully stabilized zirconia irradiated with ions and/or electrons, J. Nucl. Mater. 319 (2003) 74–80. https://doi.org/10.1016/S0022-3115(03)00136-3.

[23] B. Windes, W., Wendt, D., Bewley, R., O'Brien, Nitride fuel development at the INL., in: Sp. Nucl. Conf. 2007 - Proc. Embed. Top. Meet. SNC'07, 2007: pp. 196–199.

[24] U. Benedict, The solubility of solid fission products in carbides and nitrides of uranium and plutonium, part II: Solubility rules based on lattice parameter differences., 1977.

[25] C. Bailly, H., Menessier, D., Prunier, The Nuclear Fuel of Pressurized Water Reactors and Fast Reactors: Design and Behvaiour. Intercept Ltd., in: 1999.

[26] D. et al Grishchenko, Stockholm, Sweden, 3rd annual GENIUS meeting., in: 2012.

[27] J. Wallenius, CONFIRM final technical report: Collaboration on nitride fuel irradiation and modelling. Tech. rep., KTH., 2009.

[28] P.R. Hania, FAIRFUELS D 3.1.1, confirm - synthesis report PIE. Tech. rep., NRG., 2011.

[29] T. Ogawa, T. Ohmichi, A. Maeda, Y. Arai, Y. Suzuki, Vaporization behaviour of (Pu,Am)N, J. Alloys Compd. 224 (1995) 55–59. https://doi.org/10.1016/0925-8388(95)01512-4.

[30] CEA, Carbon-14 production and nitrogen-15 enrichment of nitride fuels. Tech. rep., Laboratoire des Irradiations., 2001.

[31] R. Thetford, M. Mignanelli, The chemistry and physics of modelling nitride fuels for transmutation, J. Nucl. Mater. 320 (2003) 44–53. https://doi.org/10.1016/S0022-3115(03)00170-3.

[32] S. Potter, R. A., (U,Zr)n alloy having enhanced thermal stability, Patent US4059539, 1977.

[33] L.M. Zabudko, MATINE - study of minor actinide transmutation in nitrides: Modeling and measurements of out-of-pile properties. Tech. rep., FSUE, ISTC Project No. 2680., 2006.

[34] O.F. Dense, F. For, L. Metal, C. Fast, 1950-1960 When in the fifties neutron physicists and engineers started to develop the reactors for obtaining access to the &, 153 (1988) 171–177.

[35] B.D. Rogozkin, N.M. Stepennova, A.A. Proshkin, Mononitride fuel for fast reactors, At. Energy. 95 (2003) 624–636. https://doi.org/10.1023/B:ATEN.0000007886.86817.32.

[36] M. Burghartz, G. Ledergerber, H. Hein, R.R. Van Der Laan, R.J.M. Konings, Some aspects of the use of ZrN as an inert matrix for actinide fuels, J. Nucl. Mater. 288 (2001)

233–236. https://doi.org/10.1016/S0022-3115(00)00722-4.

[37] R.J. Tilley, Crystals and crystal structures:John Wiley & Sons, 2006.

[38] C. R. Barrett, W. D. Nix, and A. S. Tetelman, The principles of engineering materials: Prentice hall, 1973.

[39] R. W.Grimshaw. and A. B. Searle, The chemistry and physics of clays and allied ceramic materials: Wiley-Interscience, 1971.

[40] C. B. Carter. and M.G. Norton, Ceramic materials: science and engineering: Springer Science & Business Media, 2007.

[41] D. Zanghi, A. Traverse, M.D.C. Martins Alves, T. Girardeau, J.P. Dallas, Structural characterization of ZrN implanted with high Co fluences, Nucl. Instruments Methods Phys. Res. Sect. B Beam Interact. with Mater. Atoms. 155 (1999) 416–425. https://doi.org/10.1016/S0168-583X(99)00474-7.

[42] A.J. Perry, A.J., Sartwell, B.D., Valvoda, V., Rafaja, D., Williamson, D.L., Nelson, Residual stress and the effect of implanted argon in films of zirconium nitride made by physical vapor deposition, J. Vac. Sci. Technol. A Vacuum, Surfaces Film. 10 (1992) 1446–1452.

[43] J. Gan, Y. Yang, C. Dickson, T. Allen, Proton irradiation study of GFR candidate ceramics, J. Nucl. Mater. 389 (2009) 317–325. https://doi.org/10.1016/j.jnucmat.2009.02.021.

[44] N. Yu, K. E. Sickafus, and M. Nastasi, First observation of'amorphization in single-crystal $MgA1_2O_4$ spinel, Philos. Mag. Lett. 70 (1994) 235–240.

[45] A. I. Ogarkov, S. V. Shevtsov, K. B. Kuznetsov, I. A. Kovalev, A. S. Chernyavskii, and K. A. Solntsev, Irradiation of titanium, zirconium, and hafnium nitrides with high-energy ions, Inorg. Mater. 52 (2016) 561–565.

[46] K. B. Kuznetsov, I. A. Kovalev, A. N. Nechaev, A. I. Ogarkov, S. V. Shevtsov, A. I. Ogarkov, S. V. Shevtsov, A. S. Chernyavskii, and K. A. Solntsev, Stability of the structure of compact zirconium nitride ceramics to irradiation with high-energy xenon ions, Inorg. Mater. 52 (2016).

[47] F. Lu, M. Huang, F. Yaqoob, M. Lang, F. Namavar, C. Trautmann, H. Sun, R.C. Ewing, J. Lian, Displacive radiation-induced structural contraction in nanocrystalline ZrN, Appl. Phys. Lett. 101 (2012). https://doi.org/10.1063/1.4738772.

[48] G.J. Corbeet, Electron radiation damage in semiconductors and metals, Academic press: New York, 1966.

[49] G. J. Dienes, G. H. Vineyard, Radiation effects in solids: Interscience publishers: New

York, 1957.

[50] W. Schilling, P. Ehrhart, and K. Sonnenberg, In fundamental aspects of radiation damage in metals, 1975.

[51] A. K. Seeger, In radiation damage in solids; IAEA: Vienna, 1962.

[52] F. Agullo-Lopez, C. R. A. Catlow, Point defects in materials. Academic press, San Diego, CA, 1988.

[53] M.W. Thompson, Defects and Radiatin Damage in Metals. Great Britain: Cambridge University Press, 1969.

[54] M. Kiritani, N. Yoshida, H. Takata, and Y. Meahara, growth of interstitial type dislocation loops and vacancy mobility in electrons irradiated metals, Journal of physical society of Japan, Vol. 38, pp. 1677-1686, 1975..

[55] N.F. Mott, Proceedings of the Royal Society A: Mathematical, Physical and Engineering Sciences, in: 1929: p. 426.

[56] N.F. Mott, Proceedings of the Royal Society A: Mathematical, Physical and Engineering Sciences, vol. 135, 1932.

[57] N.F. Mott. and H.S.W. Massey, The Theory of Atomic Collisions, 3rd ed. New York: Oxford University Press, 1965.

[58] W.A.McKinely, and H. Feshbach, The Coulomb scattering of relativistic electrons by nuclei, Phys. Rev. 74 (1948) 1759–1763.

[59] O. Oen, Cross sections for atomic displacements in solids by fast electrons, Oak Ridge National Lab., Tenn.(USA), 1973.

[60] J. A. Doggett, and L. V. Spencer, Phys. Rev., vol. 103, p.1597, (1956).

[61] P.D. Lesueur, Cascades de déplacement dam les solides polyatomiques, Philos. Mag. A Phys. Condens. Matter, Struct. Defects Mech. Prop. 44 (1981) 905–929. https://doi.org/10.1080/01418618108239557.

[62] J.M. Costantini, F. Beuneu, Threshold displacement energy in yttria-stabilized zirconia, Phys. Status Solidi Curr. Top. Solid State Phys. 4 (2007) 1258–1263. https://doi.org/10.1002/pssc.200673752.

[63] S .J. Zinkle, C. Kinoshita, Defect production in ceramics, J. Nucl. Mater. 251 (1997) 200–217.

[64] H.Y. Xiao, Y. Zhang, W.J. Weber, Ab initio molecular dynamics simulations of low-energy recoil events in ThO 2, CeO 2, and ZrO 2, Phys. Rev. B - Condens. Matter Mater. Phys. 86 (2012) 1–9. https://doi.org/10.1103/PhysRevB.86.054109.

[65] D.L. and J. Meese, Displacement thresholds in ZnO, Nucl. Sci. IEEE Trans. 19 (1972)

237–242.

[66] R. Bernstein, and R. Levine, Molecular Reaction Dynamics," Clarendon, Oxford, 1974.

[67] N. Mott. and M. Littleton, "Conduction in polar crystals. I. Electrolytic conduction in solid salts, in: Trans. Faraday Soc., 1938: pp. 485–499.

[68] A. Guglielmetti, A. Chartier, L. van Brutzel, J.P. Crocombette, K. Yasuda, C. Meis, S. Matsumura, Atomistic simulation of point defects behavior in ceria, Nucl. Instruments Methods Phys. Res. Sect. B Beam Interact. with Mater. Atoms. 266 (2008) 5120–5125. https://doi.org/10.1016/j.nimb.2008.09.010.

[69] H.Y. Xiao, F. Gao, W.J. Weber, Threshold displacement energies and defect formation energies in Y 2Ti2O7, J. Phys. Condens. Matter. 22 (2010). https://doi.org/10.1088/0953-8984/22/41/415801.

[70] E. Holmström, A. Kuronen, K. Nordlund, Threshold defect production in silicon determined by density functional theory molecular dynamics simulations, Phys. Rev. B Condens. Matter Mater. Phys. 78 (2008) 1–6. https://doi.org/10.1103/PhysRevB.78.045202.

[71] F. Gao, H. Xiao, X. Zu, M. Posselt, W.J. Weber, Defect-enhanced charge transfer by ion-solid interactions in sic using large-scale abinitio molecular dynamics simulations, Phys. Rev. Lett. 103 (2009) 1–4. https://doi.org/10.1103/PhysRevLett.103.027405.

[72] O.S. Oen, Cross sections for atomic displacements in solids by fast positrons, in: Nucl. Instruments Methods Phys. Res. Sect. B Beam Interact. with Mater. Atoms, Vol. 33, 1988: pp. 744–747.

[73] I. E. Fermi, P. Pasta, S. Ulam, and M. Tsingou, Studies of the nonlinear problems. Technical report, Los Alamos Scientific Lab., N. Mex, 1955.

[74] J.B. Gibson, A.N. Goland, M. Milgram, G.H. Vineyard, Dynamics of radiation damage, Phys. Rev. 120 (1960) 1229–1253. https://doi.org/10.1103/PhysRev.120.1229.

[75] A. Rahman, Correlations in the motion of atoms in liquid argon, Phys. Rev. 36(2) (1964) A405–A411.

[76] M. Parrinello, and A. Rahman, Crystal structure and pair potentials: A molecular-dynamics study, Phys. Rev. Lett. 45(14) (1980) 1196–1199.

[77] R.C. and M. Parrinello, Unified approach for molecular dynamics and density-functional theory, Phys. Rev. Lett. 55(22) (1985) 2471–2474.

[78] N. Metropolis, A. W. Rosenbluth, M. N. Rosenbluth, A. H. Teller, and E. Teller, Equation of state calculations by fast computing machines, J. Chem. Phys. 21 (1953) 1087–1092.

[79] B. J. Alder, and T.E. Wainwright, Phase transition for a hard sphere system, J. Chem. Phys. 27(5) (1957).

[80] F.H. Stillinger, A. Rahman, Molecular dynamics study of liquid water under high compression, J. Chem. Phys. 3336 (1974) 4973–4980. https://doi.org/10.1063/1.1681836.

[81] I.R. McDonald, NpT-ensemble monte carlo calculations for binary liquid mixtures, Mol. Phys. 23 (1972) 41–58. https://doi.org/10.1080/00268977200100031.

[82] H.C. Andersen, Molecular dynamics simulations at constant pressure and/or temperature, J. Chem. Phys. 72 (1980) 2384–2393. https://doi.org/10.1063/1.439486.

[83] M. Parrinello, A. Rahman, Polymorphic transitions in single crystals: A new molecular dynamics method, J. Appl. Phys. 52 (1981) 7182–7190. https://doi.org/10.1063/1.328693.

[84] D. Terme, S. Beitrag, D. Grund, V. Standpunkte, Der physik 1., (1927).

[85] K. Burke, L.O. Wagner, DFT in a nutshell, Int. J. Quantum Chem. 113 (2013) 96–101. https://doi.org/10.1002/qua.24259.

[86] D.R. Hartree, The wave mechanics of an atom with a non-coulomb central field. part i. theory and methods, in: Math. Proc. Cambridge Philos. Soc. 24, 1928: pp. 89–110.

[87] J.C. Slater, A simplification of the Hartree-Fock method, Phys. Rev. 81 (1951) 385–390. https://doi.org/10.1103/PhysRev.81.385.

[88] G.W. Pratt, Wave functions and energy levels for Cu+ as found by the slater approximation to the Hartree-Fock equations, Phys. Rev. 88 (1952) 1217–1224. https://doi.org/10.1103/PhysRev.88.1217.

[89] P. Hohenberg, and W. Kohn, Inhomogeneous electron gas, Phys. Rev. 136(3) (1964) B864– B871.

[90]. Kohn and L. J. Sham, Self-consistent equations including exchange and correlation effects, Phys. Rev. 140(4) (1965) A1133–A1138.

[91] B.Y. Tong, and L.J. Sham, Application of a self-consistent scheme including exchange and correlation effects to atoms, Phys. Rev. 144(1) (1966) 1–4.

[92] G. Kresse, and J. Furthmüller, Efficient iterative schemes for ab initio total-energy calculations using a plane-wave basis set, Phys. Rev. B. 54(16) (1996) 11169–11186.

[93] J.M. Soler, E. Artacho, J.D. Gale, A. García, J. Junquera, P. Ordejón, D. Sánchez-Portal, The SIESTA method for ab initio order-N materials simulation, J. Phys. Condens. Matter. 14 (2002) 2745–2779. https://doi.org/10.1088/0953-8984/14/11/302.

[94] X. Gonze, J.M. Beuken, R. Caracas, F. Detraux, M. Fuchs, G.M. Rignanese, L. Sindic,

M. Verstraete, G. Zerah, F. Jollet, M. Torrent, A. Roy, M. Mikami, P. Ghosez, J.Y. Raty, D.C. Allan, First-principles computation of material properties: The ABINIT software project, Comput. Mater. Sci. 25 (2002) 478–492. https://doi.org/10.1016/S0927-0256(02)00325-7.

[95] S. J. Stewart, M. D. Segall, C. J. Pickard, P. J. Hasnip, M. I. J. Probert, K. Refson, and M. C. Payne, First principles methods using CASTEP, Zeitschrift Für Krist. - Cryst. Mater. 220(5) (2009) 567–570.

[96] P. Giannozzi, S. Baroni, N. Bonini, M. Calandra, R. Car, C. Cavazzoni, D. Ceresoli, G.L. Chiarotti, M. Cococcioni, I. Dabo, A. Dal Corso, S. De Gironcoli, S. Fabris, G. Fratesi, R. Gebauer, U. Gerstmann, C. Gougoussis, A. Kokalj, M. Lazzeri, L. Martin-Samos, N. Marzari, F. Mauri, R. Mazzarello, S. Paolini, A. Pasquarello, L. Paulatto, C. Sbraccia, S. Scandolo, G. Sclauzero, A.P. Seitsonen, A. Smogunov, P. Umari, R.M. Wentzcovitch, QUANTUM ESPRESSO: A modular and open-source software project for quantum simulations of materials, J. Phys. Condens. Matter. 21 (2009). https://doi.org/10.1088/0953-8984/21/39/395502.

[97] K. Schwarz, P. Blaha, Solid state calculations using WIEN2k, Comput. Mater. Sci. 28 (2003) 259–273. https://doi.org/10.1016/S0927-0256(03)00112-5.

[98] Pseudopotential,2016. URL https:// en.wikipedia.org/w/index.php., (2016).

[99] S.R. Bahn, K.W. Jacobsen, L Anguages, Comput. Sci. Eng. 4 (2002) 56–66.

[100] B. Liu, H.Y. Xiao, Y. Zhang, W.J. Weber, Ab initio molecular dynamics simulations of overlapping recoil events in ThO_2, J. Phys. Condens. Matter. 25 (2013). https://doi.org/10.1088/0953-8984/25/39/395004.

[101] W.J.Weber. B Liu, H Y Xiao, Y Zhang, Y Zhang, Ab initio molecular dynamics simulations of threshold displacement energies in $SrTiO_3$, J. Phys. Condens. Matter. 2 (2013).

[102] B. Fultz, and J.M. Howe, Transmission electron microscopy and diffraction of materials, 2001.

[103] O. S. Heavens. and R.W. Ditchburn, Insight into optics Wiley Chichester, West Sussex,, England, 1991.

[104] K. Molhave, and P. Bøggild, Tools for in-situ manipulation and characterization of nanostructures," Lyngby: Technical University of Denmark, 2004.

[105] D. B. Williams, and C.B. Carter, The transmission electron microscope: Springer, 1996.

[106] P.J. Goodhew, Thin foil preparation for electron microscopy Elsevier, 1985.

[107] D. S. Rao, K. Muraleedharan, and C. Humphreys, TEM specimen preparation

techniques," Microscopy: Science, Technology, Aplications and Education, FORMATEX Research Center, Extremadura Es, 2010.

[108] K. Yasuda, C. Kinoshita, R. Morisaki, H. Abe, Role of irradiation spectrum in the microstructural evolution of magnesium aluminate spinel, Philos. Mag. A Phys. Condens. Matter, Struct. Defects Mech. Prop. 78 (1998) 583–598. https://doi.org/10.1080/01418619808241924.

[109] J. F. Ziegler, J. P. Biersack, and U. Littmark, The Stopping and Range of Ions in Solids, Pergamon, New York, 1985.

[110] D. Simeone, J.M. Costantini, L. Luneville, L. Desgranges, P. Trocellier, P. Garcia, Characterization of radiation damage in ceramics: Old challenge new issues?, J. Mater. Res. 30 (2015) 1495–1515. https://doi.org/10.1557/jmr.2015.77.

[111] K. Nordlund, S.J. Zinkle, A.E. Sand, F. Granberg, R.S. Averback, R.E. Stoller, T. Suzudo, L. Malerba, F. Banhart, W.J. Weber, F. Willaime, S.L. Dudarev, D. Simeone, Primary radiation damage: A review of current understanding and models, J. Nucl. Mater. 512 (2018) 450–479. https://doi.org/10.1016/j.jnucmat.2018.10.027.

[112] K. Yasuda, J.-M. Costantini, G. Baldinozzi, Radiation-Induced Effects on Material Properties of Ceramics: Mechanical and Dimensional Properties, Elsevier Ltd., 2020. https://doi.org/10.1016/b978-0-12-803581-8.12052-1.

[113] T.F. Mokgadi, M.J. Madito, M. Mlambo, V.A. Skuratov, S. V. Motloung, T.T. Hlatshwayo, Slow and swift heavy ions irradiation of zirconium nitride (ZrN) and the migration behaviour of implanted Eu, Nucl. Instruments Methods Phys. Res. Sect. B Beam Interact. with Mater. Atoms. 461 (2019) 63–69. https://doi.org/10.1016/j.nimb.2019.09.031.

[114] K. Nordlund, Historical review of computer simulation of radiation effects in materials, J. Nucl. Mater. 520 (2019) 273–295. https://doi.org/10.1016/j.jnucmat.2019.04.028.

[115] X.J. Wang, H.Y. Xiao, X.T. Zu, Y. Zhang, W.J. Weber, Ab initio molecular dynamics simulations of ion-solid interactions in Gd2Zr2O7 and Gd2Ti2O 7, J. Mater. Chem. C. 1 (2013) 1665–1673. https://doi.org/10.1039/c2tc00192f.

[116] G. Lucas, L. Pizzagalli, Comparison of threshold displacement energies in β-SiC determined by classical potentials and ab initio calculations, Nucl. Instruments Methods Phys. Res. Sect. B Beam Interact. with Mater. Atoms. 229 (2005) 359–366. https://doi.org/10.1016/j.nimb.2004.12.119.

[117] M.J. Zheng, I. Szlufarska, D. Morgan, Ab initio prediction of threshold displacement energies in ZrC, J. Nucl. Mater. 471 (2016) 214–219.

https://doi.org/10.1016/j.jnucmat.2015.08.053.

[118] H.Y. Xiao, F. Gao, X.T. Zu, W.J. Weber, Threshold displacement energy in GaN: Ab initio molecular dynamics study, J. Appl. Phys. 105 (2009). https://doi.org/10.1063/1.3153277.

[119] G. Lucas, L. Pizzagalli, Ab initio molecular dynamics calculations of threshold displacement energies in silicon carbide, Phys. Rev. B - Condens. Matter Mater. Phys. 72 (2005) 1–4. https://doi.org/10.1103/PhysRevB.72.161202.

[120] K.E. Sickafus, H. Matzke, T. Hartmann, K. Yasuda, J.A. Valdez, P. Chodak, M. Nastasi, R.A. Verrall, Radiation damage effects in zirconia, J. Nucl. Mater. 274 (1999) 66–77. https://doi.org/10.1016/S0022-3115(99)00041-0.

[121] L. Thomé, S. Moll, G. Sattonnay, L. Vincent, F. Garrido, J. Jagielski, Radiation effects in cubic zirconia: A model system for ceramic oxides, J. Nucl. Mater. 389 (2009) 297–302. https://doi.org/10.1016/j.jnucmat.2009.02.013.

[122] N. Troullier, J.L. Martins, Efficient pseudopotentials for plane-wave calculations, Phys. Rev. B. 43 (1991) 1993–2006. https://doi.org/10.1103/PhysRevB.43.1993.

[123] A. Menth, E. Buehler, T.H. Geballe, Magnetic and semiconducting properties of SmB6, Phys. Rev. Lett. 22 (1969) 295–297. https://doi.org/10.1103/PhysRevLett.22.295.

[124] J.P. Perdew, K. Burke, M. Ernzerhof, Generalized gradient approximation made simple, Phys. Rev. Lett. 77 (1996) 3865–3868. https://doi.org/10.1103/PhysRevLett.77.3865.

[125] F. Birch, Finite elastic strain of cubic crystals, Phys. Rev. 71 (1947) 809–824. https://doi.org/10.1103/PhysRev.71.809.

[126] B.A. Petersen, B. Liu, W.J. Weber, Y. Zhang, Ab initio molecular dynamics simulations of low energy recoil events in MgO, J. Nucl. Mater. 486 (2017) 122–128. https://doi.org/10.1016/j.jnucmat.2017.01.020.

[127] F. Gao, H.Y. Xiao, W.J. Weber, Ab initio molecular dynamics simulations of low energy recoil events in ceramics, Nucl. Instruments Methods Phys. Res. Sect. B Beam Interact. with Mater. Atoms. 269 (2011) 1693–1697. https://doi.org/10.1016/j.nimb.2011.01.131.

[128] M. Robinson, N.A. Marks, K.R. Whittle, G.R. Lumpkin, Systematic calculation of threshold displacement energies: Case study in rutile, Phys. Rev. B - Condens. Matter Mater. Phys. 85 (2012) 1–11. https://doi.org/10.1103/PhysRevB.85.104105.

[129] W.B. Parseon. (Ed.), Structure reports, International Union of Crystallography, Oosthoek, Scheltema, and Holkema, Utrecht.

[130] C. Stampfl, W. Mannstadt, R. Asahi, A.J. Freeman, Electronic structure and physical properties of early transition metal mononitrides: Density-functional theory LDA, GGA,

and screened-exchange LDA FLAPW calculations, Phys. Rev. B - Condens. Matter Mater. Phys. 63 (2001) 1–11. https://doi.org/10.1103/PhysRevB.63.155106.

[131] D. Cheng, S. Wang, H. Ye, First-principles calculations of the elastic properties of ZrC and ZrN, J. Alloys Compd. 377 (2004) 221–224. https://doi.org/10.1016/j.jallcom.2004.01.058.

[132] M.B. Kanoun, S. Goumri-Said, Effect of alloying on elastic properties of ZrN based transition metal nitride alloys, Surf. Coatings Technol. 255 (2014) 140–145. https://doi.org/10.1016/j.surfcoat.2014.03.048.

[133] Y. Arai, Chapter 3.02, comprehensive Nuclear Materials Vol.3, ed. R. J. M. Konings, T. R. Allen, R. E. Stoller, S. Yamanaka, Elsevier, 2012.

[134] K. Balasubramanian, S. V. Khare, D. Gall, Energetics of point defects in rocksalt structure transition metal nitrides: Thermodynamic reasons for deviations from stoichiometry, Acta Mater. 159 (2018) 77–88. https://doi.org/10.1016/j.actamat.2018.07.074.

[135] L. Tsetseris, N. Kalfagiannis, S. Logothetidis, S.T. Pantelides, Role of N defects on thermally induced atomic-scale structural changes in transition-metal nitrides, Phys. Rev. Lett. 99 (2007) 1–4. https://doi.org/10.1103/PhysRevLett.99.125503.

[136] B.P. Uberuaga, M. Tang, C. Jiang, J.A. Valdez, R. Smith, Y. Wang, K.E. Sickafus, Opposite correlations between cation disordering and amorphization resistance in spinels versus pyrochlores, Nat. Commun. 6 (2015). https://doi.org/10.1038/ncomms9750.

[137] T. Yamamoto, A. Chartier, K. Yasuda, C. Meis, K. Shiiyama, S. Matsumura, Molecular dynamics simulation of point defect accumulation in MgAl2O4, Nucl. Instruments Methods Phys. Res. Sect. B Beam Interact. with Mater. Atoms. 266 (2008) 2676–2682. https://doi.org/10.1016/j.nimb.2008.03.231.

[138] D. Wu, Z. Zhang, W. Fu, X. Fan, H. Guo, Structure, electrical and chemical properties of zirconium nitride films deposited by dc reactive magnetron sputtering, Appl. Phys. A Mater. Sci. Process. 64 (1997) 593–595. https://doi.org/10.1007/s003390050522.

[139] H. Wang, L. Jiao, X. Zhang, L. Shao, D. Chen, K.Y. Yu, C. Jacob, Radiation tolerant nanocrystalline ZrN films under high dose heavy-ion irradiations, J. Appl. Phys. 117 (2015) 145901. https://doi.org/10.1063/1.4917381.

[140] K. Nakai, C. Kinoshita, Y. Muroo, S. Kitajima, Nucleation and growth process of dislocation loops in electron-irradiated β-Nb-3·1 wt% Zr alloy, Philos. Mag. A Phys. Condens. Matter, Struct. Defects Mech. Prop. 48 (1983) 215–230.

https://doi.org/10.1080/01418618308244310.

[141] C. Kinoshita, K. Hayashi, S. Kitajima, Kinetics of point defects in electron irradiated MgO, Nucl. Inst. Methods Phys. Res. B. 1 (1984) 209–218. https://doi.org/10.1016/0168-583X(84)90071-5.

[142] P. Li, J.M. Howe, Dislocation reactions in ZrN, Acta Mater. 50 (2002) 4231–4239. https://doi.org/10.1016/S1359-6454(02)00250-1.

[143] Y.M. Michio Kiritani, Naoaki Yoshida, Hiroshi Takata, Growth of Interstitial Type Dislocation Loops and Vacancy Mobility in Electron Irradiated Metals, J. Phys. Soc. Japan. (1975).

[144] Y. Satoh, C. Kinoshita, K. Nakai, Kinetic study of defect clusters in the MgO-Al_2O_3 system under electron- and/or ion-irradiation, J. Nucl. Mater. 179–181 (1991) 399–402. https://doi.org/10.1016/0022-3115(91)90109-K.

[145] A.Y. Stathopoulos, G.P. Pells, Damage in the cation sublattice of α-Al2O3 irradiated in an HVEM, Philos. Mag. A Phys. Condens. Matter, Struct. Defects Mech. Prop. 47 (1983) 381–394. https://doi.org/10.1080/01418618308245234.

[146] A. Janse Van Vuuren, V.A. Skuratov, V. V. Uglov, J.H. Neethling, S. V. Zlotski, Radiation tolerance of nanostructured ZrN coatings against swift heavy ion irradiation, J. Nucl. Mater. 442 (2013) 507–511. https://doi.org/10.1016/j.jnucmat.2013.02.047.

[147] G.W. Egeland, K. Wheeler, P. Peralta, K.J. McClellan, S.A. Maloy, G.M. Bond, Plastic deformation in zirconium nitride observed by nanoindentation and TEM, J. Nucl. Mater. 416 (2011) 253–261. https://doi.org/10.1016/j.jnucmat.2010.12.002.

[148] J.A. Phys, Mechanism of the swift heavy ion induced epitaxial recrystallization in predamaged silicon carbide, 083516 (2015). https://doi.org/10.1063/1.3236627.

[149] P.K. Sahoo, T. Som, D. Kanjilal, V.N. Kulkarni, Swift heavy ion beam induced recrystallization of amorphous Si layers, Nucl. Instruments Methods Phys. Res. Sect. B Beam Interact. with Mater. Atoms. 240 (2005) 239–244. https://doi.org/10.1016/j.nimb.2005.06.123.

[150] A. Janse Van Vuuren, J.H. Neethling, V.A. Skuratov, V. V. Uglov, S. Petrovich, The effect of He and swift heavy ions on nanocrystalline zirconium nitride, Nucl. Instruments Methods Phys. Res. Sect. B Beam Interact. with Mater. Atoms. 326 (2014) 19–22. https://doi.org/10.1016/j.nimb.2013.10.063.

[151] K. Yasuda, M. Etoh, K. Sawada, T. Yamamoto, K. Yasunaga, S. Matsumura, N. Ishikawa, Defect formation and accumulation in CeO_2 irradiated with swift heavy ions, Nucl. Instruments Methods Phys. Res. Sect. B Beam Interact. with Mater. Atoms. 314

(2013) 185–190. https://doi.org/10.1016/j.nimb.2013.04.069.

[152] K. Yasuda, C. Kinoshita, M. Ohmura, H. Abe, Production and stability of dislocation loops in an MgO-Al_2O_3 system under concurrent irradiation with ions and electrons, Nucl. Instruments Methods Phys. Res. Sect. B Beam Interact. with Mater. Atoms. 166 (2000) 107–114. https://doi.org/10.1016/S0168-583X(99)00738-7.